NTNU
Norwegian University of
Science and Technology

Engineering a vascular model based on microfluidics for studying microbubbles in an acoustic field

Ruth Gong Li

Nanotechnology
Submission date: June 2018
Supervisor: Catharina de Lange Davies, IFY

Norwegian University of Science and Technology
Department of Physics

Abstract

A major challenge in cancer therapy is the poor and insufficient delivery to tumour sites which many chemotherapeutic drugs face. Ultrasound (US) mediated delivery based on cavitating microbubbles (MBs) has emerged as a promising approach to enhance drug delivery to tumours, where several pathways have been proposed. One of the pathways involve the biomechanical effects cavitating MBs exert on the endothelial barrier resulting in enhanced endothelial permeability, with subsequent enhanced drug extravasation from the vascular compartment. In relation to this, Acoustic Cluster Therapy (ACT) has been proposed as a novel approach to solve the limitations of conventional MB formulations including US contrast agents. The mechanisms involved when MBs including ACT bubbles present in the endothelial lumen are subject to US must however be further studied and thoroughly elucidated. This was the motivation for the work that will be presented in this thesis. The goal was to develop a protocol for producing an in vitro system suitable for endothelial cell culture and insonation experiments, allowing interactions between MBs and cells to be studied. Based on experiences from the pre-master specialization project [1], microfluidic devices were designed and fabricated to facilitate seeding of Human Umbilical Vein Endothelial Cells (HUVECs), with optically and acoustically transparent materials. In addition, human prostatic adenocarcinoma (PC3) cells were seeded in microfluidic devices used for insonation experiments to simulate biomechanical interactions between MBs and the endothelial barrier in vivo. Sonoporation, manifested as uptake of the fluorescent dye propidium iodide, could be observed qualitatively (and semi-quantitatively) with both the commercially available MB Sonazoid^{TM} as well as ACT bubbles. Furthermore, the microfluidic device enabled evaluation of MB behaviour in microscale channels during insonation, such as the size of ACT bubbles. The goal of this master project was achieved with respect to establishing an in vitro system that can fulfill its purposes at the proof-of-concept stage.

Sammendrag

En av de store utfordringene i behandling av kreft går ut på å kunne levere kreftmedisiner som cellegift målrettet til svulsten, og ultralydassistert behandling basert på mikrobobler og kavitasjon har fått mye oppmerksomhet i denne sammenhengen. Blant de foreslåtte mekanismene som resulterer i forhøyet opptak i svulsten, er mikroboblers kavitasjon og resulterende biomekaniske effekter på endotelceller, som fører til økt permeabilitet i cellelaget og forhøyet ekstravasasjon. Acoustic Cluster Therapy (ACT) er en ny metode basert på disse prinsippene, som ble utviklet for å imøtekomme flere av dagens mikroboblers begrensninger. Konvensjonelle mikrobobler inkluderer kontrastmidler brukt i klinisk ultralydavbildning. Generelt er det viktig og av stor interesse å studere interaksjonene mellom mikrobobler (inkludert ACT-bobler) og endotelceller under ultralydbehandling for å forstå bioeffektene bedre. Dette var motivasjonen bak undertegnedes masterprosjekt. Målet var å utvikle en fremgangsmåte for å lage et in vitro system egnet for (endotel)cellekultur og ultralydbehandling, der interaksjoner mellom celler og microbobler kan utforskes. Basert på erfaringer fra fordypningsprosjektoppgaven [1], har mikrofluidikkanaler blitt re-designet og produsert for å muliggjøre endotelcellevekst (HUVEC-cellelinje) i kanalen, med materialer som er transparente både overfor lys og ultralyd. I tillegg ble kreftceller (PC3-cellelinje) dyrket i kanalene, som ble brukt i eksperimenter med ultralyd og mikrobobler for å simulere deres biomekaniske interaksjon med endotelcellelag in vivo. Sonoporering, detektert i form av opptak av propidiumiodid, ble observert kvalitativt (og semi-kvantitativt) for både den kommersielle mikroboblen Sonazoid^{TM} og ACT-bobler. På en annen side tillot også mikrofluidikksystemet evaluering av mikroboblers oppførsel i små kanaler under ultralydbehandling, som f.eks. ACT-boblers størrelse. Målet med masterprosjektet er blitt nådd mtp. å utvikle et in vitro-system som oppfyller sin hensikt på et 'proof-of-concept'-nivå.

Preface

This thesis concludes Ruth's M.Sc. degree in nanotechnology at NTNU. The work presented in this master thesis was carried out during the spring semester of 2018 at the Department of Physics and is an extension of the pre-master specialization project from the fall semester of 2017 titled "A Microfluidic In Vitro Model for Studying Acoustic Cluster Therapy" [1]. Hence, substantial portions of the theory and minor parts of the materials and methods chapters (Chapter 2 and 3) have been reproduced, and several references to previous work will be made. Furthermore, minor parts of Chapter 2.4.1 and 2.4.3 have similar content to the unpublished review article "Microfluidic tumour-on-chips - the future in pre-clinical drug assay?" Ruth produced under supervision by Dr. ir. Séverine Le Gac during the academic year 2016/2017.

Acknowledgements

I would like to express my sincerest gratitude towards my supervisor Catharina de Lange Davies and co-supervisor Annemieke van Wamel for all guidance and motivation during the whole academic year 2017/2018. Catharina has always been available for help and advice, and her feedback on this thesis has been very important. Annemieke has been available for Skype meetings, answering questions and sharing very helpful insights, despite not formally being my co-supervisor during this thesis work. Also, I would like to give my special thanks to Melina Mühlenpfordt for helping out with cell culture and experimental planning, for always being available to answer questions and share opinions, as well as for providing feedback on this thesis.

The staff at NTNU NanoLab is thanked for providing training and creating an atmosphere for asking questions and sharing experiences, especially Mark Chiappa and Mathilde Barriet who would always be available to help and share their opinions. In relation to this, The Research Council of Norway is acknowledged for the support to the Norwegian Micro- and Nano-Fabrication Facility, NorFab, project number 245963/F50. Kristin Grendstad Sæterbø is thanked for providing the essential training related to cell culture. Moreover, I thank Ingrid Haga Øvreeide for assistance and sharing her experience related to microfluidic device fabrication. I would also like to thank Jakob Vinje for sharing tips and answering questions related to photolithography. Petros Tesfamichael Yemane is thanked for helping setting up sonication experiments as well as for characterizing one of the transducers that was used in this project. Furthermore, I would like to thank Séverine Le Gac from the University of Twente for providing her guidance and expertise related to microfluidic in vitro models and scientific writing, during my year on exchange (2016/2017), as well as for being available to answer questions and providing interesting and helpful literature after my return to Norway. Jean Baptiste Blond from said university is thanked for providing some very helpful insights based on his experiences with microfluidic cell culture. Last but not least, I would like to thank Birger Langebro for proof-reading this thesis, as well as for being of indispensable support during months of intense and busy days with several late evenings spent in the lab.

Table of contents

List of Tables

List of Figures

Abbreviations

3D - three-dimensional

ACT - Acoustic Cluster Therapy

ACT bubble - activated ACT cluster upon insonation

ACT cluster - a cluster consisting of negatively charged microbubble(s) and positively charged microdroplet(s)

AM - acetoxymethyl

CCD - charge-coupled device

G-device - microfluidic device comprising PDMS bonded to glass substrate

HUVEC - Human Umbilical Vein Endothelial Cell

ECM - extracellular matrix

EPR - enhanced permeability and retention

M-device - microfluidic device comprising PDMS bonded to a PDMS-covered piece of Mylar® sheet

MB - microbubble

MI - mechanical index

PBS - phosphate buffered saline

PDMS - polydimethylsiloxane

PI - propidium iodide

PNP - peak negative pressure

SEM - scanning electron microscopy/microscope

US - ultrasound

UV - ultraviolet

Chapter 1

Introduction

With high mortality and morbidity rates worldwide, cancer is extremely difficult to treat, facing unmet challenges and unanswered questions. Various chemotherapies have been discovered and applied over the years, contributing much to reduced mortality and our current understanding of the disease. However, in many cases, cancer therapy medicines are subject to poor tumour specific uptake, compromising the therapeutic effects and instead increasing the risk of adverse effects. The therapeutic agent has to cross numerous biological barriers to reach its target tumour site and achieve the desired pharmacokinetics. To exemplify, therapeutics administered intravenously need to sustain their circulation time, i.e. avoid premature elimination and clearance, while at the same time being able to extravasate into the tumour. Over the years, various methods to improve tumour specific drug uptake have been proposed and studied. Encapsulating drugs in a variety of micro- and nanoscale carriers, e.g. nanoparticles, has been reported to be advantageous over the free drug in many cases, to increase bioavailability, pass biological barriers and offer targeted delivery. However, the fraction of such carriers reaching the tumour site is extremely low with only 0.7 % of the injected dose accumulating in the tumour, according to a recent metastudy of literature from the past decade [2]. Furthermore, the therapeutic agent has to be internalized by tumour cells and reach its desired intracellular destination. The major obstacle in cancer therapy is therefore not the discovery of an effective chemotherapy, but adequate delivery to the target site.

Ultrasound (US) mediated methods for improved drug delivery have gained interest recently. Most of these approaches consider intravascular injection of micrometer scale gas bubbles (microbubbles, MBs). Upon US exposure, MBs are subject to cavitation events, i.e. volume oscillations, with subsequent biomechanical effects. Cavitation may result in enhanced endothelial permeability towards drugs or nanoparticles present in the vascular compartment, with subsequent enhanced extravasation. Such methods offer targeted delivery to not only tumours [3], but also across the blood brain barrier [4] and to the heart [5]. MBs include commercially available US contrast agents, however, current MB formulations and methods offer limited effects on the endothelial barrier due to the small size of MBs [6]. Moreover, there are safety aspects associated with possible inertial cavitation events where MBs violently explode [7, 8]. To offer solutions to these limitations, Acoustic Cluster Therapy (ACT) has been proposed as a novel approach. The method is based on microbubble cavitation of US activated ACT clusters into ACT bubbles with diameters of 20-30 µm [9], about an order of magnitude larger than conventional US contrast agents.

Indeed, the behaviour of MBs including ACT bubbles inside blood vessels, as well as their interactions with the endothelial wall, must be thoroughly studied and elucidated. As with any novel therapy in clinical application, extensive documentation is necessary for the method to reach market pipeline, including both in vitro and in vivo studies. In this sense, a system mimicking microvessels in vivo where MBs can be studied is highly relevant. The system must be acoustically and optically transparent to allow insonation and inspection by microscopy, respectively. Moreover, the system should preferably allow in vitro cell culture and microscale flow to mimic small diameter blood vessels in vivo. Microfluidic systems present an exceptional opportunity to meet these requirements, and have gained much attention as the next generation of cell culture platforms due to their suitability in various studies involving cells [10–20]. Moreover, with the possibility of dynamic flow conditions similar to the in vivo situation, physiological considerations not available in traditional culture dishes and flasks are enabled.

Combining microfluidics and cell culture with appropriate materials would present a power-

ful tool to study MBs and their effects on the endothelial wall. With this regard, an in vitro system based on microfluidics was previously fabricated in a pre-master specialization project [1], yielding important insights and experiences in the establishment of an artificial vascular model suitable for studying MBs. The in vitro system allowed real-time visualization of activation of ACT clusters into ACT bubbles, but successful culture of endothelial cells was not achieved. The work presented in this thesis is a continuation of the pre-master specialization project, and sought to 1) realize successful endothelial cell culture in microfluidic devices that 2) allow the study of conventional US contrast agents as well as ACT bubbles, to characterize their behaviour as well as their interactions with endothelial cells. Hence, the goal of this master project was to develop a protocol for establishing the in vitro system. Microfluidic devices have been re-designed and fabricated with new materials and methods, with respect to the pre-master specialization project. A cancer cell line was used in addition to endothelial cells for practical reasons, and both Sonazoid^{TM} and ACT bubbles have been studied inside microfluidic devices, to evaluate both their behaviour as well as their interaction with cells through sonoporation. Also new in this project is the low frequency enhancement of ACT bubbles following activation. In the future, this system may serve as a generic tool to gain insights on how MBs behave in vasculature, and how endothelial cells respond to MBs and cavitation in vivo. While microfluidic models with cells have been reported in sonoporation studies a few times [21–23], they have not yet been employed to study ACT bubble interactions with endothelial cells, and there is in general very limited literature on MB-cell interactions in such vascular models.

Chapter 2

Theory

2.1 The challenges of drug and nanoparticle delivery

Localized delivery of drugs to their desired target sites is crucial in order to maximize the therapeutic effects and reduce adverse effects, and this is especially relevant in chemotherapy. The field of nanomedicine is in the forefront to improve drug delivery, with developments over the past two decades that have resulted in the emergence of nanometer scale carriers, or nanoparticles, that incorporate various sensing plus imaging, targeting and therapeutic agents. In particular, the ability of nanoparticles to encapsulate drugs (and genes) is a major topic of interest, as targeted delivery, controlled drug release and improved pharmacokinetics are potentially enabled. In cancer therapy, the adverse effects of a chemotherapeutic agent can be minimized as the drug exposure to healthy tissue is reduced, and the circulation time of the drug is improved as the nanoparticle protects it from elimination. Such nanoparticles could consist of inorganic materials like metals [24], carbon [25], semiconductors [26], organic and biodegradable polymers [27] and lipids [28], or a combination of materials, e.g. metal and polymer such as in superparamagnetic iron oxide nanoparticles [29].

There are several features of the tumour microenvironment that make nanoparticles especially attractive for drug delivery to cancers. First of all, due to the enhanced permeability and

retention (EPR) effect found in tumour vasculature, many nanoparticles have an inherent capability of tumour accumulation. The EPR effect stems from the poor and defective architecture of blood vessels inside and in the proximity of tumours, where several factors contribute to overall enhanced permeability, such as large fenestrae expelling particles bigger than 40 kDa from the vessel [30]. Impaired lymphatic drainage around the tumour increases the retention of such particles [30]. On the other hand, nanoparticles themselves may be designed to enhance drug delivery, for example through surface modifications that provide targeting or prolong circulation. Examples include targeting ligands that may be added to enable receptor recognition and subsequent receptor-mediated endocytosis [31], or functionalization with polyethylene glycol that protects the nanoparticle from aggregation, opsonization, and phagocytosis [32].

As with any drug, nanoparticles face many physiological barriers before reaching their target destination in vivo. These include organ-specific barriers, opsonization and subsequent phagocytosis, extravasation from circulation in addition to a non-specific distribution [2, 33]. Moreover, the nanoparticle has to penetrate into the tumour microenvironment which consists of a dense extracellular matrix (ECM) and stromal cells [2, 33]. The drug carrier is further hindered by the high interstitial fluid pressure of the tumour which reduces transport from capillary to tumour [33, 34]. Last but not least, the internalization of the nanoparticle and subsequent endosomal escape present additional barriers that hamper their therapeutic potential [35]. Consequently and despite the many opportunities and discoveries, current nanoparticle-encapsulated chemotherapies offer minimal improvements in terms of efficacy, compared to their respective conventional formulations [33].

2.2 Enhancing drug delivery using ultrasound

2.2.1 Physical principles of ultrasound

US is a transmission of pressure waves through a medium at frequencies above 20 000 Hz and has many of the same wave properties as optical waves, such as amplitude, frequency, intensity, wavelength and propagation velocity (speed of sound) [36]. Similarly to light, US waves may be absorbed and focused [37], and give rise to reflected and transmitted waves at interfaces between media. As in optics, the transmitted wave will be refracted away from the direction of the incident wave, according to Snell's law, if the propagation velocity c in the two media is different:

$$\frac{\sin\theta_1}{c_1} = \frac{\sin\theta_2}{c_2}, \tag{2.1}$$

where θ_1 is the incident wave angle and θ_2 is the refracted angle [36, 38]. c is a material characteristic given by

$$c = \sqrt{\frac{M_e}{\rho_e}}, \tag{2.2}$$

where M_e and ρ_e are the effective elastic modulus and mass density, respectively [36]. Multiplying c and the mass density at rest yields a new parameter of interest, namely the specific acoustic impedance Z of the medium. Soft biological tissues have similar Z to that of water, which is 1.48×10^6 kg/s·m^2. Air, on the other hand, has a Z of as little as 4×10^{-6} kg/s·m^2 [38]. Hence, ultrasonic reflection and refraction at interfaces can be understood as a difference in acoustic impedance in two media.

Unlike optical waves, US propagates only longitudinally except for in some solids where transverse or shear waves will also be present [36]. In biological tissues, US shear waves are typically neglected [36]. US has the ability to compress and expand the medium through which it propa-

gates. Resulting particle displacement can be evaluated by considering an incremental cube of material within a body, with external forces applied to it [38]. If the wave propagates along the positive z-direction, the longitudinal displacement W is given by

$$W(z,t) = W_0 e^{j(\omega t + kz)}, \tag{2.3}$$

where ω is the angular frequency and k is the wave number [38]. As the US propagates, a non-zero force is exerted on the medium, namely the acoustic radiation force. This force can be understood as a transfer of momentum from the acoustic wave to particles in a fluid medium. The suspended particles experience the acoustic radiation forces as hydrodynamic forces leading to drift, clustering, attraction and repulsion [39]. Assuming zero attenuation, particle displacement velocity v is related to the sound pressure P_s as [36]

$$P_s = \rho c v = Z v. \tag{2.4}$$

However, US attenuation in matter is inevitable due to energy loss from reflection, scattering and refraction. P_s and acoustic intensity I decrease exponentially with traveling distance z according to

$$P_s = P_{s,0} e^{-\alpha z}, \tag{2.5}$$

$$I = I_0 e^{-2\alpha z}, \tag{2.6}$$

where α is the pressure frequency-dependent attenuation coefficient, with the implication that attenuation increases with frequency [36, 38]. α is expressed in nepers or decibels per centimeter times frequency, and is a material property. While the attenuation coefficient of air is 11.98 dB/cm·MHz, it is only 2.17×10^{-3} dB/cm·MHz for water [38]. This is among the reasons why insonation is typically done with the transducer placed in water, and a gel is applied in clinical use to avoid any air gap between the patient's skin and the US transducer.

US has been used in medical imaging for decades as its reflection characteristics at tissue interfaces can be detected and related to the depth of the reflecting surface. For example, small objects relative to the US wavelength tend to scatter the acoustic waves, which are detected as scattered echoes, whereas larger objects with smooth surfaces compared to the wavelength reflect angle-dependent specular waves [36].

2.2.2 Ultrasound transducers

Acoustic waves may be generated by US transducers which use piezoelectric crystals, i.e. materials that convert electrical signals to mechanical vibrations and vice versa. More precisely, upon the presence of an electric potential difference across a slab of piezoelectric material (i.e. an electric field), electric dipoles in the material are re-aligned, causing deformation of the material [38]. Conversely, deformation of the material due to stress causes re-orientation of the dipoles, giving rise to non-zero charge accumulations and resulting electric field across the material. These phenomena are known as the reverse and direct piezoelectric effect, respectively. In US transducers, the former effect is employed. A time-varying voltage across a piezoelectric material results in expansion and contraction of the material, mechanical vibrations that generate US. In medical applications, US is typically applied as pulses with a certain duration and frequency [38]. The pulse frequency determines the frame rate in many transducers that are used in medical imaging, as each pulse echo gives rise to an image. The transducer can consist of a single piezoelectric element, or multiple elements arranged as a line (one-dimensional or linear array), in rows or columns (two-dimensional array), or concentrically aligned ring-shaped elements (annular array) [38]. Multiple elements allow steering and focus of the US beam, e.g. control of the beam geometry and direction [40]. This is achieved by exciting individual or groups of piezoelectric elements with appropriate time lags, known as phasing. Transducers that employ phasing are commonly referred to as phased array transducers.

2.2.3 Ultrasound mediated drug delivery

In tissue, US has thermal and mechanical effects with resulting implications on surrounding cells or particles. Thermal energy can be absorbed in target tissue from US, resulting in localized hyperthermia that can be exploited to heat up or ablate tissue, or melt drug carriers. The mechanical effects on the other hand, are manifested as fluid motion. US may cause oscillatory and even convective motion of the insonated fluid that enhances molecule transport and thus drug transport, or drugs may be pushed towards their target by acoustic radiation forces. [37]

Recently, the combined use of US with MBs to induce biomechanical effects that enhance drug (and gene) delivery, has gained attention, as reviewed by several authors [3, 37, 41–43]. Conventional MB formulations include commercially available US contrast agents used in medical imaging to improve the acoustic contrast between blood and surrounding tissue. These MBs have been studied to enhance delivery to tumours in several reports [44–48], with positive results from a clinical phase I trial [49]. Although the gas is mainly responsible for the acoustic properties, US contrast agents typically have a shell in order to add mechanical stiffness and reduce their compressibility [42], which stabilizes the bubbles both in vitro and in vivo [50]. Such formulations include phospholipid membrane MBs such as perfluorocarbon gas filled Sonazoid™ (GE Healthcare AS), sulphur hexafluoride gas filled Sonovue™ (Bracco diagnostics Inc.) and octafluoropropane gas filled Definity™ (Lantheus Medical Imaging Inc.). Other shell materials exist, such as cross-linked serum albumin in Optison™ (GE Healthcare AS) which are also filled with octafluoropropane gas. US contrast agents have typical diameters in the 1-4 μm range [3].

2.2.3.1 Microbubble behaviour in acoustic fields

Gas bubbles in a medium exposed to US respond by oscillating, i.e. expanding and contracting, in the acoustic field. This activity is referred to as cavitation [3, 37, 51]. At low acoustic pressures, the oscillation is linear and inversely proportional to the local acoustic pressure [52].

However, at higher pressures, a non-linearity arises and bubbles have a lengthened expansion phase. This leads to bubble growth by a process commonly termed as rectified diffusion [53]. Expansion of the bubble decreases its internal pressure which results in an in-flux of gas. The enhanced gas diffusion is further driven by effects such as the enlarged surface area of the bubble, and an increased concentration gradient of gas due to the reduced liquid-air mass transfer boundary around the bubble [53]. During stable cavitation, a bubble increases in size until reaching a certain "equilibrium" size, whereupon it exhibits stable, low amplitude oscillation around this equilibrium size [52, 54]. The oscillation generates local microstreams around the MB with associated forces that can act on neighbouring particles or cells. A different cavitation mechanism known as collapse or inertial cavitation produces considerably higher forces compared to stable cavitation. At higher US intensities, rapid increase of MB oscillation amplitude leads to MB collapse due to the inertia of the inrushing fluid [52]. For the collapse to happen, a critical maximum radius of twice the equilibrium radius of the oscillating bubble has been predicted [55], and the threshold for onset has been found to decrease for increasing MB volume concentrations [7]. Inertial cavitation generates extreme shear stresses by the resulting shock wave, and can lead to the formation of microjets.

In the acoustic field, MBs may also interact with each other. Several authors have studied MB behaviour with high-speed imaging tools to characterize phenomena such as coalescence [56] and aggregation [57]. During coalescence, two (or several) neighbouring MBs collide and become a single bubble, which happens as two adjacent MBs in solution expand in the acoustic field. Before making contact, the MBs are separated by an amount of trapped liquid between the two surfaces, that is drained so that the separation between the MBs decreases until reaching a critical distance [56]. The MBs will then coalesce due to instability of the separation. On the other hand, MB aggregation is due to an attractive secondary acoustic radiation force commonly referred to as the secondary Bjerknes force. This force describes the interaction between two oscillating bubbles experiencing the same acoustic field, and its magnitude increases with decreasing distance between the bubbles [39]. The secondary Bjerknes force is repulsive in any case the driving frequency ω of the field lies between the resonance frequencies ω_1 and ω_2 of the two bubbles, i.e. $\omega_1 < \omega < \omega_2$, and will be attractive as long as this condition is not fulfilled [39]. Importantly, the underlying theory assumes that

the separation distance between the two bubbles is initially much larger than the bubble radii. Stable aggregates of MBs can be explained by the interaction force switching from attractive to repulsive as the separation between the two MBs decreases [39].

Nevertheless, MBs in a solution may also experience events that are not a direct effect of an acoustic field. In general, small bubbles with high Laplace pressure (given by high surface tension) may shrink or completely dissolve. In the presence of larger bubbles, the dissolution of smaller bubbles will create local areas of supersaturation that cause larger bubbles to grow [58], a process commonly known as Ostwald ripening. The rate of this process will increase or decrease depending on the surface properties of the MB, such as its composition [58].

2.2.3.2 Biophysical effects of cavitating microbubbles

There are several biophysical effects associated with cavitating MBs that give rise to different drug delivery pathways. In the proximity of a cell, the oscillation may cause the MB to make physical contact with the cell, with pushing and pulling of the cell membrane [59]. MBs have also been reported to be able to cross cell membranes and enter cells during insonation [60]. One of the proposed main mechanisms is that the oscillations generate microstreams around the bubble with associated shear force on cell membranes that increase with oscillation amplitude, sometimes high enough to rupture surrounding cells and drug carriers [37]. Moreover, the circulating eddies or microstreams around the MB may significantly increase drug transport due to convection, or due to net forces acting on suspended bodies in the vicinity of a bubble [37]. MB cavitation could find applications in combination with both co-injected free drug agents [61, 62], drugs encapsulated within MBs [63], or drugs encapsulated within nanoparticles [64]. Enhanced macromolecular endocytosis in the vicinity of US and MBs has been reported [65], and direct deposition of nanoparticles (initially bound to MBs) in patches onto the cell membrane has also been observed [59].

MB cavitation may have effects on surrounding cells and tissues with critical implications on drug transport across physiological barriers such as the capillary wall. For example, stable

cavitation resulting in MBs pushing against the blood vessel wall may increase the gap size between endothelial cells, facilitating drug entry into target tissue [3]. While US itself is thought to have little effect on cells and tissues, the stresses that originate from the cavitation events, e.g. due to microstreams or pushing and pulling during stable cavitation [52], may create pores [37, 41]. This process is known as sonoporation [3, 52], and results in local increase of drug extravasation [3, 66]. Sonoporation may also target the tumour directly to increase drug uptake in cancer cells [67, 68], or reduce nutrients supply to the tumour by disrupting or mechanically destroying the tumour vasculature [69]. Sonoporation is especially associated with inertial cavitation [3] as the forces resulting from microjets and shockwaves perforate cell membranes and permeabilize blood vessels [52]. Inertial cavitation is however problematic due to the potential associated tissue damage and safety aspects in vivo; endothelial cells may be ruptured due to the extreme shear forces [37], with the possible effects of capillary rupture, hemorrhage and DNA fragmentation [7]. Nevertheless, there seems to be a matter of debate whether inertial cavitation is in fact crucial for enhanced drug delivery to take place [6].

There are several limitations to using conventional US contrast agents for improved drug delivery. High intensity US leading to subsequent inertial cavitation is often associated with current MB drug delivery approaches [7, 8]. Furthermore, the small MB size, short circulation time and free flowing behaviour limit the range and extent of the necessary biomechanical effects exerted on the vasculature [6].

2.2.3.3 The mechanical index

In relation to US for clinical applications, there are some particular parameters of interest. Modern US machines give a measure of the thermal and mechanical effects by displaying a thermal and mechanical index, respectively. The mechanical index (MI) is especially interesting in this context, as it was developed and introduced in order to predict the onset of inertial cavitation to foresee mechanical stress or tissue damage [70]. MI is commonly expressed as

$$\mathrm{MI} = \frac{\mathrm{PNP}}{\sqrt{f_c}}, \tag{2.7}$$

with PNP being the peak negative (or rarefactional) pressure given in MPa, and f_c the US center frequency given in MHz [71, 72]. MI is commonly expressed as a dimensionless number and is recommended to be below 1.9 in medical diagnostic imaging, according to guidelines by the American Food and Drug Administration [72]. Note that this threshold does not apply for US contrast agents, as onset of MB inertial cavitation can happen at MI $>$ 0.5 (at an f_c of 3 MHz) [70].

2.2.4 Acoustic Cluster Therapy

ACT has been investigated and suggested as a novel therapy based on the biophysical mechanisms of cavitating MBs, while addressing the aforementioned drawbacks of currently available US contrast agents. The approach is based on co-injecting drugs (e.g. chemotherapies) or nanoparticles and a dispersion of so-called "ACT clusters". ACT clusters are formed by electrostatic interactions between conventional MBs of negative charge, and positively charged oil-phase microdroplets [9]. Clusters consist predominantly of one MB and one microdroplet, but triplets, quartets etc. also exist, giving rise to a cluster population of varying size, most in the 3-10 µm range [9]. A two-step process of sonication is applied to first activate ACT clusters at US frequency in the 1-10 MHz range, followed by an enhancement step of low frequency (0.3-1 MHz) US that induces stable cavitation. During the activation step, MBs transfer energy to the microdroplets which undergo a subsequent liquid-to-gas phase transition. This process is achievable at MI $<$ 0.4, in contrast to previously proposed related methods such as the acoustic droplet vaporization method, where MI $>$ 2 is common [73]. The oil vapour then enters the MB after 5 µs [61] resulting in a single bubble (ACT bubble) that continues to grow, eventually reaching 20-30 µm, reported up to 50 µm [9]. The ACT bubble will then transiently deposit in the microvasculature, locally in direct contact with the endothelial wall in a fraction of the capillary. Blood flow is temporarily occluded in these areas, which leads to a local increase of drug concentration due to the hampered drug wash-out. During the subsequent enhancement step, stable cavitation of ACT bubbles causes

mild biomechanical effects on the surrounding endothelial cells [62] including sonoporation [61]. Consequently, extravasation is enhanced with subsequent increase of drug uptake in tumour. Thus, ACT offers considerably larger bubbles than conventional MBs with an increased potential to interact with the endothelium, as well as eliminating the safety issues associated with inertial cavitation. A schematic illustration of the principle is shown in Figure 2.1.

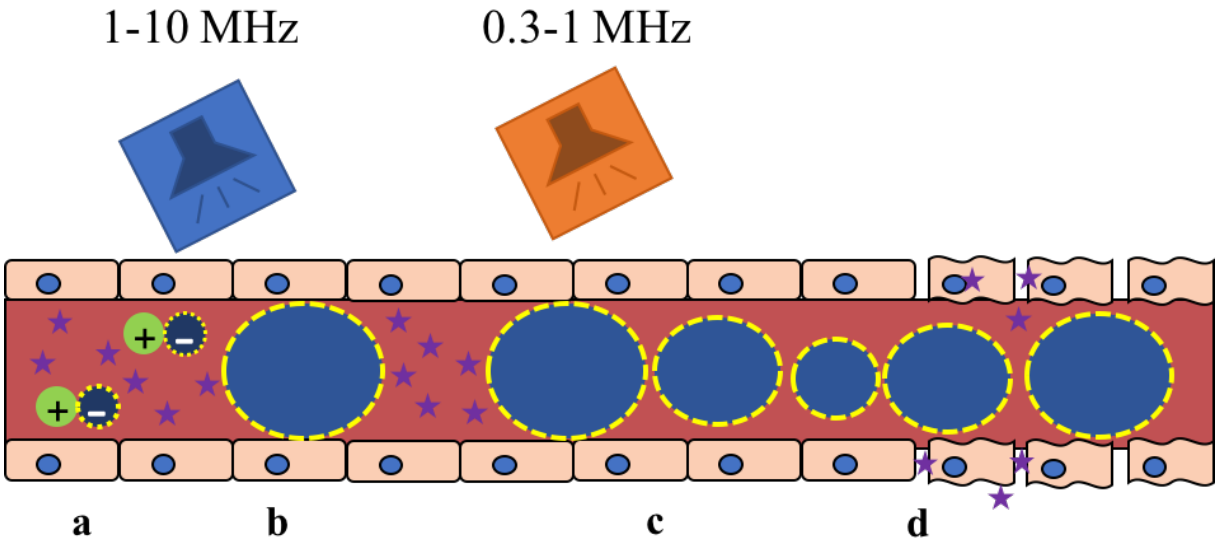

Figure 2.1: Schematic illustration of the principle behind Acoustic Cluster Therapy (ACT) inside a capillary. **a)** Clusters of positively charged microdroplets and negatively charged MBs are co-injected with drug (indicated by stars). Upon insonation, clusters are activated to form ACT bubbles that transiently deposit in the microvasculature, increasing drug concentration locally (**b**). A second step of low frequency US induces stable cavitation of the ACT bubble (**c**). This causes biomechanical effects on the surrounding endothelial cells, increasing the endothelial permeability and subsequent drug extravasation (**d**).

The inventors of ACT, Per Christian Sontum, Svein Kvåle and Andrew John Healey, co-founded the company Phoenix Solutions AS in 2013 and filed a patent the following year. Pre-clinical studies of the technology have shown promising results, demonstrating that ACT is safe at dose levels up to 1 mL/kg with activation in the liver and heart of rats and dogs [74]. Moreover, the synergistic effect of this treatment with the chemotherapies paclitaxel [61, 62] and Abraxane® [62] has been confirmed in two recent pre-clinical studies.

2.3 Fundamentals of microfluidics

The term ”microfluidics” is widely associated with the engineering or application of fluid flow systems that contain channels and/or chambers with at least one dimension below 1 mm, where liquid volumes in the microliter to picoliter range can be controlled and manipulated. In many applications, microfluidics present an enabling alternative to traditional macroscale liquid handling systems, as the minituarization offers portability, low material and space consumption as well as high sensitivity. As will become evident in Chapter 2.4, microfluidic technology is especially interesting in developing advanced cell culture systems.

2.3.1 Underlying principles of microflows

Before presenting the governing equations describing microflows, some fundamental assumptions and principles must be mentioned, that originate from general fluid mechanics. Firstly, the continuum approximation is applied on the fluid to assume an average of fluid properties (i.e. velocity and density) rather than properties of individual molecules of the fluid. Despite volumes down to the picoliter range, the approximation is valid for microfluidics as the number of water molecules (3×10^{13} molecules/pL) is still high. Hence, microflows can be analyzed from the same governing principles as for macroscale fluid mechanics [75]. Secondly, fluids are classified as Newtonian or non-Newtonian fluids to characterize how the fluid's rate of deformation is related to viscous stress present in the fluid during flow. For Newtonian fluids, the viscous shear stress τ is directly proportional to the derivative of the velocity in the direction perpendicular to the shear plane, i.e. $\frac{\partial u}{\partial y}$, through the fluid (dynamic shear) viscosity η:

$$\tau = \eta \frac{\partial u}{\partial y}, \tag{2.8}$$

implying the fluid is non-Newtonian if η is shear-dependent. Non-Newtonian fluids may experience both increase as well as decrease of viscosity as shear stress increases, such as in the case of blood flow in small and intermediate diameter vessels [76]. On the other hand, water and other small molecule liquids are often assumed as Newtonian.

As a consequence of the small dimensions, flow in microfluidic channels is laminar, implying that viscous forces dominate. Laminar flow assumes that fluid mixing occurs solely due to diffusion in contrast to the case of e.g. turbulent flow where mass transport due to convection also takes place. The Reynold's number, Re, is an important parameter in these systems, giving the ratio between inertial and viscous forces in the flow to determine the flow regime:

$$Re = \frac{\rho u_0 L_0}{\eta}, \tag{2.9}$$

where ρ is the fluid density and u_0 and L_0 denote the characteristic linear velocity and length scale of the system, respectively [77]. For conventional microfluidic devices, Re is typically below 1, while the transition to turbulent flow occurs at values above 2000 [78]. As physiological fluid flow is characterized by Re far below 2000, laminar flow is often assumed in these cases. Transitions to turbulent flow in vivo is associated with sites with diameters above the micrometer scale such as in the heart valves and aorta, or in diseased arteries [79].

2.3.2 Governing equations in microflow systems

The motion of a Newtonian and incompressible fluid can be described by the following expression of the well-known Navier-Stokes equation:

$$\rho\vec{g} - \nabla p + \eta\nabla^2\vec{u} = \rho\left(\vec{u}\nabla\vec{u} + \frac{\partial\vec{u}}{\partial t}\right), \tag{2.10}$$

where ρ denotes fluid density, $\vec{g}$ is the gravitational acceleration, p denotes pressure and u is the flow velocity [77]. As can be seen from the equation, fluid flow is thus described by forces due to gravity, pressure gradient and viscosity, respectively. In microsystems, Poiseuille flow is often assumed, which simplifies (2.10) into a linear equation containing only a pressure and a viscosity term. Poiseuille flow concerns the steady-state (i.e. $\frac{\partial u}{\partial t} = 0$), laminar flow of a Newtonian fluid in a straight, rigid channel. Flow is driven by a pressure gradient between the two ends of the channel, where gravitational body forces are neglected and there is a no-slip condition at the channel walls [77]. Moreover, the flow is unidirectional, parallel to the axis of

the channel, implying $\vec{u}\nabla\vec{u} = 0$. With these conditions, (2.10) can be written as:

$$\nabla\vec{p} = \eta\nabla^2\vec{u} \tag{2.11}$$

which can be solved to obtain (analytical) solutions of the flow velocity for various channel geometries. For a circular channel of radius a and length L, velocity u along the channel axis (x-direction) is given by

$$u(y,z)_{circular} = \frac{\Delta p}{4\eta L}(a^2 - y^2 - z^2), \tag{2.12}$$

where y is the position along the channel width, $\frac{-a}{2} < y < \frac{a}{2}$, and z is the position along the channel height, $\frac{-a}{2} < z < \frac{a}{2}$ [77]. Similarly, for a rectangular channel of length L with height h and width w, $h < w$, the solution, along the channel axis, is [77]

$$u(y,z)_{rectangular} = \frac{4h^2\Delta p}{\pi^3\eta L}\sum_{n,\text{odd}}^{\infty}\frac{1}{n^3}\left[1 - \frac{\cosh(n\pi\frac{y}{h})}{\cosh(n\pi\frac{w}{2h})}\right]\sin(n\pi\frac{z}{h}). \tag{2.13}$$

Knowledge about the velocity can be used to compute the volumetric flow rate Q - a constant describing the amount of liquid passing through the channel per time. Q can be found by multiplying the average velocity with channel cross section area, which is the same as performing a spatial integral on $u(y,z)$. For (2.12) and (2.13), we arrive at

$$Q_{circular} = \frac{\pi a^4}{8\eta L}\Delta p, \tag{2.14}$$

and

$$Q_{rectangular} \approx \left[1 - 0.63\frac{h}{w}\right]\frac{h^3 w}{12\eta L}\Delta p. \tag{2.15}$$

Moreover, Q may be expressed at a form analogous to Ohm's law, known as the Hagen-Poiseuille law:

$$Q = \frac{\Delta p}{R_h}, \tag{2.16}$$

where R_h is the hydraulic resistance - a proportionality constant between the pressure and flow rate describing the resistance to flow. R_h depends on channel geometry, thus, it is an important parameter to consider when designing microfluidic channels. This can be seen directly by inserting (2.16) into (2.14), or (2.15):

$$R_{h,circular} = \frac{8\eta L}{\pi a^4} \tag{2.17}$$

and

$$R_{h,rectangular} \approx \frac{12\eta L}{1 - 0.63h/w} \frac{1}{h^3 w}. \tag{2.18}$$

As in an electrical circuit, channels arranged in series or in parallel are analogous to electrical resistors and follow the same additive rules to compute the total resistance [77]. The magnitude of the hydraulic resistance is critical in microfluidic systems as the hydraulic resistance can directly oppress liquid flow in small diameter channels. In particular, the hydraulic resistance is an important consideration at channel junctions as an asymmetrical resistance will result in an uneven liquid flow, in the worst case blockage of the high resistance channel.

Knowledge about the flow velocity u can also be used to find the channel wall shear stress, as seen in (2.8) for $y = 0$.

2.4 Microfluidic in vitro models

2.4.1 Microfluidics as an enabling tool in cell culture

Initially, applications of microfluidics were centered around biomolecule analysis from an analytical point of view, which later gave rise to terms like 'lab-on-a-chip' and 'micro total analysis systems' (μTAS). Recently, there has been a shift towards biological applications involving complex cell cultures [13] and single cell analysis [80], as microfluidics allows manipulation of fluids and forces at the characteristic scale of a cell [11]. These systems can contain one single or a network of micrometer scale channels inside which cell culture medium and liquid reagents can flow at a controllable rate. Several features make microfluidic devices highly suitable for cell culture purposes. First of all, in such small set-ups only a limited amount of cells and materials is needed. This would make microfluidic systems favourable for experiments using rare or expensive materials. Moreover, the small size enables continuous perfusion of cell culture medium, in contrast to conventional bioreactors, where medium must be collected and reused [81]. Delivery of nutrients and other chemical cues to cells can be done in a controlled manner in microfluidic systems [82]. Mechanical cues can also be considered such as by implementing mechanically deformable substrates [82]. Devices themselves ensure effective gas and thermal exchange due to the large surface to volume ratio. Moreover, real-time visualization and quantitative analysis of various biological processes are enabled as many devices are optically transparent [82]. Undoubtedly, it is the presence of flow that is the most important feature. Fluid flow in microfluidic devices can be precisely tuned to mimic the dynamic flow conditions found in vivo and resulting physiological stress experienced by cells. Thus, it is widely accepted that microfluidic platforms give rise to more physiologically relevant cell cultures in contrast to traditional Petri dish cultures in static (i.e. no flow) environments. This is true not only for achieving the culture itself, but also for the specific application where the cell culture serves as a model, such as in drug screening assays [15, 16], cell-to-cell interaction studies [17] and cell migration studies [83, 84].

Cell cultures of high complexity are possible with microfluidics. Functionalization with ECM mimicking proteins allows cell attachment to channel walls [12], or growth or migration

into three-dimensional (3D) ECM networks [83–86] to include cell-matrix interactions. Compartmentalization of devices enables co-cultures where cells are allowed to interact across different cell types [83, 85, 87–91], and 3D clusters of tumour cells may be created to mimic solid tumours by trapping and culturing cells in microfluidic systems [14, 92]. Furthermore, the device may be integrated with programmable valves and pumps for automated liquid handling [93]. The term ”organ-on-chips” is widely used to denote such models, which have gained much publicity as the next generation of cell cultures. An increasing number of devices, studies employing microfluidic cell cultures and protocols have been reported, along with multiple review articles on the topic [10–14].

2.4.2 Flow considerations in cell culture

Prediction of flow behaviour, e.g. flow velocity, hydraulic resistance and shear stress, is useful in order to optimize device design for a certain application. The mathematical equations given in Chapter 2.3.2 are helpful in describing the flow of Newtonian fluids in simple microchannel geometries where solutions to the Navier-Stokes equation are easily obtainable, but are limited to these cases. To predict the flow behaviour in more complex systems, e.g. when channels branch into channels of smaller widths or in cases where the layout is asymmetric, simulation software or experimental measurements will be more useful. The likely shear-dependent viscosity of a solution containing significant concentrations of proteins and cells could be another important consideration. Also, when cells occupy significant space in microchannels, the altered channel geometry and effective dimensions (i.e. the space available for liquid flow) should be considered. Nevertheless, the equations in Chapter 2.3.2 still provide fundamental insights on the effects of channel dimensions. For example, as can be seen from (2.17) and (2.18), the hydraulic resistance is proportional to channel length, but is much more affected by channel height or radius (to the power of 3 and 4, respectively). This would for instance imply that the presence of cells or air bubbles in the channel would lead to an increased R_h, oppressing flow. If a portion of the channel is filled with air, the resistance against flow may be so high that flow is completely obstructed. Increasing the pressure to drive the flow may potentially have detrimental effects on cells present in the channel.

Flow parameters may be important to achieve a successful cell culture. For example, flow velocity is central in manipulating shear stress experienced by cells, as seen from (2.8). Shear stress affects cell morphology, gene expression and interactions between cells and ECM [94], and could thus be essential in a given application. A study showed that endothelial cells exposed to shear stresses of 15-30 dyn/cm^2 had reduced susceptibility to undergo apoptosis, while shear stress of 1 dyn/cm^2 had no effect [95]. In microfluidic endothelial cell culture, shear stress should preferably be in a physiological range. In vivo measurements of shear stress in human capillaries of 4-24 µm revealed a mean value of 15.4 dyn/cm^2 [96].

Replenishing cell culture medium in microfluidic devices happens by flowing fresh medium into the device, displacing the old medium. This can be done in various ways, such as using a micropipette, a syringe pump [22, 97–100], a peristaltic pump [101], integrated micropumps [93, 102], or simply by exploiting gravity [87, 92]. Throughout this master project, gravity driven flow has been explored as a means of continuously delivering medium to cells inside microfluidic devices, even while inside a cell culture incubator. The method, which requires no external pump, is a passive pumping method where the pressure driving the flow is given solely by hydrostatic and capillary pressures. The relative magnitude of the latter depends on the surface to volume ratio of the channel or fluid reservoir in question, as capillary forces result from liquid surface tension. For a fluid column of height ΔH, the pressure at the bottom of the column is Δp higher than at the top due to the hydrostatic pressure, with

$$\Delta p = \rho g \Delta H, \tag{2.19}$$

where ρ is the density of the liquid and g is the gravitational constant [77, 103]. For a microfluidic channel used for cell culture, it is useful to consider two reservoirs connected to the inlet and outlet of the channel respectively, where medium can flow from the inlet reservoir into the outlet reservoir. Then, ΔH in (2.19) is the height difference between the two reservoirs [103]. As ΔH decreases with time, Δp and thus Q decrease with time. Ultimately, when the two liquid columns have equalized their height, flow is zero unless capillary forces are able to induce

further liquid movement.

2.4.3 Reported microfluidic vascular models and devices for sonoporation studies

Microfluidic platforms as vascular models have been reviewed previously by several authors [18–20, 104], but as will become evident, their application in studying cavitating MBs is limited. Various devices incorporating endothelial cell culture have been produced to study a range of processes including pathophysiological processes such as thrombosis [87, 99] and cancer angiogenesis during co-culture with tumour and/or stromal cells [83, 87, 90, 91], and effects of shear stress on endothelial cell morphology [101], gene expression [101, 105], cytoskeletal remodeling [106], and even binding to ligand-functionalized nanoparticles [107]. The range of different applications gives rise to a variety of microfluidic devices and designs as depicted in Figure 2.2. All devices except for the one in Figure 2.2h were employed for endothelial cell culture.

Individual channels for ECM constituents in 3D networks are visible in devices in Figure 2.2a-b. In Figure 2.2a, endothelial cells (Human Microvascular Endothelial Cells cell line) are allowed to migrate from a ”cell channel” into a collagen scaffold to study angiogenesis influenced by tumour cells (MTLn3 or U87MG cell lines) that are co-cultured in a ”condition channel” [83]. Channel dimensions are given in the figure. In the device shown in Figure 2.2b, Human Umbilical Vein Endothelial Cells (HUVECs) grow at the interface between a ”main channel” and side channels filled with basement membrane extract and chemokines, to study extravasation of tumour cells (ACC-M cell line) from the main channel into the side channels, across endothelial cells [84]. Main channel had a cross section of 1000 µm × 150 µm (width x height) and side channels were 600 µm × 100 µm.

Figure 2.2c shows a microfluidic design according to a computer mapped image of a hamster cremaster muscle to create a physiological vascular model, with rectangular channels of 50 or 100 µm height (widths not given) [100]. The resulting device was used to culture bovine aortic

endothelial cells. Figure 2.2d shows a branched microchannel structure that was developed to study microvascular interactions in hematological diseases [97], and was employed to study occlusion and thrombosis by culture of HUVECs [99]. The device allowed culture for up to 8 days. Smallest channels had a cross section of 30 µm × 30 µm. Figure 2.2e shows HUVECs cultured in a single 50 µm × 50 µm channel to characterize endothelial linings including presence of adherence junctions, after 6 days of culture [98]. In the device depicted in Figure 2.2f, a single inlet and outlet port are connected to five "flow-control channels" of 1000 µm width and 40-87 µm height, which branch into two "culture channels" each, of 3000 µm × 213 µm (width x height) [101]. This gives rise to higher hydraulic resistance in the flow-control channels with respect to the culture channels. HUVECs were cultured in the culture channels in order to study effects of shear stress, which was tuned by the varying resistance in the flow-control channels.

In Figure 2.2g, a culture chamber of 1000 µm × 120 µm (width x height) is connected to a source and sink channel, respectively, of 500 µm × 120 µm, separated by microchannels of just 5 µm × 4 µm [108]. HUVECs were loaded into and cultured in the culture chamber. The source and sink channels provided concentration gradients of growth factors that were loaded into the source and diffused into and across the cell culture chamber, to study resulting cell behaviour. Figure 2.2h shows a microfluidic device functionalized with interdigital transducers (visible as four panels) to generate surface acoustic waves, to induce sonoporation of single tumour cells (MFC-7 cell line) by MBs present in a microfluidic device [21]. The microfluidic device consisted of a single cylindrical channel of 600 µm radius, but was designed to have a height of 16 µm in order to trap tumour cells of larger size. It was not given whether the device allowed cell culture. By applying appropriate voltages at the interdigital transducers, surface acoustic waves would steer MBs towards single tumour cells. A single pulse of 24 MHz and 41 µs duration would lead to the collapse of 3 µm MBs with subsequent sonoporation of tumour cells. The authors also used a similar device to initiate release of doxorubicin from temperature sensitive liposomes by high intensity focused US from the surface acoustic waves [109].

All the devices mentioned so far were fabricated using the polymer polydimethylsiloxane

(PDMS) - which is the most widely employed material in microfluidic device fabrication [110]. Other materials for device fabrication are however possible. Figure 2.2i shows a device of collagen gel with a plexiglass housing, the collagen casted from a PDMS master to yield straight and parallel microchannels of 100 µm × 100 µm cross section connected to a single inlet and outlet [87]. HUVECs readily attached to all channel walls and could be cultured for 4-7 days. The device had a PDMS reservoir on top to store growth medium, which was to be delivered by gravity-driven flow, a process described in Chapter 2.4.2. Sonoporation of HUVECs was successfully conducted using such a device by Juang et al. [22]. The authors perfused their device with MBs (both custom-made as well as commercially available) in growth medium using a syringe pump. As flow reached steady-state, insonation at f_c of 1 MHz for 5 s was conducted. This resulted in MB destruction with subsequent sonoporation of HUVECs, which was verified by propidium iodide (PI) (see Chapter 2.6.1). Figure 2.2j shows a single microfluidic channel realized in a device made of polyester and toner, with channel cross section of 2000 µm × 103 µm (width x height), suitable for HUVEC culture with viable cells up to 5 days [111].

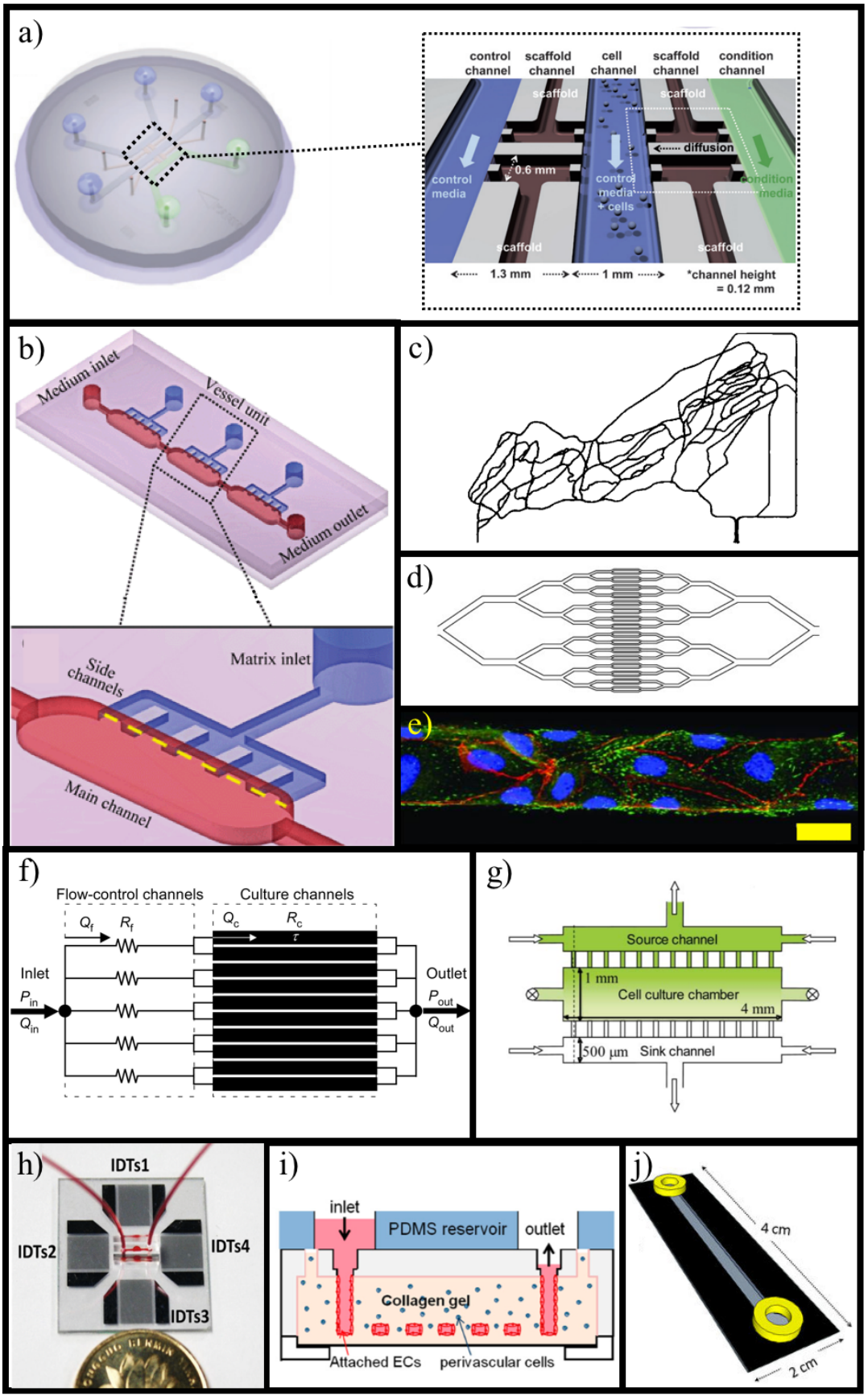

Figure 2.2: Microfluidic devices from the last decade, among which all except for **h** were used for endothelial cell culture. See next page for detailed captions.

Figure 2.2: a) Co-culture device suitable for endothelial and tumours cells where endothelial cells may migrate from ”cell channel” into ”scaffold channels”. Adapted from [83] with permission of The Royal Society of Chemistry. **b)** Device for studying tumour cell extravasation. An extracellular matrix (ECM) gel fills the side channels, and endothelial cells are cultured on the yellow dotted line. Tumour cells extravasate from main channel, across endothelial cells, into side channels. Adapted from [84] with permission of The Royal Society of Chemistry. **c)** Microfluidic channel design based on a computer mapped network of a native cremaster muscle. Adapted by permission from RightsLink Permissions Springer Customer Service Centre GmbH: Springer Nature, [100]. **d)** Microfluidic channel design of a branched network, reproduced from [99], with the permission of American Society for Clinical Investigation. **e)** Fluorescence micrograph of Human Umbilical Vein Endothelial Cells (HUVECs) cultured in a single microchannel 6 days after seeding, 25 µm scale bar. Adapted from [98] with permission by Mary Ann Liebert Inc. **f)** Microfluidic channel design with channels of varying height, suitable for endothelial cell culture in ”culture channels”. Reproduced from [101] with permission from Elsevier. **g)** Device suitable for endothelial cell culture in a ”cell culture chamber”. Source and sink channels enable gradients of biochemical cues. The small channels connecting the channels to the chamber are not drawn to scale. Reproduced from [108] with permission of The Royal Society of Chemistry. **h)** Device consisting a single cylindrical microchannel. Device allows generation of surface acoustic waves by interdigital transducers (IDTs), to induce sonoporation of individual cancer cells. Reprinted from [21] with the permission of AIP Publishing. **i)** Device with microchannels of collagen gel, suitable for endothelial cell culture in square channels. Was used to study e.g. thrombosis [87] and sonoporation [22]. Reproduced from [87], Copyright 2012 National Academy of Sciences. **j)** Device made from polyester and toner, comprising a single rectangular channel, suitable for endothelial cell culture. Adapted from [111] under the Creative Commons Attribution 4.0 International License [112].

The versatility of microfluidic systems allows expansion of the in vitro model to add various new dimensions. As already presented, microfluidic devices can be functionalized to allow co-culture of endothelial cells and tumour cells. This can be exploited to mimic the endothelial barrier and EPR effect, features that are crucical in drug delivery to tumours. Kwak et al. reported a microfluidic tumour microenvironment model with different device compartments and microchannels to represent a pair of blood and lymphatic vessels, and a compartment representing the tumour, as shown in Figure 2.3. The vascular channel, with cross section of 300 µm $\times$ 50 µm (width x height), lied on top of a 1 mm by 2.7 mm tumour compartment of 100 µm height. On each side of the tumour compartment, there was a 300 µm $\times$ 100 µm ”lymphatic channel”. By applying different pressures on the capillary, tumour and lymphatic compartments, the authors sought to simulate the complex hydraulic pressure conditions found in vivo. The goal was to use the device to study extravasation and subsequent tumour accumulation of polystyrene nanoparticles. By separating microvascular endothelial cells

and tumour cells (MCF-7 cell line) with a porous membrane of 400 nm pores, nanoparticles were allowed to flow through and extravasate from the vascular compartment into the tumour compartment, to mimic EPR-associated leaky vasculature in tumours in vivo. This exemplifies how microfluidic models allow consideration of a vaster context that extends beyond the single organ or cell type, to incorporate multiple physiological features found in vivo. Microfluidics augment traditional in vitro models and are especially powerful in simulating in vivo environments where liquid flow is important, such as in microvasculature.

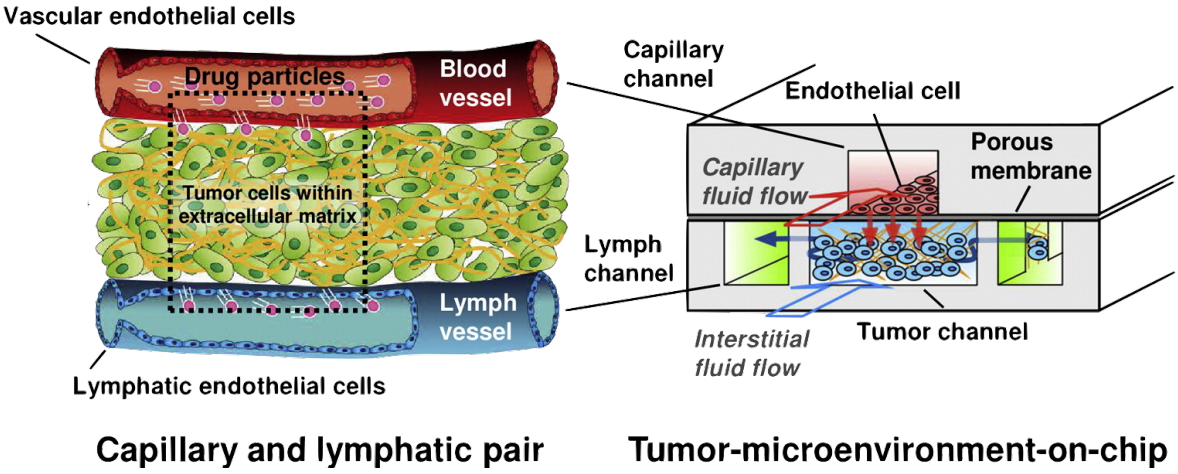

Figure 2.3: Schematic of a multi-compartment microfluidic tumour model incorporating tumour cells, endothelial cells and two lymphatic channels to mimic the tumour microenvironment and surrounding compromised endothelium. Endothelial cells and tumour cells are separated by a porous membrane to allow consideration of the enhanced permeability and retention (EPR) effect. Adapted from [113] with permission from Elsevier.

To date, the literature on microfluidic devices to study cells and MBs in acoustic fields is limited, including devices shown in Figure 2.2f and h along with sonoporation studies with single cavitating bubbles [114]. Lajoinie et al. reviewed the different in vitro systems that have been used to study (micro)bubble-cell interactions [115], not limited to MBs responding to US. A number of reports on cells and cavitation bubbles in microfluidic confinement exist, including single cell analysis of a laser-induced cavitation bubble interacting with cells in suspension, in a microfluidic confinement [23, 116]. The authors pointed out that these represent oversimplified models, and that despite the emergence of more sophisticated microfluidic cell culture models that allow physiological considerations such as flow and ECM, their application in studying MBs and cavitation bubbles is limited [115]. However, these considerations could be crucial

in order to gain insights that are translatable to the in vivo situation where cells interact with each other and ECM in 3D, and endothelial cells are subject to flow-induced shear stress. A previous study showed that MB-induced sonoporation of endothelial cells was greatly reduced if cells had been subject to culture under flow conditions, compared to a static culture [117]. Thus, microfluidic devices represent an enabling technology for studying MB-cell interactions under in vivo-like conditions. Despite the many opportunities, it is emphasized that this master project did not strive to develop a complex 3D in vitro model with high physiological relevance due to the limited amounts of time and materials. Instead, focus was dedicated to establishing a device that essentially allowed monolayer endothelial cell culture (although cell attachment may happen on the whole channel surface), and visualization of MBs during insonation.

2.5 Fabrication of a microfluidic vascular model

In general, microfluidic devices are most often fabricated from either a solid polymer material or glass, or a combination. As already mentioned, PDMS is by far the most common material. For cell culture purposes, the material has many favourable properties, including flexibility, optical transparency, gas permeability [118], low toxicity and its surface adsorption of ECM proteins like fibronectin [119]. Device fabrication, as will become evident, is both rapid and straight-forward. However, although PDMS would sound like the ideal material, there are adverse effects that should not be neglected, including permeability towards water vapor and small hydrophobic molecules, and possible interaction of un-cross-linked oligomers with cells [120]. As mentioned in Chapter 2.4.3, other materials are possible.

Rapid prototyping of PDMS based microfluidic devices is typically achieved from soft lithography replica molding, where PDMS is casted from a reusable mold that carries the desired pattern. The mold is typically prepared by a photolithography process on a silicon wafer, where the pattern in question is transferred to a film of photosensitive material (”photoresist”) coating the wafer. This happens by selective exposure to light at appropriate wavelength, often in the ultraviolet (UV) range, according to the desired pattern. Then, PDMS is casted from the

mold and bonded to a substrate (e.g. glass), before the device is functionalized to allow cell culture. A schematic showing this process flow, which was employed in this project, is given in Figure 2.4. All the steps are described in more detail in the following subsections.

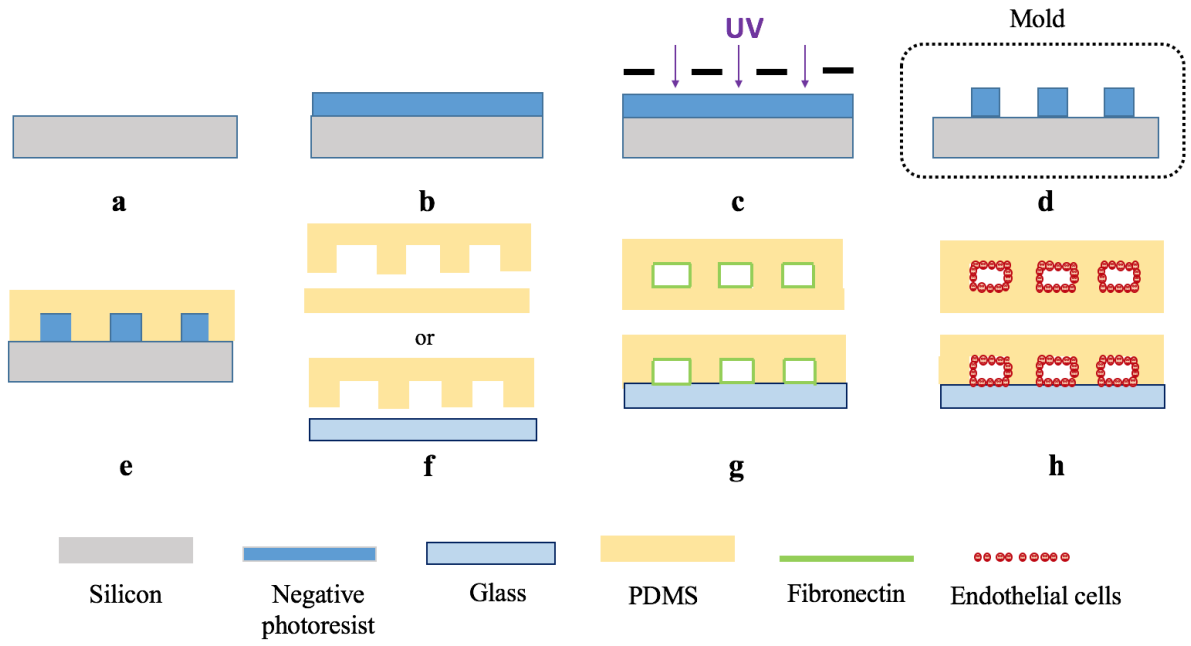

Figure 2.4: A flow chart illustrating the stepwise fabrication of a microfluidic system for endothelial cell culture. Steps **a-d** show a standard lithography process utilizing a negative photoresist to create a silicon mold that contains the inverse of the final pattern. Microfluidic pattern is transferred to a photosensitive material by selective ultraviolet (UV) light exposure (**c**), which hardens the material and yields a mold (**d**) for the device. Polydimethylsiloxane (PDMS) is then casted from the mold (**e**), inlets and outlets are created (not shown), before PDMS is bonded to a substrate (**f**) of e.g. glass or PDMS. Fibronectin is introduced in the channels (**g**) to facilitate endothelial cell attachment in the final step (**h**).

2.5.1 Photolithography

Photolithography is commonly associated with semiconductor manufacturing and integrated circuit industry, but is nevertheless widely employed in microfabrication in general for selective substrate patterning. The process involves several steps which can be optimized for a given material and application. Most photolithography processes include the following steps in the given order: 1) cleaning the substrate, 2) dehydration bake, 3) depositing photoresist, 4) soft bake, 5) exposure to (UV) light, 6) post exposure bake, 7) development and 8) hard bake.

The substrate, most often a silicon wafer, is first thoroughly cleaned, e.g. by spraying with solvents, exposed to plasma or etched in a corrosive solution. Then, dehydration bake is carried out to remove any excess moisture including adsorbed water molecules. These steps are necessary to ensure proper adhesion of photoresist. The photoresist is a polymer solution in an organic solvent that, upon exposure to (UV) light at appropriate wavelength, changes its solubility in a developer solution. Resists are fundamentally classified as either positive or negative, depending on whether light exposure breaks down the resist to increase solubility, or crosslinks the polymer component to decrease solubility, respectively. In fabrication of a microchannel mold, i.e. the inverse pattern of the microchannel, it is relevant to consider selective light exposure of a negative photoresist with subsequent removal of unexposed resist. The photoresist film thickness defines the depth, or height, of the microfluidic channels. To achieve channels of different heights as in Figure 2.2f, the photolithography process may be repeated for several cycles where photoresist is repeatedly deposited over previous resist layers [101]. The negative photoresist SU-8 is widely used in microfluidic device fabrication [97, 98, 101, 108, 110], but can in principle be any negative photoresist that allows the appropriate film thickness.

Photoresists may be deposited on the substrate by various means. A widely employed method is spin coating, where the resist is first deposited in the center of the substrate, which is subsequently spun at thousands of revolutions per minute (RPM). The centrifugal forces ensure even distribution of the photoresist towards the substrate edge by resist flow; higher RPMs yielding thinner films. Frequently, the manufacturer of the photoresist provides a spin curve for the specific resist, giving information about how resulting thickness varies with spin speed. The spin curve often follows a power relation of the form

$$t \propto av^b, \tag{2.20}$$

where t denotes film thickness, v is the spin speed given in RPM and a and b are constants. Typically, b has a value of around -0.5 [121]. Moreover, film thickness decreases with decreasing resist viscosity, and to some degree also the duration of the spin coating. Sometimes, especially for viscous resists, a ridge of resist on the wafer edge and back side can be observed,

known as the edge bead. Depending on the application, removal of edge bead can be crucial, which can be achieved by e.g. spraying an appropriate solvent on the underside of the wafer while spinning [122]. After coating, soft bake is carried out to evaporate excess solvents from the resist, improve its adhesion and relieve film stress.

The film is now ready for exposure. This step is most often performed with the aid of a photomask with areas that are transparent and opaque according to the pattern, hence the photomask has to be physically fabricated. However, light exposure in direct exposure systems that do not require photomasks also exist, such as the direct laser writing system (maskless aligner) that was used in this project. Such a system focuses a laser beam onto the resist and scans across the substrate according to a computer generated design. Following exposure, post-exposure bake is carried out to, depending on the resist type, initiate chemical reactions or improve resist adhesion and/or alleviate film stress [122]. Afterwards, a developer solution dissolves soluble areas of the resist to yield the final pattern. Depending on the application of the patterned substrate, a hard bake can be performed as a final step to harden the resist, prepare it for subsequent processing and remove excess developer and/or moisture.

2.5.2 Silanization

A non-stick silicon mold is desirable to facilitate removal of PDMS, achievable through silanization. The process involves coating the silicon wafer with a self-assembled monolayer of alkylsilane molecules, e.g. by creating covalent Si-O-Si bonds to the already present silanol group on the silicon surface through hydrolysis [123]. This decreases the affinity of PDMS to the mold.

2.5.3 PDMS soft lithography replica molding

To transform the mold pattern to PDMS, a mixture of liquid PDMS base and curing agent is poured onto the mold and subsequently solidified. The base contains vinyl terminated PDMS

oligomers which react with silicon hydride groups present in the curing agent, cross-linking the base to yield a solid elastomer [124]. The ratio between the amount of base and curing agent determines cross-linking density in the final material, which has implications on material stiffness, a lower base to curing agent ratio yielding a material of higher Young's modulus [125]. Curing is typically carried out at 60-65 °C overnight, or up to 24 h [97, 110], but can also be shortened down if the temperature is increased; 2 h at 120 °C [101] or 1 h at 80 °C [84] have been reported. Necessary curing time increases with PDMS thickness. Afterwards, the patterned PDMS slab is peeled off the mold, inlets and outlets are punched through the slab, and the slab is bonded to a substrate such as a clean glass slide or a slab of PDMS (Figure 2.4f). Other substrate materials are also possible, e.g. lithium niobate which was used by Meng et al. [21] (Figure 2.2h). All other PDMS microfluidic devices shown in Figure 2.2 had glass bottoms. To create an irreversably sealed device, plasma bonding is typically done [124] with e.g. oxygen plasma [97, 98]. In this process, surface active hydroxyl groups are created on the two surfaces (e.g. PDMS or glass) [124], which may undergo a condensation reaction to yield covalent Si-O-Si bonds between the two surfaces upon bonding. Remaining hydroxyl groups in the channels render the device hydrophilic, but PDMS hydrophilicity is unstable as low-molecular weight chains from the bulk of the polymer diffuse to the surface [126]. Especially storage in dry air post plasma treatment, leads to a continuous increase in hydrophobicity [126]. Hydrophilicity can however be maintained by allowing contact between the plasma treated PDMS surface and water or a polar organic solvent [124]. The plasma treatment may also improve surface adsorption of ECM proteins necessary for cell attachment (see Chapter 2.5.4) [127, 128].

2.5.4 Device functionalization for endothelial cell culture

Following fabrication, devices must be prepared for endothelial cell culture. Sterilization may be achieved by different means, including washing with 70 % ethanol [98, 129], autoclaving [83, 118], UV light treatment [84, 101, 130], or just relying on the plasma treatment from device bonding [97]. Channel walls are then coated with an ECM mimicking protein (Figure 2.4e) by injecting a solution with suitable concentration. The protein is immobilized to the channel

surface either by adsorption or covalent bonds [127]. Fibronectin is widely reported in microfluidic endothelial cell culture including HUVECs [97–100, 105, 111]. This glycoprotein is an ubiqutous ECM constituent that plays an important role in endothelial cell adhesion and survival [131]. It has been shown that HUVECs attach to this protein via the fibronectin receptor $\alpha_5\beta_1$ and possibly also $\alpha_v\beta_1$ integrins [132]. Moreover, fibronectin ensures more robust cell attachment so that cells do not detach under flow [105]. Other proteins such as collagen could also be used, but fibronectin has previously yielded more well-spread endothelial cells and resistance towards shear stress [133].

2.6 Relevant characterization techniques

Throughout the course of this project, several characterization techniques were employed to evaluate structures fabricated during photolithography optimization, final silicon molds, microfluidic cell culture and experiments with MBs. A brief theoretical background of the mentioned techniques will be presented in the following sections.

2.6.1 Optical microscopy

Techniques to magnify small samples using visible light and lenses have existed for centuries. Optical microscopy is still the main-stay method to study samples of size above the diffraction limit. Modern optical microscopes are typically compound microscopes, implying that magnification happens at two distinct systems of lenses. The main components of a compound microscope include a light source, eyepiece or ocular lens, objective lenses for magnification, a stage for the sample, focus knobs to adjust focus, a diaphragm and a condenser. The latter two are responsible for adjusting the size of the light cone and focusing the light beam onto the specimen, respectively. Two-step magnification happens as the initial magnification from the objective lenses creates an internal image in the microscope, which is further magnified at the eyepiece. From the eyepiece, the final image can be observed.

The most simple microscopy technique considers transmitted light where appropriate lighting conditions are crucial to achieve images of acceptable quality. In this sense, Köhler illumination is a method to achieve extremely even lighting of the sample. Moreover, there are distinct illumination techniques to achieve contrast. These include brightfield (contrast achieved by specimen light absorption), darkfield (contrast achieved by specimen scattering) and phase contrast (contrast achieved by optical interference). Today, more advanced optical microscopy techniques exist that evaluate other parameters than just the transmitted light of the specimen, including reflected light which is the method of choice for opaque samples such as semiconductors and metals, or emitted fluorescence light from fluorophores in the specimen.

2.6.1.1 Inverted microscopes

Inverted microscopes contain the same components as conventional microscopes, but have some of the components arranged differently. Light source, diaphragm and condenser are above the sample stage rather than below, and the objective is positioned underneath rather than above the sample stage. Moreover, the sample stage is fixed in the vertical direction, thus adjusting the focus involves moving the objective lens along the vertical axis. Inverted microscopes are popular in studying cell cultures as cells may be viewed at the bottom of a large culture flask or dish. In a conventional microscope however, samples would most often have to be deposited on a glass slide before inspection. Thus, inverted microscopes enable the observation of cells under more natural conditions.

2.6.1.2 Phase contrast microscopy

In phase contrast microscopy, one aims at transferring the phase differences of optical waves into observable contrast in the specimen, i.e. differences in light intensity. Optical waves interact with the sample, so that their phase and amplitude will depend on properties of the sample, which can be exploited to create contrast in an image. Specimen thickness and refractive index affect how the light interacts with it; for example, the amplitude changes if

the specimen absorbs or scatters the light. To understand this microscopy mode, one must distinguish between light waves transmitted straight through and unaffected by the sample (S-waves), i.e. the background light, and light waves that are diffracted and scattered in new directions (D-waves). The sum, or interference between these waves, is referred to as particle waves (P-waves). In this sense, contrast is manifested as an amplitude difference between the P and S-wave. Typically, in transparent, unstained specimens, the D-wave has low amplitude and is phase-shifted -90° relative to the S-wave. Thus, the S-wave and P-wave have nearly the same intensity, yielding low contrast, as seen in Figure 2.5a. Phase contrast microscopy enhances contrast by achieving constructive interference (high P-wave amplitude) in regions containing the sample, and reducing the amount of background light (low S-wave amplitude). In negative phase contrast microscopy, S-waves are phase-shifted -90° to be in phase with D-waves, yielding constructive interference. The process increases P-wave amplitude so that it becomes more distinguishable from the S-wave (Figure 2.5b). Higher P-wave amplitude yields increased brightness in areas containing the sample. This happens as the light passes through a ring-shaped aperture diaphragm (phase-shift ring) as given in Figure 2.5c. Furthermore, S-waves are dimmed by a gray filter to minimize background light. Assuming the specimen has a higher refractive index than its background, it will appear bright on a darker background in this mode. Alternatively, S-waves may be phase-shifted 90°, so that the net phase shift between S-wave and D-wave is 180°, to create positive phase contrast. This yields a dark specimen on a light background.

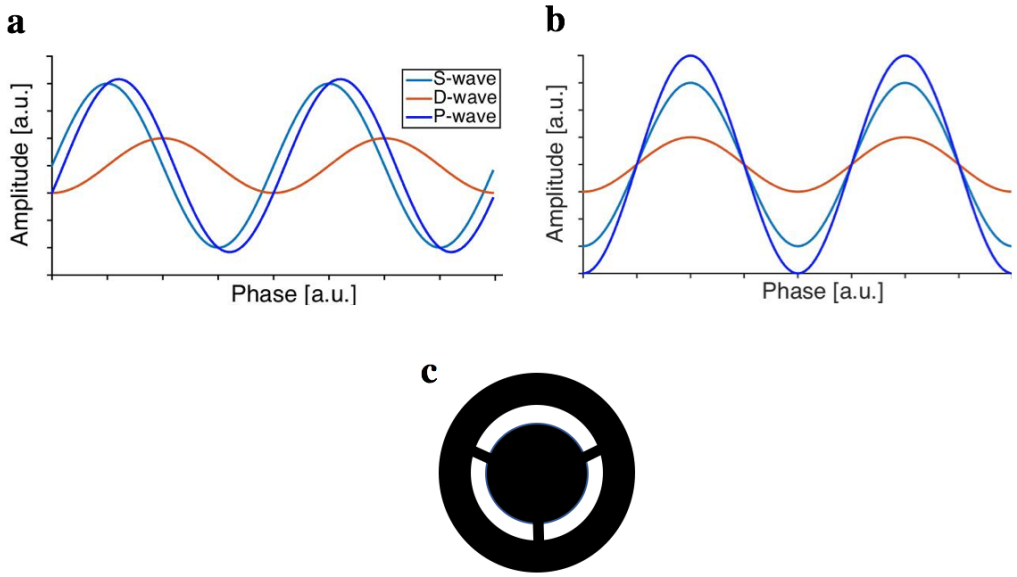

Figure 2.5: The fundamental principle of phase contrast microscopy relies on phase shifting background light (S-waves) so that it is in-phase with diffracted light (D-waves) to create amplitude difference between background light and its interference with diffracted light (P-waves). The example here shows how S-waves are phase-shifted by minus a quarter wavelength (-90°) from **a** to **b**. This happens as the light passes a phase ring, shown in **c**.

2.6.1.3 Fluorescence microscopy

Fluorescence is a phenomenon involving molecular absorption and subsequent excitation of photons, exhibited by molecules commonly referred to as fluorochromes or fluorophores. A molecule may absorb photon energy and be excited into higher energy states, both electronically (excitation of electrons) and vibrationally (excitation of phonons). Upon relaxation, i.e. returning back to the molecule's ground state, the absorbed energy may be emitted in the form of light, i.e. photons, known as fluorescent light. As some of the energy from the incoming excitation light will be lost to non-radiative transitions in the molecule such as vibrational relaxation, the emitted fluorescent light will always be of higher wavelength than the excitation wavelength. This phenomenon is known as Stoke's shift. Fluorescence is a property that can be exploited in microscopy by staining samples with fluorophores emitting light of visible wavelengths. In cell biology studies, fluorescence staining involves the specific binding of certain fluorophores to certain organelles, cytoskeleton proteins or DNA. Staining can also be a powerful tool in viability assays as some fluorophores are only able to enter apoptotic or necrotic cells, or must be activated by intra-cellular enzymes only live cells exhibit. Many fluorescence dyes are com-

mercially available, such as the DNA-specific blue dye 4,6-diamidino-2-phenylindol (DAPI), the viability marker calcein and the necrotic and apoptotic marker propidium iodide (PI). In other words, fluorescence microscopy involves the detection and localization of fluorophores.

To ensure the optimal contrast and excitation conditions, fluorescence microscopes contain many optical components. As most fluorescence microscopes including the one used in this project employ epifluorescence, we will consider the set-up of such microscopes, as visualized in Figure 2.6. Epifluorescence implies illumination from above the specimen. Firstly, the set-up must have an appropriate light source, often a mercury lamp, and an excitation filter ensuring that only light of the specific excitation wavelength irradiates the sample. To separate the excitation and emission wavelengths, short wavelengths are reflected by a dichroic mirror. Long wavelengths must pass an emission filter which further isolates the emission wavelength, which can be observed at the eyepiece or a camera detector. This way, light that was not emitted by excited fluorophores is reduced, and areas not containing fluorophores appear dark in the final image. The filtering components of fluorescence microscopes are contained inside filter cubes, which allow switching between filters of different wavelengths.

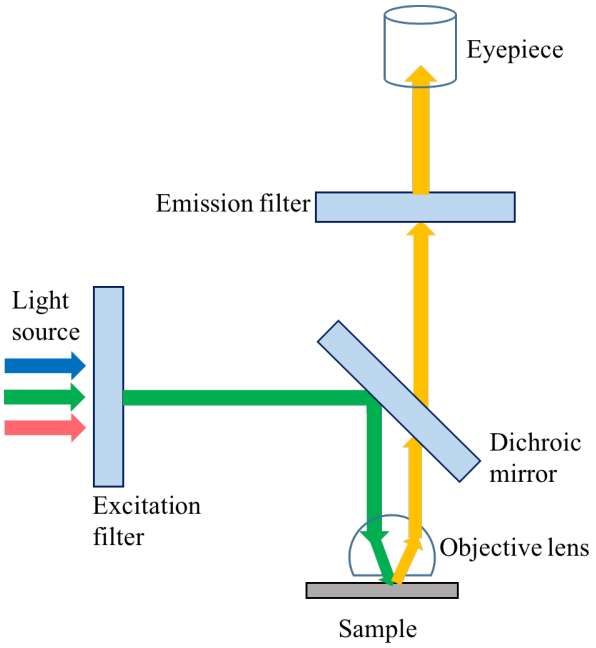

Figure 2.6: A simple schematic of epifluorescence microscopy, showing how different components ensure that excitation and emission light rays are separated, so that only excited light is detected.

The fluorescence dyes that were used in this project include calcein acetoxymethyl (AM) and PI. Calcein is fluorescent and has an excitation peak at 495 nm and emission peak at 515 nm (green light), but does not exhibit fluorescence when bound to the AM group. The AM group may however be hydrolysed by intracellular esterases once calcein AM passively crosses a cell membrane due to its lipid-solubility, leaving fluorescent calcein in the cytosol [134]. Calcein is polar and thus retained in live cells with little transfer between cells [134]. Hence, it is a viability marker. Although the esterase activity should be significantly higher in live cells, it must be noted that dead cells may release or retain some residual enzymes [135]. PI, on the other hand binds to DNA and RNA and is impermeable to the cell membranes of live and healthy cells. However, when the membrane is disrupted such as in the case of (sono)poration, the dye may enter the cell and has thus been used in several sonoporation studies [22, 136, 137], or as an apoptotic marker [138]. The fluorescence activity increases 20 to 30-fold once bound to DNA or RNA, with excitation and emission peaks at 535 nm and 617 nm (red light), respectively.

2.6.2 Scanning electron microscopy

Scanning electron microscopy (SEM) is a widely used imaging technique for sample features at the micrometer and submicrometer scale, with resolution not limited by the diffraction limit of visible light. The sample of interest is placed in a vacuum chamber and subject to a focused beam of electrons accelerated at voltage typically in the 1-30 kV range, which scans across the surface to gather information for each pixel in the final image. These primary electrons interact with the sample and give rise to secondary electrons which are emitted by atoms of the sample, and back-scattered electrons from the primary beam. Detection of both secondary as well as back-scattered electrons give rise to an image, and the amount of detected electrons allows image contrast by correlating pixel intensity to the number of detected electrons. Secondary electrons are mostly surface sensitive and allow edge contrast determined by sample topography, and they also enable higher resolution than back scattered electrons. On the other hand, back scattered electrons have much higher penetration depth into the sample where electrons in the inner volume may also escape. These electrons allow elemental contrast.

To avoid charging effects due to the electron beam, sample surface typically needs to be conductive, although some scanning electron microscopes (SEMs) such as environmental SEMs allow inspection of non-conducting samples without the need of vacuum in the specimen chamber. Sample preparation with metal deposition can however be both fast and straight-forward with a sputter coater, where a 10 nm layer of e.g. gold can be deposited in a matter of a few minutes.

2.6.3 Profilometry

Profilometers include a range of instruments of different operational principles used to characterize sample surface topography such as surface roughness or film thickness. The latter can be obtained by measuring the height difference between the film and underlying substrate. Generally, one can group profilometers in two categories, namely optical profilometers and contact or stylus profilometers. Optical profilometers include several optical techniques that consider differences in light path stemming from height differences, such as in interferometry. On the other hand, contact profilometers utilize physical probing of a surface with a stylus. Hence, probing microscopes such as atomic force microscopes and scanning tunneling microscopes are among the contact profilometers. The most simple contact profilometer, however, is just a regular stylus or mechanical profilometer. In brief terms, a diamond stylus is moved laterally across the sample surface, in contact with the surface, while a feedback system monitors the force exerted on the probe by the sample. As the feedback system aims at keeping a constant force at the stylus, the stylus deflects in response to interactions with the sample. This deflection is recorded by a detector and is used to plot sample surface height versus lateral position of the stylus, yielding surface topography.

2.6.3.1 White light interferometry

WLI is an optical profilometry method for characterizing surfaces and 3D structures based on studying the interference between light that is reflected from the sample and a reference light beam. Collimated light from a white light source is split into the reference beam and object beam (to be reflected from the sample) at a beam splitter. The reference beam travels a known distance in the reference arm, is reflected from a reference mirror, and combined

with the reflected object beam at the beam splitter. The resulting interference pattern, or interferogram, is imaged onto a charge-coupled device (CCD) camera which responds with a camera pixel of high intensity if the interference is constructive and vice versa. A simple schematic showing this process is shown in Figure 2.7. The interference is determined by the optical path difference travelled by the reference and object beams. Structural features on the sample surface give rise to this difference between the two light beams, and the interference pattern can be translated to height differences present in the sample. The interferogram can be visualized in a computer software and is manifested as alternating black and white stripes (see Figure 2.7), so-called ”fringes”, which correspond to areas of destructive and constructive interference, respectively, between the wavefronts of the reference and object beams. Fringe spacing corresponds to the path difference between wavefronts in the z-direction.

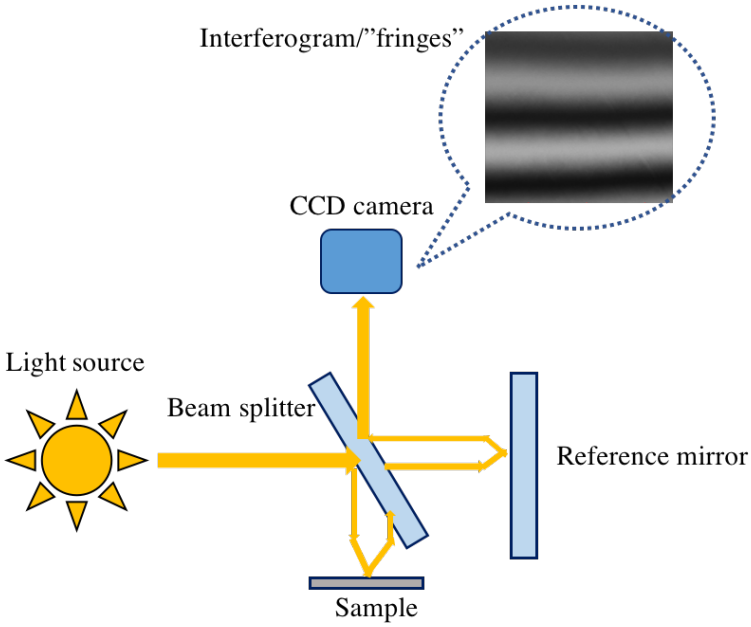

Figure 2.7: A simple schematic showing the light path during white light interferometry (WLI), an optical method for characterizing sample surface topography. The interferogram is imaged onto a charge-coupled device (CCD) camera.

The apparatus that was used in this project, namely Bruker Contour GT-K (Bruker Corp.), is a set-up combining WLI and optical microscopy in one single instrument. The apparatus has the configuration of a Mirau interferometer, i.e. the reference arm is located inside a microscope objective.

Chapter 3

Materials and methods

In sections 3.1, 3.2, 3.3 and 3.4, all work was performed in a cleanroom environment at room temperature unless otherwise stated.

3.1 Optimization of photolithography

Based on the results from the pre-master specialization project [1], preliminary microchannel heights of 50-100 µm (i.e. increased 2-3-fold from previously) were desired to reduce cell clustering and channel blockage during cell culture. This corresponds to the diameter of arterioles [139]. Photolithography processes to produce silicon molds of such height, i.e. resist thickness, proved to be difficult, and optimization was necessary to achieve a homogeneous coating and reduce edge bead. Moreover, a newly acquired photoresist was employed, and available data sheets with recommended processing parameters were not helpful in fabricating acceptable structures in the new thickness range. Suitable parameters in the different photolithography steps had to be determined with respect to the instruments that were employed in this project. Hence, many efforts were made to optimize the different parameters involved in photolithography towards developing a protocol for silicon mold fabrication. The following was investigated during the optimization process, with details about each step such as the instruments involved specified in Chapter 3.3.

- Two different photoresists of different viscosity (only specified for one of them by manufacturer) were used, namely mr-DWL 40 and mr-DWL 100 (Micro Resist Technology GmbH). The resists have equivalent chemical composition, however mr-DWL 100 is observably more viscous due to higher polymer concentration and/or molecular weight of polymer. While mr-DWL 40 was used in the pre-master specialization project and had a spin-curve available from the resist manufacturer, no such information was available for mr-DWL 100.

- Spin coating parameters were varied for both resists to determine resulting thickness, an acceptable edge bead as well as a uniform resist coating. Methods for quantifying resist thickness will be described in Chapter 3.2. In addition, attempts were made at measuring resulting edge bead with these methods, but it was later deemed sufficient to just inspect it visually by eye. mr-DWL 40 was spun on 2-inch silicon wafers and/or small silicon wafer pieces of $\sim$3 cm $\times$ 3 cm at speed in the 750-1100 RPM range (step size of 50 or 100 RPM) for 30, 45 or 60 s (decreasing time for increasing speed), at acceleration equal to $\sim$1/3 of the spin speed per second. These spin speeds were according to the spin-curve given by the manufacturer.

  It was found that a 3-step spinning process was desired to first distribute the resist at low speed and acceleration, then spinning to reach a certain thickness, before a final step at high speed and acceleration for a short period of time to remove the edge bead. An example of parameters that were tested for mr-DWL 40 is 1) 500 RPM for 30 s and an acceleration of 200 RPM/s, 2) 1500 RPM for 30 s with an acceleration of 500 RPM/s, and 3) 4500 RPM for 3 s with an acceleration of 3000 RPM/s. For mr-DWL 100, the 3-step process was also applied, and spin parameters in the two latter steps were varied. To investigate spin speed and resulting thickness, the resist was coated on 2-inch silicon wafers, and speeds of 2000, 2200, 2400 and 3000 RPM were tested for 60 s with an acceleration equal to 1/3 or 1/4 of the spin speed per second. To spin off the edge bead, speeds of 5400, 6000 and 6500 RPM were tested for about 3 s at acceleration of 3000-4000 RPM/s. Desired thickness was later specified to $\sim$60 µm based on evaluation of structures post exposure and development (see below), and feasibility to fulfill all the requirements.

The wafer cleaning procedure prior to spin coating was the same in all cases and is described in Chapter 3.3.

- Soft bake was according to the description in Chapter 3.3 and was performed either immediately after spin coating, or the day after where the resist was allowed to planarize overnight by placing the wafer in a closed wafer ship tray, on a levelled surface. It was found that planarization prior to soft bake reduced the edge bead.

- UV light exposure parameters were varied to find suitable values for exposure dose and defocus for a given resist and thickness. Defocus describes the location of the exposure laser's focal point in the z-direction and has implications on how light is distributed across the thickness of the resist. In the present exposure instrument (see Chapter 3.3), the defocus value ranges from 0 to 10, as defined by the manufacturer of the instrument. A value of 0 corresponds to a focal point present at the resist surface, while a value of 10 corresponds to a shift of 6 µm below the surface, i.e. into the resist. Such tests were conducted by exposing a small pattern relative to the wafer multiple times on a given resist-coated wafer, with a varying dose and/or defocus value each time. The pattern was a smaller and simplified version of the final microfluidic device pattern (see Chapter 3.3). Each wafer could thus be used to evaluate up to 42 combinations of dose and defocus parameters. Two wafers of each resist were subject to such tests, varying the dose from 700-1200 mJ/cm^2, 900-1400 mJ/cm^2, or 1000-2500 mJ/cm^2 with a step size of 100 mJ/cm^2. In addition, the defocus value was either kept constant equal to 0 or varied between 0-2, 0-6 or 1-8 with a step size of 1. All exposure was done at 405 nm wavelength as given by the manufacturer. Evaluation of exposure dose was done after the development step with the methods described in Chapter 3.2.

- For samples that were exposed, post exposure bake was initially carried out for 6 min at 90 °C with the temperature ramp described in Chapter 3.3. The baking time was later increased to 10 and 30 min to investigate if baking time affected the quality of the fabricated structures. It was found that an increased post exposure baking time gave better results.

- It can be expected that development time increases somewhat for increasing resist thickness. For each sample that was developed, the wafer was first developed for 5 or 5.5 min

and checked in a yellow light illumination microscope (see Chapter 3.2). In case the structures appeared underdeveloped, the wafer was developed for 1 min additionally, before inspection, and this was repeated until no more residual resist could be observed.

It is emphasized that not all combinations of the various parameters neither within nor across the different photolithography steps have been explored, as it was not necessary and would require excessive time and materials. Moreover, detailed results from the optimization process will not be presented in this thesis as reportable data acquisition was not prioritized.

3.2 Characterization of photolithography structures

To characterize structures resulting from photolithography, several techniques were used both during the optimization process as well as for the final silicon molds that will be described in Chapter 3.3.

- Resist thickness was initially evaluated by a stylus profilometer (Dektak 150, Veeco Instruments Inc.) during optimization. This was done by removing a small area of the deposited resist and measure the height difference between the wafer surface and the resist surface after soft bake. It was later found that WLI gave more accurate measurements with respect to SEM micrographs, hence the stylus profilometer was only used in the early stages of the optimization process.

- A light microscope (Axio Scope A1, Zeiss AG) with yellow light illumination equipped with an AxioCam ICc 3 camera (Zeiss AG) operated in reflected brightfield (epi-brightfield) mode was used to evaluate structures by visual inspection. In particular, this was done to determine if exposure parameters and development time were optimal. The objectives include a 5x objective (EC Epiplan, Zeiss AG) with numerical aperture (NA) of 0.13, or a 10x objective with NA = 0.2, imaging conducted under air.

- In contrast to the stylus profilometer, resist thickness quantification with WLI in a newly acquired Bruker Contour GT-K with Vision 64^{TM} software (Bruker Corp.) could only be carried out for samples that were subject to all photolithography steps prior to and

including development. This was done by using the Vertical Scanning Interferometry mode, using the 2.5x objective (NA = 0.07) at 0.55x and 1.0x camera zoom (High-Res camera mode) which yield a field of view of 3.5 mm × 2.6 mm and 1.9 mm × 1.5 mm, respectively. Measurements were controlled using the 20x objective (NA = 0.4) at 0.55x zoom. In final silicon molds, for each channel, at least three measurements were made at different locations along the channel length to study height uniformity. One measurement would provide a measurement region that covered the whole width as well as 1.4 mm of the length of the channel (2.5x objective, 1.0x zoom). In this region, the channel height at any point could be read by measuring the height difference between two arbitrary points or areas. For practical reasons, this was done manually as the accuracy was deemed sufficient. In addition, the measurement provided a 3D image of the channel with extrapolated side walls.

- SEM imaging was carried out to visualize feature profiles during optimization to evaluate exposure dose and development time. For acceptable sample size, wafers were first broken into pieces of ∼0.5 cm × 2 cm, before coating with a 10 nm layer of gold with the aid of a sputter coater (208 HR B, Cressington Scientific Instruments). Then, samples were loaded into a tabletop SEM (T3000, Hitachi Ltd.) and inspected at 500x magnification at 15 kV acceleration voltage, 73-75 µA emission current and 11.6-12 mm working distance. In addition, inspection in a more advanced SEM (APREO, FEI Co.) that allowed inspection of whole wafers was attempted for a silicon mold of mr-DWL 100 fabricated according to the protocol in Chapter 3.3. Despite varying the acceleration voltage and emission current, imaging could not be successfully carried out in this SEM due to significant charging effects and not enough time to optimize imaging in this project.

3.3 Silicon mold fabrication

Microfluidic channels were designed in a suitable photomask format (.cif) using the software CleWin 4.0 as shown in Figure 3.1. As the ultimate goal of the project was to mimic capillaries in vivo, channel cross section diagonals would have to be in the tens of micrometers range. However, based on the results from the pre-master specialization project, cell culture in

branched channel networks of such small cross section was very difficult due to cell clustering and transitions to high hydraulic resistance (in accordance with (2.18)). Hence, channels were entirely straight and widths were increased to 200, 400 and 600 µm to aid cell seeding and culture. A further measure to avoid cell clustering, based on the results from the pre-master specialization project, was to have a smooth transition between inlet/outlet and the channel itself without any sharp corners (see Figure 3.1). The circular inlets and outlets of all channels had a radius of 600 µm while the channel lengths were 2 cm. A single 2-inch silicon wafer yielded a mold for one of each channel.

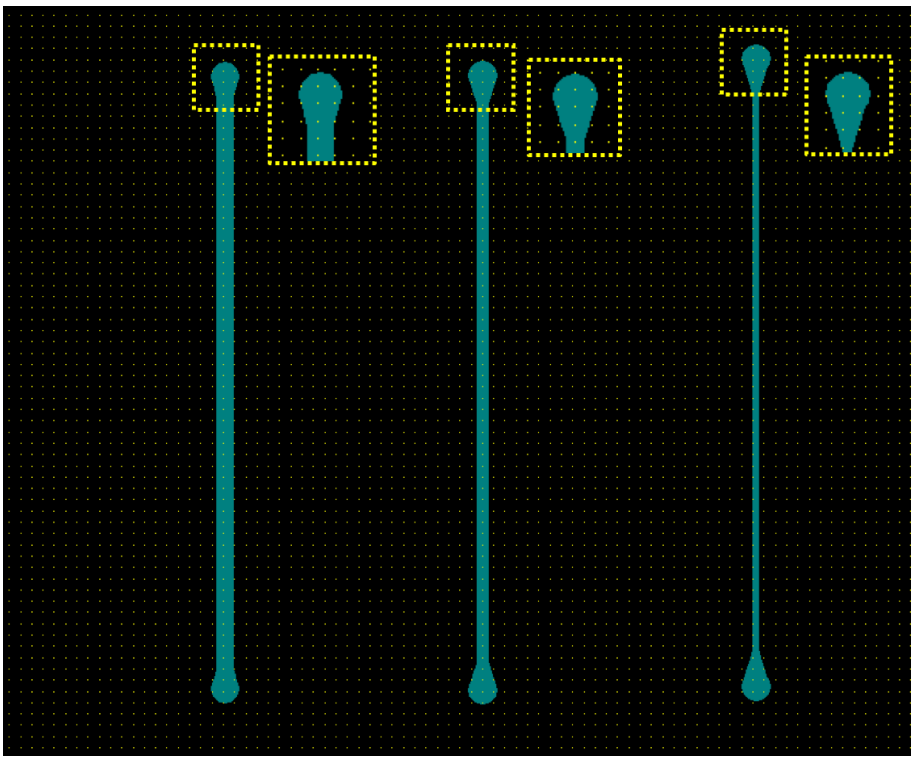

Figure 3.1: Screen shot from the photolithography mask design software CleWin 4.0 showing the three microchannel designs of 600, 400 and 200 µm width from left to right. All channels are symmetrical and have a length of 2 cm.

From optical inspection during the photolithography optimization process, it was concluded that acceptable structures following exposure and development were more achievable in the case of mr-DWL 100, and a final protocol to fabricate microfluidic device molds was established.

- The wafer was cleaned first by brief immersion in a bath of acetone followed by spraying with isopropanol from a squirt bottle, and blowdrying in a stream of nitrogen gas. To ensure complete removal of organic residues, the wafer was exposed to oxygen plasma at 100 SCCM and 20 kHz generator frequency for 3 min in a plasma cleaner (Femto, Diener Electronic GmbH).

- Dehydration bake was done at 180 °C for 25 min. The wafer was then cooled down to room temperature.

- A puddle of the negative photoresist mr-DWL 100 (Micro Resist Technology GmbH) was poured onto the substrate and spun in a spin coater (LabSpin6/8, SÜSS MicroTec AG) in three following stages: 1) 500 RPM for 30 s at 200 RPM/s acceleration to distribute the resist, 2) 3000 RPM for for 60 s at 1000 RPM/s to achieve a thickness of 55-60 µm, and 3) 6500 RPM for 3 s at 3500 RPM/s to spin off the edge bead. It was however later revealed that a reproducible resist thickness was unachievable even with the spin coating settings kept constant, see Chapter 4.1.

- Soft bake was performed by placing the wafer on a hot plate with a temperature of 50 °C, and the temperature was gradually ramped up to 90 °C with a rate of 5-10 °/ min to reduce stress in the resist. The wafer was then left at 90 °C for 25 min before the temperature was ramped down to 50 °C with a rate of 1-4 °/min by simply changing the set temperature to 40 °C. The wafer was then cooled down to and stored at room temperature for 2-16 h, for rehydration before exposure.

- Exposure was carried out by uploading the mask file to the software of a MLA150 Maskless Aligner (Heidelberg Instruments Mikrotechnik GmbH), with exposure at 405 nm wavelength, 1200 mJ/cm^2 dose and defocus value of 0.

- Post-exposure bake was done immediately after exposure and was identical to the soft bake step. The wafer was then allowed to relax overnight prior to development.

- Uncrosslinked mr-DWL 100 was removed by two times immersion in a bath of mr-Dev 600 developer solution (Micro Resist Technology GmbH), first for 5.5 min and then 1 min in an additional beaker to remove resist residues, under continuous stirring. After each de-

velopment step, the wafer was rinsed with isopropanol from a squirt bottle before drying with nitrogen gas.

- Hard bake was performed immediately after development by baking the wafer at 135 °C for 25 min, based on recommendations for mr-DWL 40 from the manufacturer. The same temperature ramp as during soft bake and post-exposure bake was done.

- Silanization was carried out by placing the wafer pattern side down on a Petri dish shaped piece of aluminium foil, in a polystyrene Petri dish bottom. Inside the aluminum dish, 2-3 drops of 1H,1H,2H,2H-perfluorododecyltrichlorosilane (Sigma Aldrich Norway AS) were deposited, and the Petri dish was left in a vacuum desiccator for 20 min. The aluminium foil was then removed and the wafer was kept in the vacuum dessicator for 10 min additionally before rinsing with isopropanol and blowdrying in a stream of nitrogen to remove excess silane.

3.4 PDMS soft lithography replica molding

As the patterned PDMS slab could be bonded to different substrates, two types of devices were realized in this project. Devices that had a glass substrate as channel bottom are referred to as G-devices, being equivalent to the ”PG-devices” that were fabricated in the pre-master specialization project [1]. However, as it was believed that glass would reflect US significantly and affect subsequent insonation experiments, PDMS-coated Mylar® sheets (plastic film based on polyethylene terephthalate) were used as alternative substrates [140]. With Mylar® sheets, insonation from both the top as well as the bottom surface of the devices could be carried out, hence most subsequent experiments were conducted using such devices which are referred to as M-devices. Both PDMS and glass substrates proved to be suitable substrates for HUVEC culture in the pre-master specialization project, and Annemieke van Wamel and Sigrid Berg have previously documented that PDMS has proven to have little attenuation towards US [1]. The terms ”(microfluidic) device”, ”microchannel” and ”channel”, as well as ”substrate” and ”(channel) bottom”, are used interchangeably.

PDMS was casted and bonded according to the following protocol:

- The silicon mold was placed pattern side up in a polystyrene Petri dish and would be secured by cured PDMS on the edges from the first time of use.
- To cover one mold, 7 g PDMS base from a Sylgard® 184 Silicone Elastomer Kit (Dow Corning Corp.) was mixed with 0.7 g curing agent from the same kit, in a plastic cup with the aid of a plastic spoon.
- The mixture was placed in a vacuum desiccator for 20-30 min for gas removal.
- Dust and particles were removed from the mold surface by a stream of nitrogen gas. The PDMS mixture was then poured over the silicon mold and remaining gas bubbles were removed with the aid of an air dust blower.
- PDMS was cured by placing the whole Petri dish in an oven for 3.5 h at 80 °C or 6.5 h at 65 °C, which was enough time for it to solidify. Curing time and temperature were increased from the pre-master specialization project [1] to ensure absence of uncrosslinked oligomers.
- Cured PDMS was peeled off the mold and cut with a scalpel to realize individual devices. A 1 mm blunt biopsy punch was used to create inlets and outlets, which were punched at an angle ($\sim 45°$) to aid liquid injection. Scotch tape was used to remove residual PDMS, and the patterns were also covered with tape to prevent dust deposition prior to bonding.
- A $\sim$7 cm $\times$ 8 cm piece of 76 µm thick Mylar® sheet (CS Hyde Co.) was glued to a plastic frame, wiped with 70 % ethanol and dried in a stream of nitrogen gas. The piece was then covered with $\sim$5 g PDMS base and $\sim$0.5 g curing agent prepared as above, with the aid of a plastic spoon, and cured at 65 °C for 2 h. To be able to fit M-devices inside Petri dishes and reuse the plastic frames, Mylar® sheets were peeled off the frames after curing and each sheet was cut into 3-4 pieces for individual devices. The PDMS surface was covered with tape to avoid dust deposition prior to plasma treatment.
- Glass slides for G-devices were wiped with 70 % ethanol and blowdried in a stream of nitrogen.

- PDMS pieces (pattern side up), glass slides and Mylar® sheet bottoms (PDMS coated side up) were placed in aforementioned plasma cleaner and exposed to oxygen plasma at 160 SCCM and 32 kHz generator frequency for 1 min. It was assumed that the plasma exposure would sterilize all exposed surfaces.

- Immediately after plasma exposure, PDMS slabs and glass slides (G-devices) or Mylar® sheet bottoms (M-devices) were bonded together by placing plasma exposed surfaces in contact with each other and pressing gently. The outside of the device was then wiped with 70 % ethanol.

Pictures of a final G- and M-device are shown in Figure 3.2.

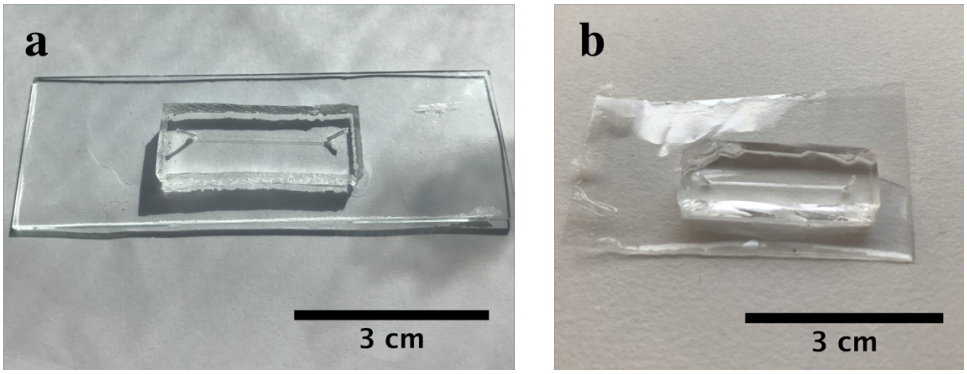

Figure 3.2: Pictures of final microfluidic devices fabricated from soft lithography replica molding. **a)** A 400 µm wide, 2 cm long and 59-64 µm (see Chapter 4.1) high channel with a glass slide comprising the device bottom (G-device). **b)** A 600 µm wide, 2 cm long and 59-72 µm (see Chapter 4.1) high channel. The device bottom consists of a polydimethylsiloxane covered piece of Mylar® sheet (M-device).

3.5 Preparation of cells

In the following sections, all handling of cells was conducted in a sterile environment except for during incubation, imaging and sonoporation studies. Only incubation was not performed at room temperature.

3.5.1 Human Umbilical Vein Endothelial Cells

Prior to microfluidic culture, HUVECs (Lonza Group Ltd.) in passage 4 were thawed by placing a cryo vial of cells in an empty nitrile glove that was sprayed with ethanol on the inside and placed in a 37 °C water bath for 2-3 min. Any instance of growth medium in relation to HUVEC refers to growth medium prepared from Clonetics® EGM™-2M SingleQuots™ Kit (Lonza Group Ltd.) pre-heated to 37 °C unless otherwise stated. The growth medium was supplemented with 2 % fetal bovine serum (Sigma Aldrich Norway AS), 1 % penicillin-streptomycin (Sigma Aldrich Norway AS), and various growth factors including vascular endothelial growth factor. Using a 5 mL pipette, HUVECs were transferred from the cryo vial to a TC75 flask (VWR International) that contained 15 mL growth medium, and incubated in a 5 % CO_2 incubator with temperature of 37 °C and humidity of $\geq$95 %. All instances of incubation refer to the mentioned incubator. HUVECs were left in the incubator overnight before the medium was changed. Change of medium was done every second or third day by adding 10-15 mL growth medium to the flask, and splitting of endothelial cells was done upon observation of (nearly) confluent cell layers. To split cells, old growth medium was first removed by vacuum suction. HUVECs were then washed with 5 mL of 37 °C phosphate buffered saline (PBS), which was removed before 3 mL of pre-heated (37 °C) trypsin was added for cell detachment. Cells were incubated for 2-3 min before 10 mL growth medium was added and cells were transferred to a centrifuge tube and centrifuged at 1500 RPM for 5 min. After removing the supernatant by vacuum suction, growth medium was added to achieve a desired concentration, and 0.3 million HUVECs were transferred to a new flask containing 10-15 mL growth medium. Preparation and culture of HUVECs prior to microfluidic culture were mostly conducted by PhD candidate Melina Mühlenpfordt.

3.5.2 Human prostatic adenocarcinoma cells

For practical reasons throughout the project, as the amount of HUVECs available was very scarce, the human prostate cancer cell line PC3 was used additionally for microfluidic culture as a more robust cell line. Although different from endothelial cells, the PC3 cell line is an

adherent cell type that also adheres to fibronectin via β_1-integrins [141], and was believed to behave similarly to HUVEC in microfluidic devices, with respect to short-term cell culture and subsequent sonoporation experiments. In other words, it was believed that successful experiments with PC3 could be somewhat translatable to culture with endothelial cells. This matter will be further discussed in Chapter 5.1.2.

PC3 cells (American Type Culture Collection) were cultured in T75 flasks with Gibco^{TM} Dulbecco's Modified Eagle Medium (Life Technologies AS) supplemented with 10 % fetal bovine serum (Sigma Aldrich Norway AS) and 1 % penicillin-streptomycin (Sigma Aldrich Norway AS). Any instance of growth medium in relation to PC3 cells refers to said medium pre-heated to 37 °C. Cells were split upon confluence according to the protocol of Chapter 3.5.1 except that 1.2 or 1.3 million cells were transferred to a new flask. The growth medium was changed every second or third day by removing the old medium by vacuum suction and adding 10-15 mL to the flask.

3.6 Microfluidic cell culture

In the following sections, the term "microfluidic cell culture" denotes any microfluidic device seeded with cells (HUVEC or PC3) irrespective of how long time was allowed between cell seeding and subsequent experiments. Devices that were used for cell culture were stored in polystyrene Petri dishes, always with the top surface where the inlet and outlet were present facing up. Channels of all widths were used, and the specific height of a given channel was not noted as it was regarded as uninteresting (however between 59 and 72 µm, see Chapter 4.1). Any injection of liquids into channels, including cell suspension, was carried out using a micropipette as this was deemed most optimal based on previous experiences [1]. In the following sections, unless otherwise stated, any injection of liquid refers to the following: the micropipette was inserted into an inlet while pressurized, before emptying until a droplet was visible at the outlet. Then, the pipette was withdrawn while still pressurized, depositing an additional droplet at the inlet. The terms inlet and outlet do not refer to any specific entrance to the channel.

All channels were coated with fibronectin before HUVECs or PC3 were seeded, and all liquid injection was carried out the same day as device bonding to maintain channel hydrophilicity upon liquid injection, reducing the likelihood of air bubbles [1]. To coat channels with fibronectin, 10-25 µL of 5 µg/mL fibronectin in PBS solution at 4 °C was injected into each channel according to the procedure described above. For PC3 cells, a concentration of 10 µg/mL was additionally used, to find an optimal concentration. Devices were then incubated for 40-60 min.

10-25 µL HUVEC or PC3 cell suspension was injected. HUVECs were in passage 5-8 and had concentration of 10 million cells per mL. PC3 cells were injected at 10 or 20 million cells per mL concentration, to find a suitable concentration. Cells were first injected until a droplet (containing displaced fibronectin solution) was visible on top of the outlet, which was removed by a disinfectant wipe. Then, the remaining cell suspension in the pipette tip was injected into the channel from the outlet to stop the flow, creating an additional liquid droplet on top of the inlet. The two liquid droplets on the outer device surface were then connected by a fluid line of $\sim$100 µL pure growth medium to ensure zero flow in the channels, allowing cells to attach. Devices were then immediately placed in the incubator. For HUVECs, unattached cells were flushed out by injecting new medium the day after seeding. This was deemed unoptimal for PC3 cells (see Chapter 4.4).

In some cases with HUVECs cultured in G-devices for several days, the medium would be renewed every 24-48 h. This was carried out by first flushing out cell debris by injecting 20 µL growth medium until a droplet was visible on top of the outlet, which was wiped away by a disinfectant wipe. The pipette tip containing the remaining medium ($\sim$15 µL) was then left in the inlet and an empty pipette tip was placed in the outlet, allowing the medium to be renewed by gravity-driven flow according to (2.19). Pipette tips were then cut to allow storage in a Petri dish. It would take approximately two days for the two fluid columns to be of equal height, which corresponds to a medium exchange of about 70 times the volume of a 400 µm wide channel.

3.7 Optical inspection

An optical microscope was used to evaluate microfluidic cell culture and insonation experiments with MBs. All imaging was conducted with an inverted microscope (Eclipse TS100, Nikon Corp.) coupled to a Zyla 5.5 sCMOS camera (Andor Technology Ltd.), operated in phase contrast mode, unless otherwise stated. Imaging was done under air and Nikon Plan Fluor objectives of 10x and 20x magnification were employed, with NA = 0.13 and 0.3, respectively. Devices containing cells would be imaged while inside a polystyrene Petri dish. Except for during insonation experiments that will be described in Chapter 3.8.3, microfluidic devices were always imaged with the channel bottoms facing the objective.

3.7.1 Fluorescence microscopy staining and imaging

Fluorescence imaging was carried out by coupling the mentioned inverted microscope to a universal illumination system (pE-4000, CoolLED Ltd.), using the aforementioned objective of 10x magnification. A 600 µm channel of a G-device was stained with 1 µM calcein AM (Life Technologies AS) in growth medium at 4 °C 1 day post seeding of HUVECs by injecting ∼20 µL. The device was put in an aluminium foil wrapped polystyrene Petri dish and incubated for 40-60 min before imaging with a 490 nm excitation wavelength. PC3 cells were not stained with calcein due to all channels being used for subsequent sonoporation experiments where PI staining was instead carried out, as will be described in Chapter 3.8.2.

3.8 Studying microbubbles in microfluidic devices

Throughout the rest of this thesis, ”MBs” refer to both Sonazoid^{TM} as well as ACT bubbles. In the following sections, all experiments were carried out with M-devices of 59-72 µm height and 400 and 600 µm width. Injection of MBs was done as in Chapter 3.6. All handling of test items

was conducted at room temperature under non-sterile conditions unless otherwise stated. The same conditions apply for the experimental set-up that will be described in Chapter 3.8.3.

3.8.1 Preparation of microbubbles

MBs were prepared for two distinct experiments: 1) to study the behaviour of MBs inside microchannels and 2) to study how they interact with PC3 cells. In the former experiments, empty M-devices were employed in order to isolate MBs from cells and cell debris for improved image quality. Each channel was first washed with 37 °C water degassed by boiling and PBS before injecting MBs, allowing channels to be reused. The behaviour of both bubbles was assessed qualitatively from videomicroscopy as will be described in Chapter 3.8.3. In addition, the size (diameter) of ACT bubbles was evaluated (see Chapter 3.8.4). Preparation of test items to evaluate MB behaviour will be described below.

Sonazoid™

For Sonazoid™, an 18G needle was first inserted into the rubber stopper of a vial containing 2.4×10^9 freezedried Sonazoid™ MBs (GE Healthcare AS) for venting purposes before 2 mL PBS at 37 °C was injected into the vial by a syringe, through another 18G needle. The contents of the vial were then homogenized by gently flipping the vial 180° back and forth, 1-2 times a second, for approximately 30 s. Afterwards, 10 µL of the solution, in addition to a dilution of 1:3 (bubble solution to 37 °C PBS), was carefully injected into each channel.

Acoustic Cluster Therapy (ACT)

The ACT compound (i.e. the ACT cluster dispersion) was provided by Phoenix Solutions AS and has been used previously by several authors [9, 61, 62, 142, 143]. ACT compound consisted of the US contrast agent Sonazoid™ (GE Healthcare AS) reconstituted with 2 mL microdroplet dispersion (3 µL/mL) at room temperature to yield $\sim 1.2 \times 10^9$ MBs per mL and 0.3-1.1 $\times 10^9$ microdroplets per mL. Preparation of the ACT compound was identical to Sonazoid™ MB so-

lution, except for adding microdroplets rather than PBS to a Sonazoid™ vial. Microdroplets consisted of perfluoromethylcyclopentane stabilized with a distearoylphosphatidylcholine phospholipid membrane, with 3 % (mol/mol) stearlyamine, dispersed in 5 mM TRIS (2-amino-2-hydroxymethylpropane-1,3-diol) buffer. A dilution of 1:3 in 37 °C PBS solution was studied.

3.8.2 Microbubble-cell interactions in microfluidic devices: sonoporation

To prove that the M-devices could be used to study MB-cell interactions, sonoporation was deemed a suitable parameter to study by considering uptake of PI through porated cell membranes, as mentioned in Chapter 2.6.1.3. Experiments were carried out 1 day after seeding in M-devices containing PC3 seeded at 20 million cells per mL, as it was found that this concentration would yield the most optimal cell layer for PC3 (see Chapter 4.3). For both Sonazoid™ and ACT bubbles, the MB dispersion was prepared and injected as in Chapter 3.8.1, however under sterile conditions, and diluted 1:3 with PI in PBS solution (25 µg/mL) at 37 °C.

As there were only a few channels with acceptable cell layers, no control experiments were done and channels had to be used multiple times and cells would be washed with 37 °C growth medium between subsequent injections of bubbles. It was assumed that one experiment would not be affected by the previous, and a given channel was only used to study one type of MBs. Videos were recorded for all sonication events as will be described in Chapter 3.8.3. As sonoporation was expected to be manifested as an increase in fluorescence signal, the microscope was switched to fluorescence mode whilst recording at certain time points to evaluate sonoporation. The same imaging equipment as in Chapter 3.7.1 was used, with 550 nm excitation wavelength. For Sonazoid™, fluorescence micrographs were also captured 2 min after insonation had stopped to determine if the signal changed with time.

3.8.3 Insonation and imaging set-up

The experimental set-up involved wrapping the device in a nitrile glove to protect the microscope from water before placing directly on the sample stage after injection of the MBs to be studied. In all cases, the device was placed so that the PDMS slab faced the objective lens (i.e. upside down with respect to the Mylar® sheet bottom) and insonation was carried out from above, through the Mylar® sheet. To create a water bath for insonation, two plastic cups lacking their bottoms were sandwiched with plastic foil in between and filled with 37 °C degassed water prepared by boiling, and placed on top of the Mylar® sheet of the device. Water was deposited on top of the Mylar® sheet to ensure that no air was trapped between the device and the plastic foil. Videomicroscopy was carried out at 15 fps or 25 fps according to the description in Chapter 3.7 at 10x and 20x magnification, the latter only used for Sonazoid™. The terms ”image” and ”micrograph” in relation to insonation experiments refer to a single frame from a video. All experiments were conducted under zero flow conditions to be able to track individual MBs and obtain acceptable image quality. A schematic of the experimental set-up is shown in Figure 3.3.

Insonation of Sonazoid™ and activation of ACT clusters

Experiments with Sonazoid™ as well as activation of ACT clusters were conducted by placing a clinical broad-bandwidth phased array probe (Vscan™, GE Healthcare AS) in the water bath, which has been used previously for activation of ACT clusters [61, 62, 143]. The transducer had $f_c = 2.5$ MHz and nominal MI = 0.8 (PNP of 1.2 MPa). Actual MI, however, was previously measured by a calibrated hydrophone to be $\sim$0.4 with a PNP of 0.6 MPa [143]. The frame rate, i.e. the pulse frequency, was 20 Hz. Duration of insonation was 45 s as previously [1, 61, 62, 143] (but in practise up to 46-48 s).

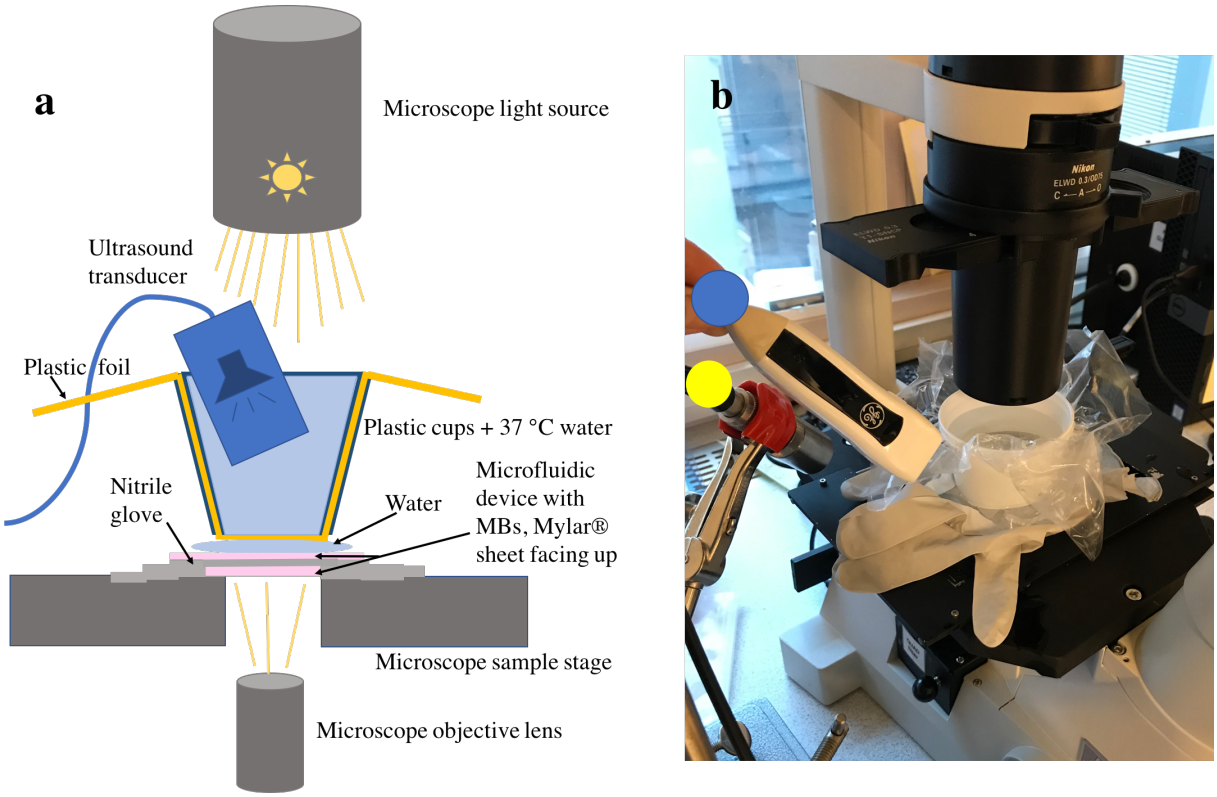

Figure 3.3: a) Schematic of the set-up used in insonation experiments where an M-device containing microbubbles (MBs) is wrapped in a nitrile glove and placed on the microscope sample stage so that the Mylar® sheet faces the light source and the inlet and outlet face the objective lens. Two plastic cups and a piece of plastic foil comprise a water bath for insonation, wherein the transducer can be placed approximately 3 cm away from the device. **b)** Photograph of the set-up where the Vscan^{TM} transducer used for activation of ACT clusters and insonation of Sonazoid^{TM} is annotated by a blue circle. The yellow circle denotes the transducer used during low frequency enhancement of ACT bubbles.

Low frequency enhancement of ACT bubbles

The enhancement step was carried out within 1 min after activation had stopped by placing an immersion transducer (I7-0012-P-SU, Olympus Corp.) in the water bath and sonicating for 2 min. The transducer was excited by a function/arbitrary waveform generator (33522A, Agilent Technologies) operated at 500 kHz, amplitude of 248.5 mV_{pp}, cycle count of 2 and burst period of 1 ms, coupled to a radio frequency power amplifier (2100L-1911, Electronic Navigation Industries) with 50 dB nominal gain and 100 W output power. The MI was later measured to be 0.5 by Petros Tesfamichael Yemane.

3.8.4 Image analysis

ImageJ (Fiji) [144] and Microsoft Excel were used in image analysis, the latter for data processing. ACT bubble diameter was evaluated by using the ”Analyze particles” tool in ImageJ after applying appropriate threshold values for optimal contrast, which had to be done differently for all images due to varying image quality. The tool identifies ACT bubbles as circular particles, based on appropriate size and circularity constraints, and returns the planar circular area of each ACT bubble. As a lower cut-off, particles below 4.37 µm were ignored, consistent with ACT bubbles having a size of 6 µm after $<$100 ms [61]. In cases where the image quality was insufficient with respect to particle detection, bubble outlines were adjusted manually for higher accuracy. ACT bubble diameter was measured 1, 30, 40 and 45 s after onset of activation (which lasted for a total of 45-48 s). In addition, ACT bubbles were studied 5 min after enhancement subsided to evaluate any change in bubble size and number of bubbles.

To evaluate fluorescence intensity in sonoporation experiments, the image type was first converted to 8-bit (greyscale), and the ”Histogram” function in ImageJ was used to count the number of pixels of each pixel intensity (i.e. grayscale value). To compare fluorescence intensity, images with equal fluorescence spots, i.e. cells, in focus were selected and the brightness and contrast were adjusted identically, and in each case the mean intensity of two frames was taken. Degree of fluorescence was defined as the number of pixels in a given area with value greater than the highest intensity value in the background, where no fluorescence was visible by eye.

For Sonazoid™, sonoporation was assessed as the presence of sonoporated cells, giving off distinct fluorescence spots in the micrographs, relative to the total number of PC3 cells in the field of view. If the number of sonoporated cells could not be determined, it was attempted to evaluate the change in fluorescence intensity instead.

For ACT bubbles, presence of sonoporated cells after activation was assessed qualitatively by creating overlap images of phase contrast and fluorescence micrographs, respectively. It was

in general difficult to relate fluorescence signals to certain individual cells due to unoptimal video quality and substantial fluorescence signals from non-viable cells present from before activation, that in most cases could not be isolated or discriminated from signals appearing during activation or low frequency enhancement. Moreover, whether additional cells were sonoporated during enhancement was inconclusive and assumed to be negligible, as it was expected that any sonoporated cells would already be proximal to ACT bubbles following activation. Sonoporation during enhancement was therefore evaluated by considering the change in fluorescence signal, by evaluating the total number of fluorescence pixels in a selected area. It was not feasible to only consider the fluorescence signals in the proximity of ACT bubbles with the available data. To account for the background of non-viable cells present from before insonation experiments, as well as any possible additional uptake of PI not resulting from interactions with ACT bubbles, a relative change in intensity was found for each micrograph. This was, whenever possible, done by considering the fluorescence intensity in an area with non-viable cells located at least a bubble diameter away from the closest ACT bubble. The change in this background intensity was then subtracted from the overall change in intensity. It is emphasized that the analysis is rather semi-quantitative due to all sources of error associated with the poor video quality.

Chapter 4

Results

4.1 Photolithography optimization and silicon molds

Among the characterization techniques, optical inspection was crucial in order to determine optimal exposure parameters in photolithography, and WLI measurements of final molds enabled evaluation of the reproducibility of feature heights. Optical inspection of structures following dose and defocus tests did not yield a correlation between dose and defocus, and subsequent appearance of structures. Different combinations of dose and defocus values appeared to give very similar results, and several combinations of parameters on a single test wafer yielded structures of acceptable appearance. An example of a typically under-exposed and hence unacceptable structure is shown in Figure 4.1a for 73-77 µm thick mr-DWL 40 exposed at 1000 mJ/cm^2 with a defocus value of 7. The unevenness and features on the resist surface could only be qualitatively evaluated. Note that this structure is designed differently from the microfluidic channels, for practical reasons. On the other hand, the appearance of structures upon more suitable exposure parameters can be seen in Figure 4.1b-c. Figure 4.1b shows a sample from the same dose and defocus test (i.e. same resist-coated wafer) as in Figure 4.1a with the same dose, however a defocus value of 3. Like the structure in Figure 4.1a, there is some unquantifiable unevenness on the surface. An equivalent result was obtained with 1100 mJ/cm^2 dose and defocus value of 1. However, lower defocus value did not necessarily produce better results for all doses in the different tests. Figure 4.1c shows a 400 µm wide

channel on a microfluidic mold (i.e. mr-DWL 100 processed according to Chapter 3.3) where the transition from inlet/outlet is depicted. Compared to Figure 4.1b, surface unevenness is less pronounced, which was a general observation for mr-DWL 100 versus mr-DWL 40.

For all structures including silicon molds, optical inspection indicated that features were not perfectly vertical due to the presence of ”skirts”, visible in Figure 4.1a-c as shadowy features around the outlines of the structures. Initially, it was believed that these features were due to underdeveloped resist protruding at the base of the structures. Skirts were however observed throughout the whole optimization process, despite using different microscope objectives and varying exposure parameters, resist thickness and even prolonging the development time in the attempt of eliminating them. Efforts were made to characterize the skirts with WLI and SEM by evaluating feature profiles. 3D views of the molds in WLI measurements yielded vertical profiles based on automatic extrapolation in the software. SEM micrographs of the dose and defocus test sample shown in Figure 4.1a-b are given in Figure 4.1d-e, though not necessarily depicting the same structures as in Figure 4.1a-b. The structures in Figure 4.1d-e were exposed at 1000 or 1100 mJ/cm^2 and unknown defocus value. From the SEM micrographs, it can be seen that structures have an undercut rather than a pronounced protrusion at their base. Unfortunately, successful SEM imaging could only be done for this particular sample due to problems with charging of the structures in all other attempts. Nevertheless, based on these micrographs, it was concluded that the profiles were acceptable for microfluidic device fabrication, hence no more efforts were made at eliminating the skirts.

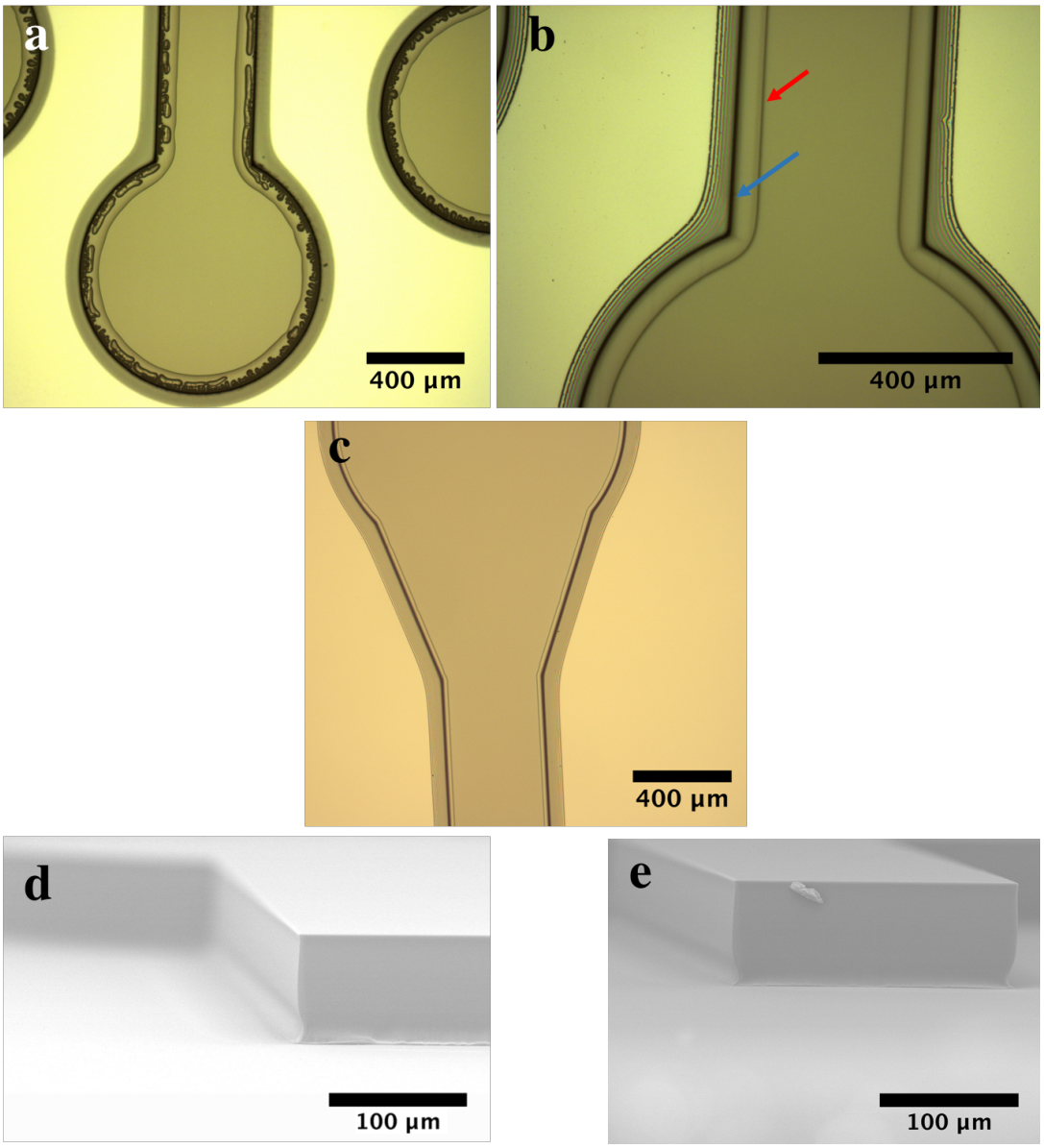

Figure 4.1: Characterization of resulting structures from optimization of photolithography process. **a)** Yellow light micrograph (epi-brightfield) captured at 5x magnification of 73-77 µm thick mr-DWL 40 exposed at 1000 mJ/cm^2 with a defocus value of 7. The same is shown in **b** at 10x magnification, for the same dose, but defocus of 3. Blue arrow denotes structure outline while red arrow indicates unevenness present on the resist surface. **c)** Yellow light micrograph (epi-brightfield) captured at 5x magnification of a 400 µm channel mold feature used for fabrication of microfluidic devices, depicting the area where an inlet/outlet transitions into the microchannel shown at the bottom. **d)** Scanning electron microscopy (SEM) micrograph of the profile of a ∼75 µm tall mr-DWL 40 structure. Micrograph captured at 500x magnification, 15 kV acceleration voltage, 73.3 µA emission current and 11.6 mm working distance. **e)** SEM micrograph of the profile of a ∼75 µm tall mr-DWL 40 structure. Micrograph captured at 500x magnification, 15 kV acceleration voltage, 75 µA emission current and 12 mm working distance. Dust particle is visible in the cross section.

The initial WLI measurements of a mold produced according to the developed protocol during the optimization process indicated height variations of $\sim$1 %, which justified the protocol. However, subsequent measurements throughout the project revealed that silicon molds had varying feature height depending on the time when they were produced, as more recent molds yielded higher and less uniform values. The heights of a selection of molds are given in Table 4.1, showing the (apparent) minimum and maximum values based on the minimum and maximum found in three 3.5 mm $\times$ 2.6 mm measurement areas for each channel. None of the channels used in microfluidic device fabrication had height variations of $>$8 % in a single channel. WLI measurements of the most recent mold are given in Figure 4.2, showing the measurement area of a 200 µm wide channel inlet/outlet in Figure 4.2a. The corresponding measurement window showing the height difference and distance with respect to the cursors seen in Figure 4.2a is given in Figure 4.2b. 3D views of the inlet/outlet of all three channel geometries are depicted in c-e. This mold was not used to produce microfluidic devices.

Table 4.1: Silicon mold feature height measured with white light interferometry as a function of time of fabrication from time equal to zero. More than one mold may have been fabricated at a given time, hence a given height range does not necessarily apply for a single mold.

Time of fabrication	**Feature height**
0	53-56 µm
$>$1 month	59-61 µm
$>$2 months	67-72 µm
$>$3 months	69-82 µm

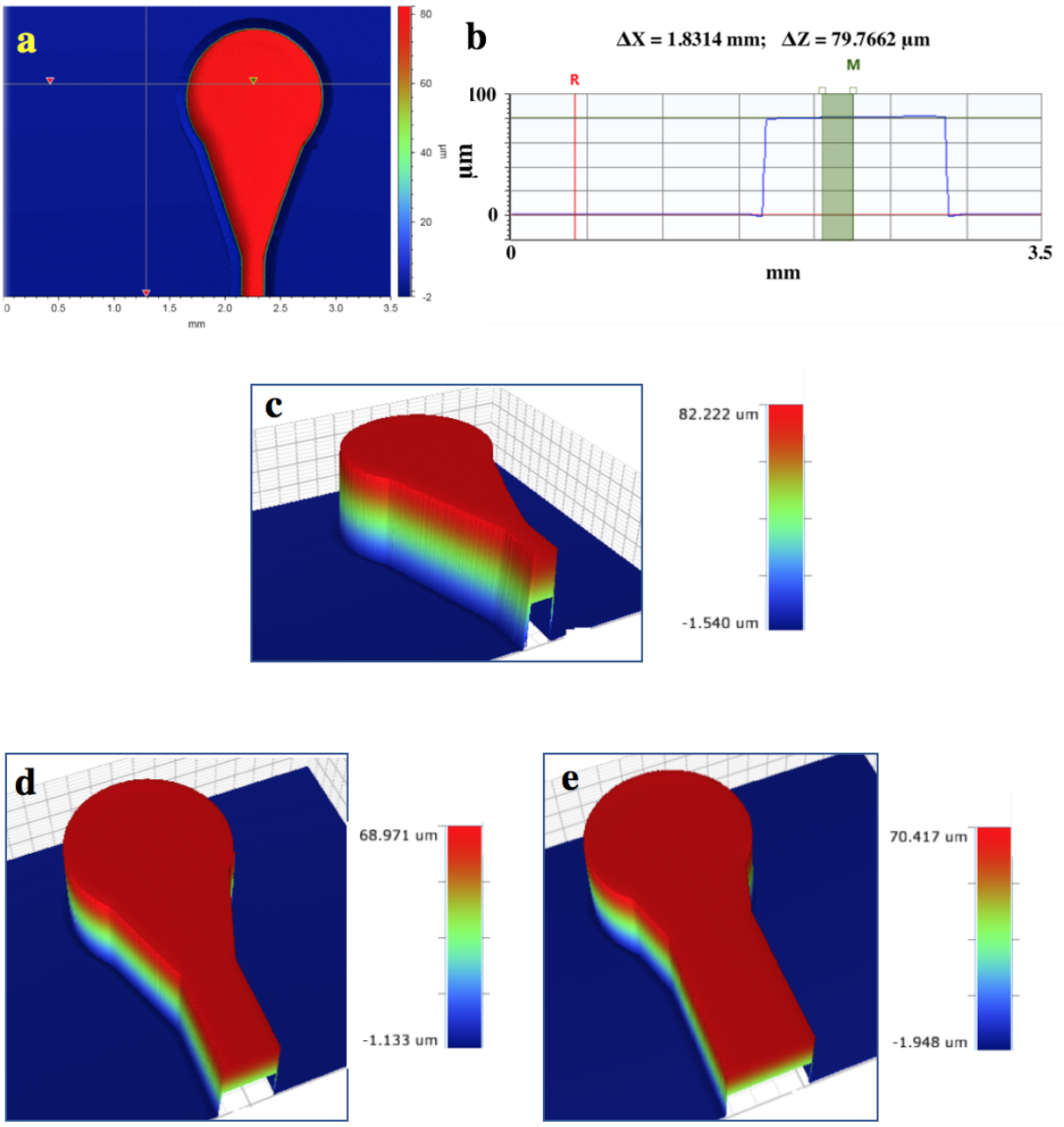

Figure 4.2: Results from white light interferometry characterization of a single silicon mold containing the inverse pattern of 3 microfluidic channels. **a)** The measurement area of a 200 µm wide channel. **b)** Reading of the height difference (ΔZ) and distance (ΔX) between the (upper) red and green cursor in **a**. 3D images of said channel as well as channels of 400 µm and 600 µm width on the same mold are given in **c, d** and **e**, respectively. Data was obtained using the 2.5x objective and 0.55x camera zoom.

4.2 Microbubble behaviour in microfluidic devices

In the following sections, experiments in channels of 400 and 600 µm width proved that both dimensions were equally suitable, with no observable differences.

4.2.1 Insonation of Sonazoid™

Micrographs depicting the insonation of Sonazoid™ MBs diluted with PBS (0.3×10^9 MBs per mL) in a 600 µm wide channel are given in Figure 4.3, representative for n = 4. As evident in Figure 4.3b, all Sonazoid™ MBs disappear rapidly (<1 s) after insonation onset in the 1:3 dilution.

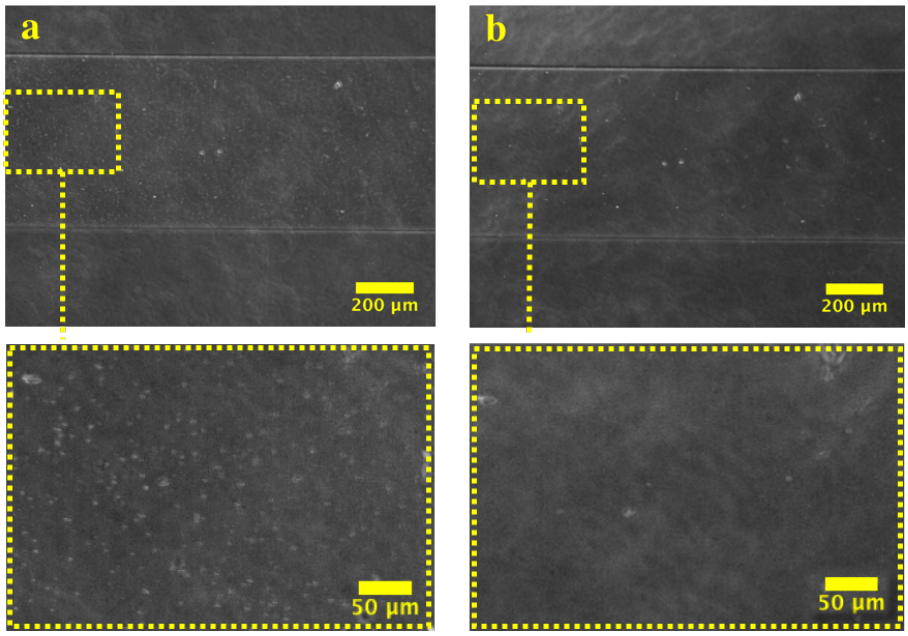

Figure 4.3: Phase contrast micrographs at 10x magnification of insonation of Sonazoid™ diluted with phosphate buffered saline (1:3 dilution) in a 600 µm channel, showing the situation after injection and before insonation in **a** and <1 s after insonation onset in **b**. The bright spots visible in **b** are due to dust particles and/or debris from the channel material.

For higher MB concentrations as in the undiluted case (1.2×10^9 MBs per mL), MB aggregation was observed both before as well as during insonation as seen in Figure 4.4 for a 600 µm wide channel. Aggregation progressed throughout insonation, forming fewer and larger aggregates, and it is likely that the smallest aggregates disappeared as in the diluted case. Notably,

the morphology of the aggregates does not resemble gas bubbles, hence the term aggregation is used over coalescence. The aggregation was observed in all experiments (n = 4). For the Sonazoid^{TM} in Figure 4.4, aggregation continued until stable aggregates were reached as seen in Figure 4.4d. These two aggregates remained stationary throughout the rest of the insonation period as well as immediately after, but their lifetime was not studied. The presence of aggregates that remained stable throughout the whole insonation was observed in 2/4 cases.

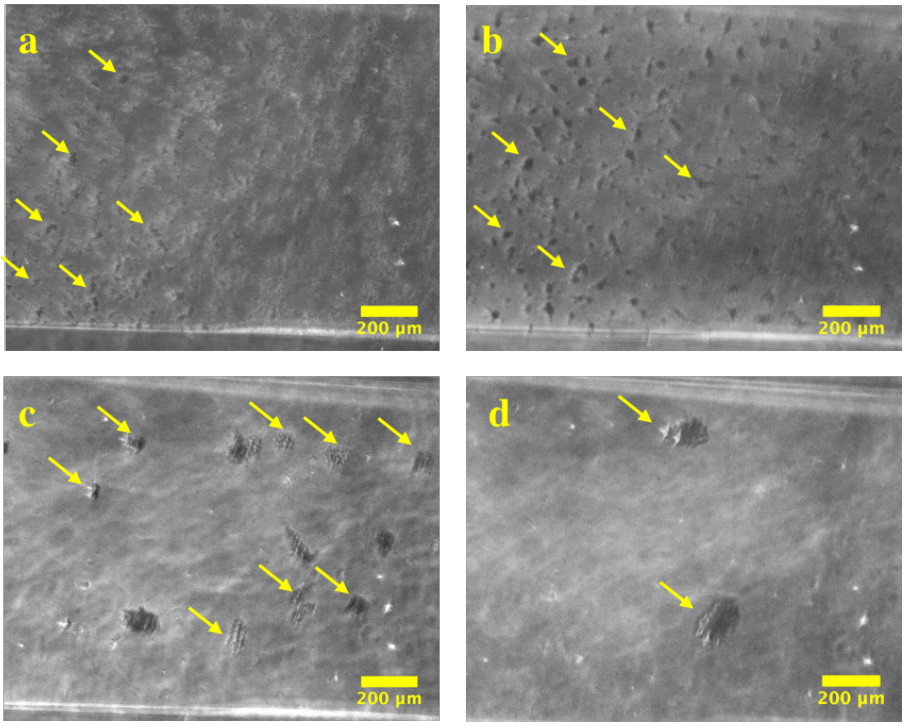

Figure 4.4: Phase contrast micrographs at 20x magnification of insonation of undiluted Sonazoid^{TM} solution in a 600 µm channel, showing the situation after injection (**a**), <0.5 s after onset of insonation (**b**), 4 s after onset (**c**) and 18 s after onset (**d**). Arrows indicate aggregates.

4.2.2 ACT bubble behaviour and size during activation

Micrographs of ACT bubbles in a 400 µm wide channel during activation are shown in Figure 4.5, depicting the situation 1, 10, 30, 40 and 45 s after onset of activation. Visible coalescence between ACT bubbles was generally low (<8 % of the bubbles), but did happen as shown in Figure 4.5g-h. Bubble movement and collapse were not observed, and cavitation was as expected not observable due to the low frame rate. White spots that are not ACT bubbles are visible in Figure 4.5g-h.

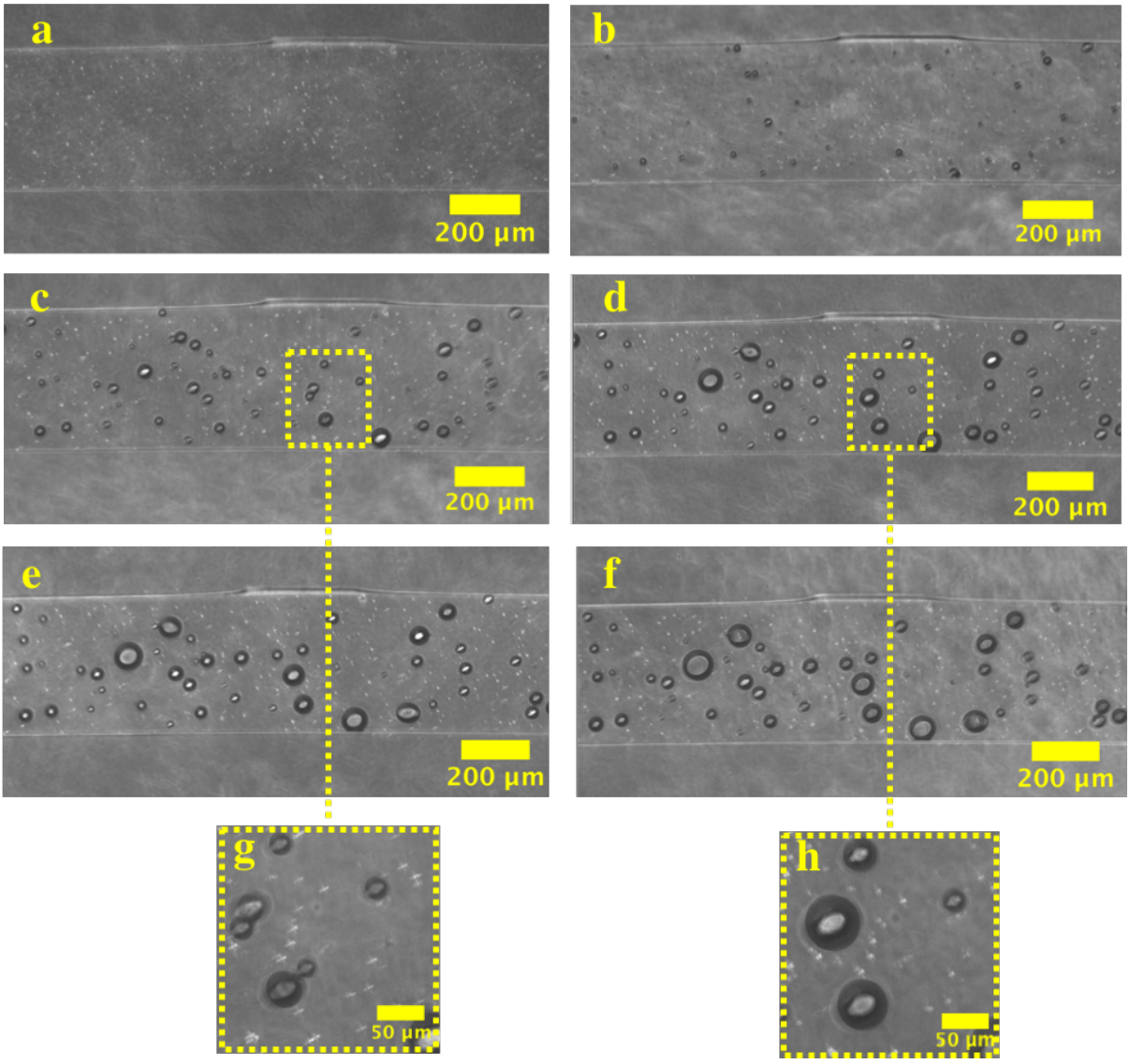

Figure 4.5: Phase contrast micrographs at 10x magnification showing the activation of Acoustic Cluster Therapy (ACT) clusters to generate ACT bubbles inside a 400 µm channel. **a)** The situation after injection, before onset of insonation. **b)** 1 s after onset. **c)** 10 s after onset. **d)** 30 s after onset. **e)** 40 s after onset. **f)** After insonation stopped, i.e. after 45 s from onset. **g-h)** Coalescence of ACT bubbles taking place during the first 30 s of insonation. Note that **g** shows an earlier time point than **c** in order to better visualize the coalescence, the same bubbles are depicted. Blurred features visible on the outside of the channels are due to gas bubbles trapped between the plastic foil and device surface, and/or dust particles.

The size distribution of ACT bubbles at the given time points is given in Figure 4.6. The analysis attempted to ignore the few (<8 %) bubbles that had visibly coalesced with other bubbles due to perceived lack of in vivo relevance (see Chapter 5.2.1), resulting in artificially large ACT bubbles. In Figure 4.6a, the distribution is given with respect to all remaining bubbles, while in Figure 4.6b, outliers have been removed. An outlier was defined as any

bubble above 50 µm in diameter after 10 s of activation (<1 %), above 55 µm after 30 s (6 %) and above 60 µm after 40 and 45 s (6 and 9 %, respectively). These thresholds were chosen to remove a few individual ACT bubbles that were unexpectedly large (compared to mean diameter) at a given time point. ACT bubbles with diameters above the channel height can be assumed to be in contact with both the bottom and ceiling of the channel, and are thus most likely immobilized. The analysis does not take into account that additional ACT clusters may be activated into ACT bubbles throughout the initial 15 s of insonation, or complete dissolution of ACT bubbles (observed for 2-4 bubbles in the 10 µm size range). As these bubbles were not ignored or discriminated, the total number of bubbles varies across the different time points (81-102). Analysis was based on data from n = 4 individual experiments.

The mean diameter at the given time points, both including and excluding the outliers, is depicted in Figure 4.6c. Maximum deviation from the respective median diameter is 4 %. The evolution of the size distributions with insonation time show that the fraction of large bubbles, especially bubbles >50 µm, as well as small bubbles <20 µm, both increase during the last 15 s of insonation. This indicates that larger bubbles grow at the expense of smaller bubbles (Ostwald ripening). It was observed that this trend continued after activation stopped with some of the smallest ACT bubbles dissolving completely or coalescing with other bubbles, which can also be seen in Figure 4.6a for the size distribution. Moreover, the growth of large ACT bubbles after insonation can also be seen qualitatively by comparing Figure 4.5f and Figure 4.7a, which shows the same channel between activation stopped and enhancement started. As evident from Figure 4.6c, the mean bubble diameter appears to grow rapidly during the first 10 s of insonation with a rate of >12 µm per 10 s, before it starts to stabilize after 30 s. At this time, about two thirds of the ACT bubbles have a diameter below 40 µm. However, between activation stopped and enhancement started, the mean diameter continued to grow, reaching 44.9 ± 22.1 µm when not correcting for outliers (based on a total of 58 ACT bubbles, n = 3 due to loss of data in one experiment), and 41.5 ± 18.7 µm when removing outliers above 80 µm (7 %). Size distribution of the former group (including outliers) is given in Figure 4.6a as "∼100 s". The size distribution when correcting for outliers is not shown as the outlier threshold is significantly higher than the 50 µm threshold of the largest ACT bubbles' group.

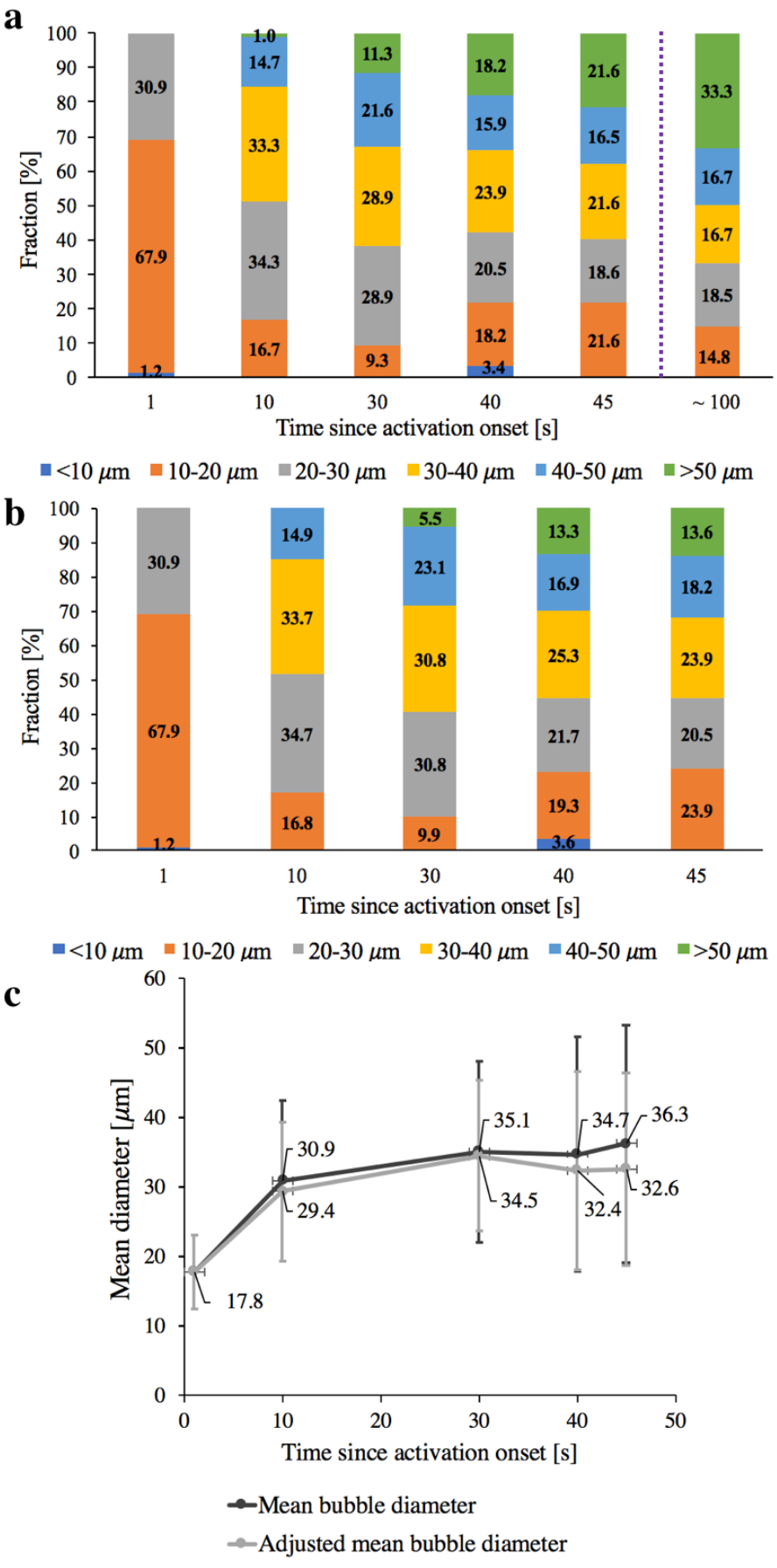

Figure 4.6: See next page for caption.

Figure 4.6: Size distribution and mean diameter of Acoustic Cluster Therapy (ACT) bubbles observed in 400 and 600 µm wide channels, as function of time from onset of insonation, n = 4 (n = 3 for the last group in **a**). **a)** Size distribution of ACT bubbles excluding <8 % of the bubbles that had visibly coalesced. The dashed line denotes that insonation was stopped after ∼45 s. **b)** An adjusted size distribution ignoring ACT bubbles of size >50 µm after 10 s, >55 µm after 30 s and >60 µm after 40 and 45 s. **c)** Evolution of mean diameter during insonation, the adjusted mean diameter according to **b**.

4.2.3 Behaviour of ACT bubbles during low frequency enhancement step

During the 2 min enhancement step at 500 kHz, coalescence and/or Ostwald ripening, and changes in ACT bubble size could be observed as depicted in Figure 4.7, which shows the same channel and ACT bubbles as Figure 4.5. Again, no collapse or bubble movement were observed. By comparing the exact same ACT bubbles before and after enhancement (a total of 47 ACT bubbles, n = 3), i.e. neglecting coalescing MBs, changes in size could be studied as shown in the size distributions in Figure 4.7e. Ostwald ripening was visible as large bubbles (>70 µm) grew considerably, while smaller bubbles (<40 µm) shrinked or dissolved. In fact, in all cases (n = 3), the three largest bubbles increased in size during enhancement. Furthermore, in all cases, the total number of ACT bubbles decreased (−18 %) during enhancement due to observed coalescence or dissolution. However, coalescence, growth and dissolving ACT bubbles were also seen in experiments where ACT bubbles were left for observation after activation without the enhancement step (n = 3). The same could be observed even 5 min after the enhancement step (n = 3), as can be seen by comparison of Figure 4.7c and d. Hence, it is unlikely that these phenomena were due to the enhancement step itself.

5 min after enhancement had stopped, bubbles of 100-200 µm diameter were visible. In one case (Figure 4.7c), ACT bubbles below 25 µm could still be observed, comprising 17 % of the bubbles. However in the other two cases, the smallest diameter 5 min after insonation was ∼50 µm. By comparing Figure 4.7c-d, one can see that especially the large ACT bubbles are retained after insonation.

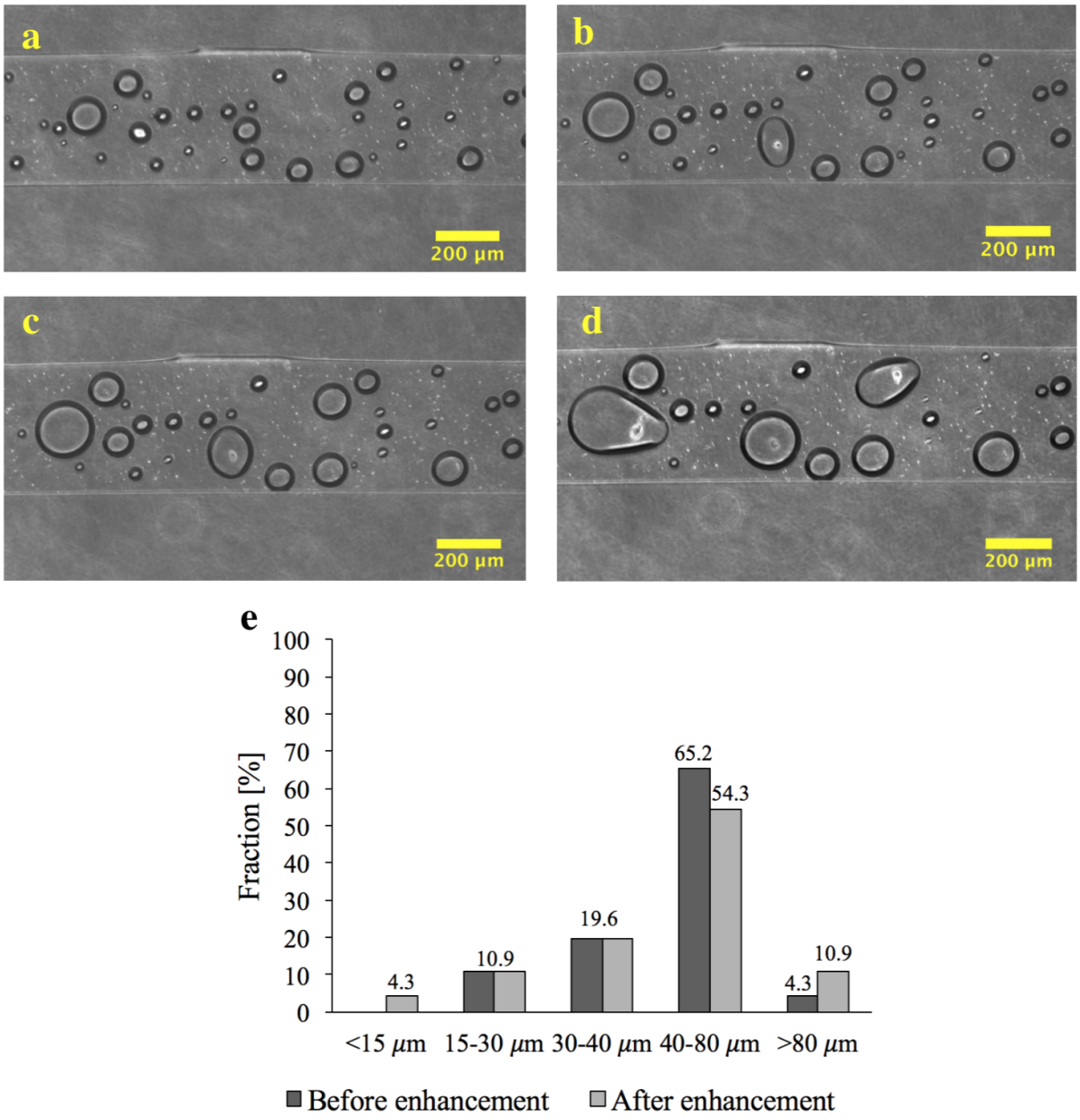

Figure 4.7: a-d) Phase contrast micrographs at 10x magnification showing the 500 KHz enhancement of Acoustic Cluster Therapy (ACT) bubbles in a 400 µm wide channel, which lasted for 2 min. **a)** The situation before enhancement, i.e. after activation. **b)** The situation after 30 s from onset of insonation. Bubble coalescence is visible. **c)** The situation a short time after insonation has stopped. **d)** 5 min after insonation has stopped with visible coalescence. Blurred features visible on the outside of the channels are due to gas bubbles trapped between the plastic foil and device surface, and/or dust particles. **e)** Size distribution of ACT bubbles before and after enhancement, n = 3.

4.3 Microfluidic cell culture

For practical reasons throughout the project, optimization of cell seeding resulting in acceptable cell layers of HUVECs and PC3 cells was only achieved for either of the devices. HUVEC culture was carried out in G-devices and PC3 in M-devices. Evaluation of the cell layer could only be done for the bottom surface of the channels with the microscopy tools in this project, however, cells were expected to attach to the additional surfaces. Presence of cells attached to the ceiling could be confirmed by adjusting the focus.

4.3.1 Confluent monolayers of HUVEC in G-devices

Figure 4.8 shows micrographs of HUVECs in G-devices up to 6 days after seeding. As evident, the cells can be observed to attach to the channel bottom surface after just 2 h post seeding, yielding a confluent cell layer in the 600 µm wide channel shown in Figure 4.8a where cell morphology resembles the typical ”cobblestone”. This morphology is a typical sign of differentiated HUVECs and a confluent endothelial monolayer [127], resembling endothelial linings in vivo [145]. Cell layers of high confluence and healthy morphology could also be observed in 400 µm wide channels, but as can be seen in Figure 4.8b, cell densities were quite low in the case of 200 µm channels. Liquid injection into 200 µm channels was also observed to be more difficult, hence channels of this dimension were deemed unsuitable for subsequent experiments with insonation. Staining with calcein in another 600 µm wide channel shows viable cells 1 day after seeding, as shown in Figure 4.8c where cells can be observed to also attach to the channel side walls. Moreover, 6 days after seeding, viable cells could still be observed in phase contrast microscopy (Figure 4.8d), although viability was not confirmed by fluorescence staining. These HUVECs have a more elongated morphology and appear larger than in Figure 4.8b due to a lower cell density, i.e. more space per cell.

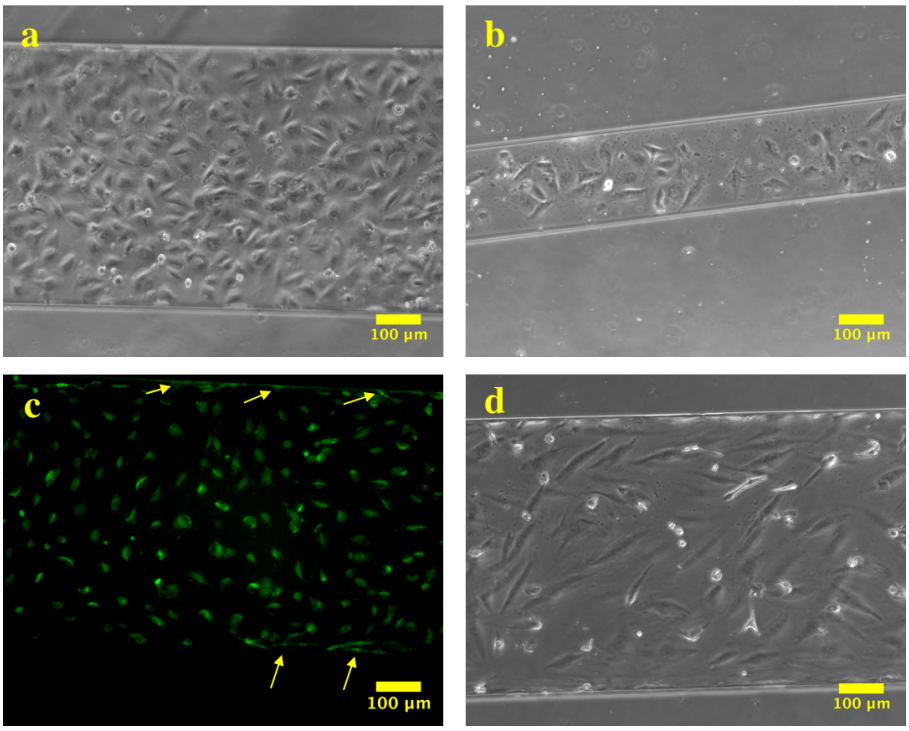

Figure 4.8: Phase contrast and fluorescence micrographs at 10x magnification of Human Umbilical Vein Endothelial Cells (HUVECs) cultured in microfluidic devices with glass bottoms (G-devices) with cells on channel bottom in focus. **a)** 2 h post seeding in a 600 µm wide channel. **b)** 2 h post seeding in a 200 µm wide channel. Features visible on the outside of the channel are dust particles. **c)** Fluorescence micrograph of a 600 µm channel after staining with viability marker calcein, 1 day post seeding. Yellow arrows indicate viable HUVECs attached to the channel side walls. **d)** 6 days post seeding in a 600 µm, cell morphology indicating viable cells.

4.3.2 Relatively confluent monolayers of PC3 in M-devices

Seeding PC3 cells in channels of 400 and 600 µm width at 20 million cells per mL, after coating with 10 µg/mL fibronectin, was deemed most optimal, as shown in Figure 4.9. PC3 cells were observed to attach to the channel surface after incubating devices overnight, but to much lower degree in 200 µm channels, in consistency with the results of HUVECs in G-devices. The longer waiting time before cell attachment compared to HUVEC was consistent with observations of when PC3 cells attached in T75 flasks. As visible in Figure 4.9a, areas of confluent cell layers on the channel bottom could be observed especially near the channel inlet/outlet, but the cell density was in general lower in the channel itself, as seen in Figure 4.9b. As with HUVEC, the more elongated morphology in Figure 4.9b is directly attributed to the lower cell densities. Nevertheless, cell layers such as the one seen in Figure 4.9b were considered adequate for subsequent experiments with insonation. Note that the channel shown in Figure 4.9 has not

been flushed with any liquids, including MBs, post seeding.

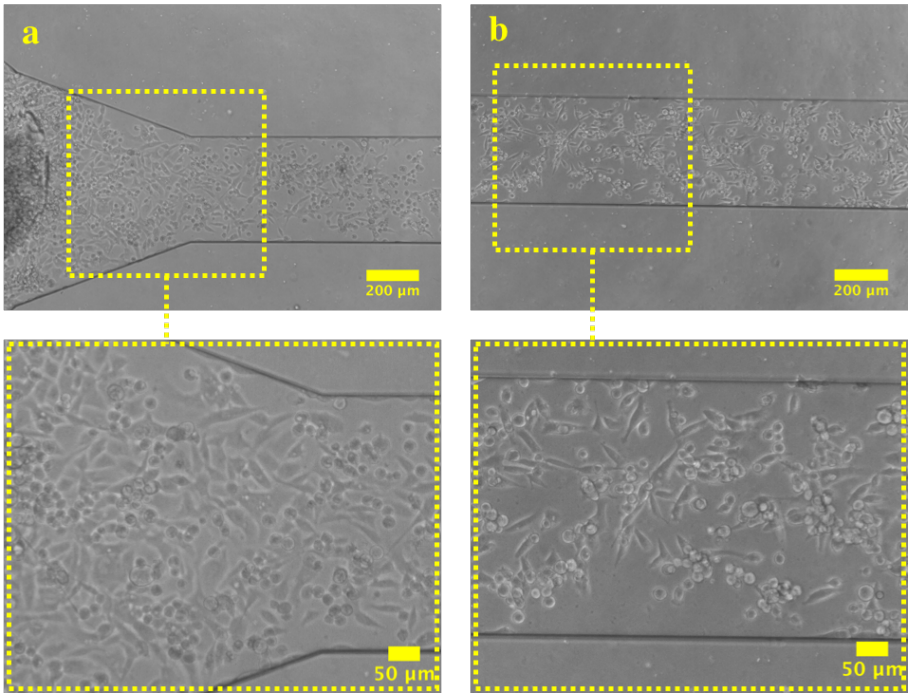

Figure 4.9: Phase contrast micrographs at 10x magnification of PC3 cells seeded in a 400 µm wide channel with Mylar® sheet bottom (M-device) after incubation overnight, cells on channel bottom in focus. **a)** Area around inlet/outlet where cell density is high. **b)** Main channel area of same channel in **a**, showing lower cell concentration and elongated morphology.

For cells seeded at a lower concentration (∼10 million per mL), low density of attached cells was observed the day after seeding, as shown in Figure 4.10. Moreover, significant amounts of the PC3 cells had rounded morphologies suggesting non- or poorly attached cells. While the fibronectin concentration for coating in Figure 4.10a was 5 µg/mL, it was 10 µg/mL in Figure 4.10b. Note that the channel in Figure 4.10a has been flushed with growth medium, hence fewer cells are visible than in Figure 4.10b.

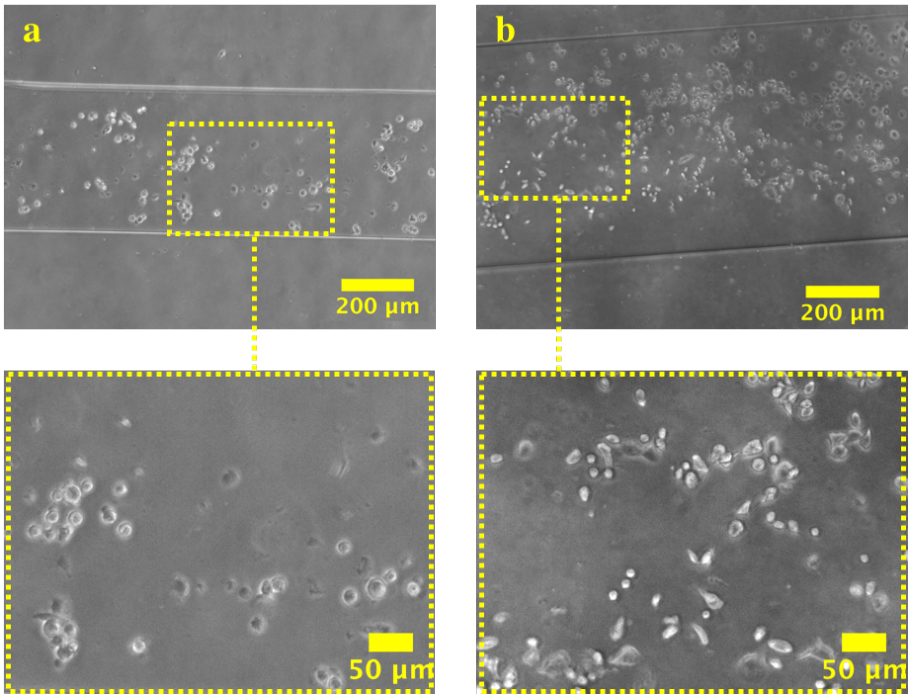

Figure 4.10: Phase contrast micrographs at 10x magnification of PC3 cells day after seeding under unoptimal conditions. The cell concentration is ∼10 million per mL in both cases. **a)** 400 µm wide channel. **b)** 600 µm wide channel, cells seeded at higher fibronectin concentration than in **a**.

4.4 Sonoporation of PC3 cells in microfluidic devices

4.4.1 Sonoporation by Sonazoid™

Enhanced PI uptake by PC3 cells in M-devices following insonation of Sonazoid™ was not substantial and could not be observed in every experiment (n = 5). In Figure 4.11a, the exact same cells giving off the fluorescence signal were observed both before and after insonation was carried out, i.e. insonation did not result in any additional cells taking up PI. On the other hand, Figure 4.11b shows a different experiment where visible uptake of PI during insonation can be observed for a single cell, i.e. sonoporation. Individual cells (roughly 1-3 % of the cells within the field of view) becoming sonoporated were observed in two experiments. Changes in fluorescence intensity were inconclusive due to the low signal-to-noise ratio. Increase of fluorescence intensity during the 2-minute waiting time after insonation was deemed to be negligible although the change in intensity could not be measured accurately.

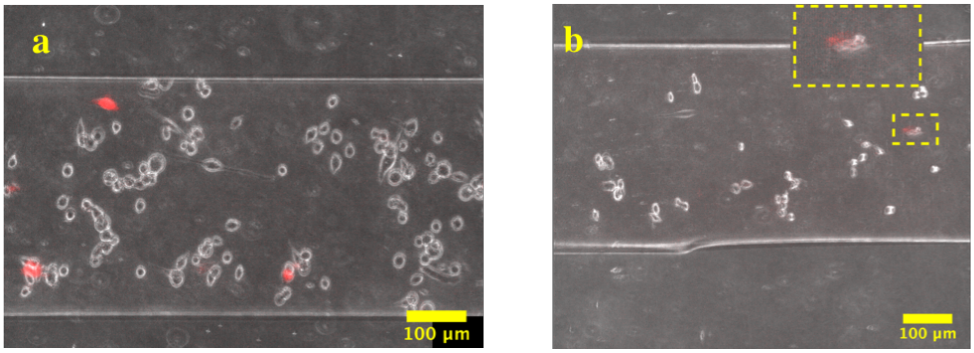

Figure 4.11: Overlay of phase contrast and fluorescence micrographs at 10x magnification from two distinct experiments with different outcome. No sonoporation by Sonazoid^{TM} occurred in **a** as the same fluorescence spots were visible both before and after insonation, but sonoporation by Sonazoid^{TM} of a single cell can be seen in **b**.

Notably, the cell concentrations seen in Figure 4.11 are relatively low compared to Figure 4.9 before injecting MBs, and very few of the cells have the typical spread morphology of attached PC3 cells seen in Figure 4.9. Cell layers appearing different after injection of MBs were observed with ACT bubbles as well, and are attributed to the fact that high concentrations of unattached cells located especially in the inlet and outlet areas were flushed into the channel upon injection. Removal of unattached cells prior to adding MBs was attempted by injecting medium, but required further optimization and was thus not carried out in most cases. To some degree, cell detachment was observed as a consequence of liquid injection for both MBs.

4.4.2 Sonoporation by ACT bubbles

Sonoporation during activation of ACT clusters was observed as new fluorescence signals in the proximity to ACT bubbles appeared following insonation. Figure 4.12 shows phase contrast and fluorescence micrograph overlays as well as separate fluorescence micrographs before insonation, after activation, as well as after enhancement. As seen in Figure 4.12b and g, new fluorescence spots related to activated ACT bubbles were visible only after activation and not before (Figure 4.12a and f). In Figure 4.12b, the ACT bubble is $\sim$33 µm, while in Figure 4.12c after enhancement, it is $\sim$25 µm, indicating a plausible shrinkage. It was not possible to deduce from phase contrast micrographs if an ACT bubble was positioned above or below a cell due to excess light scattering by the bubble. Despite this, in all regions where the fluorescence signal overlaps with an ACT bubble, the bubble is most likely sit-

uated below the cell due to cells being attached to the channel ”ceiling” in the insonation set-up.

Before ACT clusters were activated, there was considerable fluorescence from already non-viable PC3 cells, and tracking of individual cells could not be done accurately. In fact, in several cases, ACT bubbles appeared in areas with substantial background fluorescence. Hence, sonoporation of individual cells caused by individual ACT bubbles could only be observed for one or a few single ACT bubbles in three individual experiments. The total fluorescence intensity before and after activation was not evaluated as the interaction between ACT bubbles and already non-viable cells was considered uninteresting.

During enhancement, the fluorescence intensity increased for all channels that were studied (n = 4). The increase can also be seen qualitatively by comparing Figure 4.12b to c. The mismatch between Figure 4.12b-c may be due to a different focus showing unresolved spot(s) in Figure 4.12c, however the spot(s) remained unresolved even when adjusting the focus. In contrast to experiments with ACT bubbles in empty channels, movement by ACT bubbles in channels with PC3 cells due to the low frequency insonation was clearly visible, resulting in bubbles making physical contact as evident in Figure 4.12e and Figure 4.13. No ACT bubbles with diameters above the channel height moved during enhancement. Increase of fluorescence in the semi-quantitative analysis, correcting for possible changes in the background, was 8.1 ± 2.8 % after 1 min of enhancement and 14.7 % (minimum 8.1 %, maximum 18.3 %) after 2 min of enhancement (Figure 4.12i). There was no indication that fluorescence intensity increased or decreased for channels that were used multiple times.

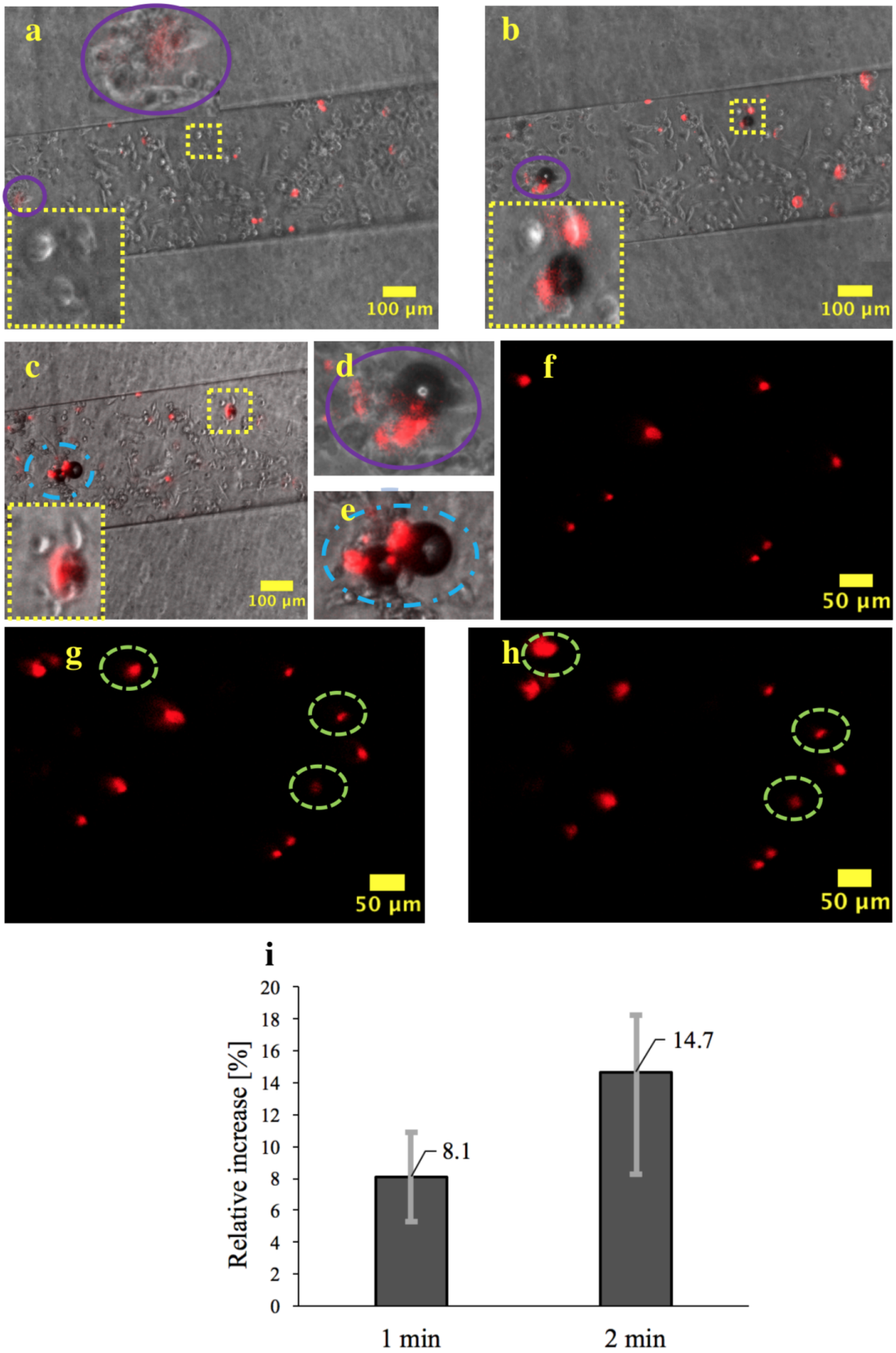

Figure 4.12: a-h) Phase contrast and fluorescence micrograph overlays at 10x magnification depicting sonoporation during activation and enhancement of Acoustic Cluster Therapy (ACT) bubbles. See next page for detailed captions.

Figure 4.12: **a)** Situation after co-injecting ACT clusters and propidium iodide (PI), before activation in a 400 µm channel. Non-viable cells are already present. **b)** Situation after activation, showing cells in the inserts of **a** getting sonoporated by two ACT bubbles of 33 and 57 µm. Magnification of the 57 µm-bubble is shown in **d**. **c)** Situation after 2 min enhancement, where ACT bubbles have translated, as magnified in **e**. The 57 µm bubble from **d** is in contact with a 48 µm bubble that was initially outside of the field of view, 120 µm away. **f)** Fluorescence micrograph of a 600 µm channel, before activation. **g)** Fluorescence micrograph of the situation in **f** after activation of ACT bubbles, new PI spots are indicated by green circles. Only one of these spots is in close proximity to or overlaps with an ACT bubble. **h)** Fluorescence micrograph after 2 min of enhancement, showing no new spots from **g**, however, the intensity has changed and the cells have been displaced. **i)** Semi-quantitative evaluation of the change in fluorescence intensity after 1 and 2 min of low frequency enhancement of ACT bubbles, compared to the situation before onset of the enhancement step. Error bars indicate maximum and minimum.

It is likely that significant amounts of PC3 cells in the field of view were in suspension rather than attached to the channel surface, as in the case of Figure 4.13 where cell displacement due to moving ACT bubbles was observed as insonation started. Displacement was mostly observed to be due to cells being pushed or dragged by ACT bubbles.

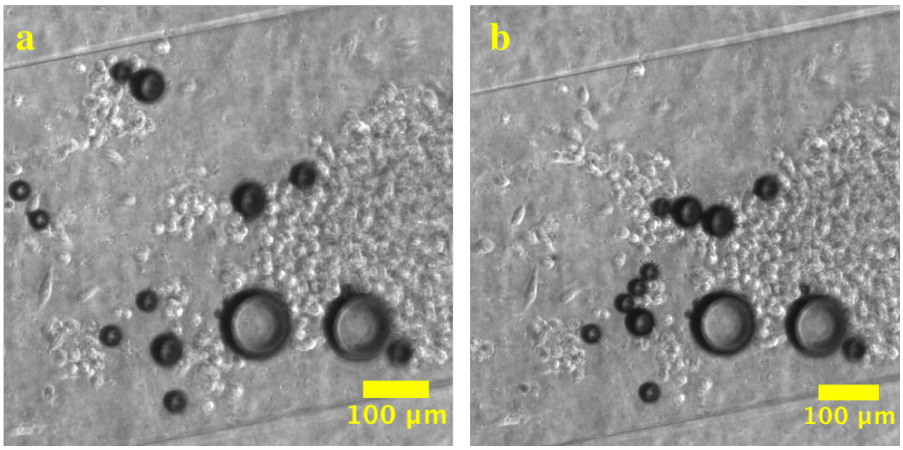

Figure 4.13: Micrographs at 10x magnification showing Acoustic Cluster Therapy (ACT) bubbles in a 600 µm microchannel with PC3 cells, the situation before enhancement step started in **a** and the situation at the onset of insonation in **b**. The particular channel was not used to evaluate fluorescence intensity as the bubble movement caused vigorous movement of cells (as visible by comparing **a** and **b**) and contained strong background fluorescence.)

Chapter 5

Discussion

5.1 Microfluidic device fabrication and cell culture

The results from the microfluidic cell cultures showed that the protocols developed through this project were successful in producing microfluidic devices that supported cell culture of both HUVEC and PC3 cells, in addition to fulfilling the requirements of optical and acoustic transparency. Liquids could be easily injected into the microchannels using a micropipette with hardly any air bubbles getting trapped inside the channels, which was a problem discussed in the pre-master project [1]. Undoubtedly, the positive results are due to the new microfluidic channel design (with respect to the previously reported one [1]) with especially the lack of branches and increased channel height. Both G- and M-devices appear suitable for cell culture. The latter was deemed necessary for compatibility with the present insonation set-up to eliminate US reflection by glass, and ensure proximity between PC3 cells and floating MBs. Unfortunately, ”endothelialized” microchannels were only achieved in G-devices as there was not enough time or materials to carry out HUVEC culture in M-devices during the course of the project. Culture of HUVEC in M-devices is however considered highly feasible based on the results in this thesis along with evaluation of HUVEC viability on fibronectin coated PDMS surfaces from the pre-master project [1].

5.1.1 Silicon mold fabrication

In this project, a protocol to fabricate silicon molds with acceptable structures of $\sim$60-70 µm height was developed based on optimization of the various photolithography steps. The imperfections presented in Chapter 4.1 are considered negligible (e.g. height variations of $<$8 % in a single channel) for microfluidic devices in their present application. The observed batch-to-batch variation in mold feature height, with an overall trend of increasing resist thickness with time, can be explained by likely varying photoresist properties. All the resist that was used for mold fabrication was stored in a single bottle, i.e. the amount of resist present in the bottle was decreasing after each use. Hence, the significance of solvent evaporation would increase each time the bottle was opened. Consequently, it is believed that the resist viscosity increased with time. This would explain its changing (flow) behaviour, resulting in a less homogeneous coating as well as an increased thickness. The changing behaviour of the resist may be characterized to develop a more robust protocol in the future if a specific mold feature height is desired. On the other hand, the channel profile could not be accurately characterized but was presumed to not be entirely vertical as already drawn forward in Chapter 4.1. The undercuts visible in the SEM micrographs (Figure 4.1d-e) suggest that the observed 'skirts' in optical microscopy, i.e. protruding resist at the base of the structures, were in fact image artifacts. As the imperfection appeared the same for all samples inspected with optical microscopy, and as WLI produced the same 3D profiles, the profiles observed in the presented SEM micrographs were deemed somewhat representative. However, reproducibility of the profiles could not be verified. The imperfection is most likely due to an uneven exposure dose across the thickness of the resist during UV radiation, and this irregularity should be reproducible if the dose and defocus values are both kept constant. Possibly, these undesirabilities, especially the inhomogeneous height within a single channel, could have implications on liquid flow behaviour and distribution of cells during seeding. However, as already stated, the imperfections could not be associated with anything of concern in this work.

5.1.2 PC3 vs HUVEC: implications of using a cancer cell line

At the proof-of-concept stage, successful application of microfluidic devices seeded with PC3 cells in sonoporation experiments is considered highly translatable to the case of endothelial cells as the interactions with MBs are by far mostly mechanical. Being a different cell type, the relevance of using a cancer cell line such as PC3 in a vascular model is naturally questionable. Undoubtedly, the in vivo relevance is weakened as the cellular responses to external factors will be different from endothelial cells. The viability of the different cell lines in microfluidic devices is another topic worth discussing. By nature, the cancer cell line has faster proliferation rate than HUVEC and is likely more robust with regards to detrimental culture conditions. One may be tempted to presume that PC3 would have a higher viability than HUVEC during microfluidic culture. However, none of the results support this hypothesis; HUVECs were observed to attach substantially to channel surfaces after a much shorter time compared to PC3 cells, with the ability to yield higher confluence at a lower cell concentration during seeding compared to PC3, and with unattached and/or non-viable cells easily removable. Moreover, HUVECs had an indicative viability in G-devices up to 6 days post seeding where medium renewal in devices was carried out by gravity driven flow. Nevertheless, long-time cell viability in microfluidic channels is irrelevant if the vascular model is to be used in experiments with insonation and MBs a short time after seeding.

Although PC3 cell layers appeared acceptable following incubation overnight after seeding, significant numbers of unattached or non-viable cells were present in suspension after MB injection. This is highly problematic due to interference with video quality and quantification of fluorescence. Moreover, for a vascular model, it is desired to study MBs' effect on a layer of adhered cells rather than cells in suspension. In the case of HUVEC, however, most unattached cells were easily flushed out of the device without disturbing the cell layer, in contrast to PC3 cells, suggesting HUVECs are more firmly attached to the bottom surface in M-devices. For PC3 cells, collagen I has been reported to be a more suitable protein to promote strong adhesion and spread morphology [146]. The lower cell concentration upon seeding of HUVEC compared to PC3 is also likely an important factor. In other words, the problems experienced with PC3 cells will not necessarily be an issue in future endothelial cell cultures in M-devices. Neverthe-

less, liquid injection that neither produces air bubbles within the channels nor disturbs the cell layer must be ensured.

5.1.3 Microfluidic design and cell seeding method

Comparison of the established microfluidic designs and cell seeding method with respect to similar reports from literature is of interest to evaluate their future potential. As justified earlier in Chapter 3.3, a microfluidic design comprising a single, straight channel was desired in this project to aid cell seeding, and dimensions were chosen to facilitate liquid injection. In the future, down-scaling of the channels may be desirable in order to mimic small diameter vessels in vivo (as was the goal in the pre-master specialization project [1]) and simulate capillary occlusion by ACT bubbles in the 20-30 µm range. Single microchannels for endothelial cell culture have been reported before as presented in Chapter 2.4.3, however, these channels have quite different cross section dimensions than the channels in this project. In the device by Esch et al., HUVECs seeded at $5 \times 10^5\,\mathrm{cm}^{-2}$ were visibly packed closely together in channels of just 50 µm × 50 µm cross section [98], i.e. dimensions closer to (large) capillaries in vivo, and cells attached to the whole channel surface. The authors used a syringe pump operating at constant flow rate to ”draw” the cells into the device, after seeding into the inlet with a micropipette.

Although a vast number of reports on cell culture in rectangular PDMS channels exist, the literature on (endothelial) cell culture in microchannels of similar or smaller dimensions is scarce, as indicated in Chapter 2.4.3 with half of the devices presented in Figure 2.2 having widths of millimeter scale. From the experiences in this project, establishing monolayers of both PC3 cells and HUVECs of acceptable density is difficult in the smallest 200 µm wide channels, which is still four times wider than the channels by Esch et al. A sufficient density upon seeding is crucial not only for subsequent insonation experiments, but also also for physiological exchange of chemical cues such as growth factors between cells necessary for cell growth and viability. Perhaps the use of a syringe pump is in fact essential for administering both cells and growth medium in microfluidic channels of smaller dimensions [97, 99], although operating such a pump for this purpose can be difficult according to experiences from

the pre-master specialization project. Cell loading by other measures, such as by gravity driven flow, have also been conducted in channels of $100\,\mu m \times 100\,\mu m$ cross section [84]. Hence, any future re-design of the microfluidic device involving down-scaled dimensions may require investigation and optimization of new liquid handling methods.

While the endothelium covers the whole 3D internal surface of blood vessels in vivo, the presence of acceptable HUVEC and PC3 layers could only be confirmed on the channel bottom surface with the microscope tools used in this project. In the case of a planar cell monolayer, not only is the in vivo relevance compromised, but the probability of MBs located in the proximity of cells is reduced. To solve the latter issue, Mylar® sheets were employed as channel bottoms to be able to get a situation were floating MBs could make contact with a cell layer present above the MBs. It is unlikely that sonoporation would be detectable for cells located below MBs unless for ACT bubbles extending the whole height of the channel, as MB sedimentation is unlikely. In the future, efforts could be made to achieve and characterize '3D' cell monolayers for a more physiologically relevant model. HUVEC monolayers on the whole surface of a rectangular channel was achieved in the devices by Zheng et al. [87] and Esch et al. [98]. Presumably, although not mentioned by the authors, the 3D attachment can be facilitated by flipping the device while cells are still in suspension, or loading cells in several steps before flipping, but this will require further investigation and optimization. It is also possible that the cell concentration and type or concentration of ECM proteins play additional roles. On a further note, other approaches to engineering 3D in vitro microvessels exist, including cell seeding in semi-circular [98] or circular microchannels [147], or inducing endothelial sprouting in ECM by adding vasculogenic factors [87] or co-culture with stromal cells that release pro-angiogenic factors [87, 90]. Such sophisticated 3D models would indeed provide higher in vivo relevance than our current set-up, with the potential of visualizing actual drug release and tissue penetration following MBs delivered at physiological flow rates [115]. These approaches will however require new materials and methods, including other microscopy tools such as confocal microscopy to visualize 3D cell culture.

5.2 Studying microbubble behaviour in microfluidic devices

As with the devices prepared during the pre-master specialization project, the M-devices that were produced during this master project allowed real-time visualization of ACT bubbles in vitro. Importantly, M-devices have a different substrate than the devices fabricated during the pre-master specialization project, and a different ACT cluster concentration before insonation due to dilution with PBS. A significantly higher data amount has been obtained to determine size of ACT bubbles. Furthermore, the behaviour of Sonazoid^{TM} during 2.5 MHz insonation was studied, as well as ACT bubble behaviour during low frequency enhancement, two processes which were not studied previously.

The effect of channel reuse on MB behaviour experiments is presumed negligible due to thorough washing between subsequent experiments that would remove remaining MBs and ACT clusters.

5.2.1 Comparison of Sonazoid^{TM} and ACT bubbles during 2.5 MHz insonation

The behaviour of ACT bubbles and Sonazoid^{TM} in an acoustic field is very different as the results in Chapter 4.2 show. Whether the disappearance of Sonazoid^{TM} in the diluted case was due to collapse or dissolution could not be determined from videomicroscopy. However, the bubble disappearance can be related to the fact that Sonazoid^{TM} has been reported to collapse at MI > 0.4 [148], as could potentially be the case depending on how the transducer was placed relative to the device surface, resulting in a different acoustic field than when the transducer was characterized. Collapse is however not necessarily due to inertial cavitation as the process is unlikely for Sonazoid^{TM} with MI < 1 [149]. Nevertheless, collapse could not be verified, and will be discussed further in Chapter 5.3.1. It is also possible that MBs were instead pushed outside of the field of view due to acoustic radiation forces [43].

At higher MB concentration as in the undiluted case, Sonazoid™ was observed to form aggregates. The concentration dependency can be understood as neighbouring MBs having a smaller or larger separation, which affects their interaction, as noted in Chapter 2.2.3.1. Koda et al. reported that Sonazoid™ MBs form aggregates of 9 µm in diameter during insonation with f_c = 3 MHz at maximimum 100 kPa (while Vscan™ has a measured PNP = 0.6 MPa), starting with an aggregate size of 8 µm at time zero [57]. Insonation and videomicroscopy was however maintained for only 3 s, and the MB concentration was not mentioned, however aggregation $<$1 s after onset of insonation is consistent with the observations in this thesis (see Figure 4.4). These aggregates, although not properly measured due to the poor image quality, are considerably larger than 9 µm 0.5-4 s after insonation, most likely due to the different concentration and insonation parameters. The observed aggregation is presumably not physiologically relevant due to the much lower concentrations in addition to blood flow that will be present in vivo.

Sonazoid™ has a reported median diameter of 2.6 µm, with $>$99.9 % below 7 µm [150]. On the other hand, ACT bubbles are an order of magnitude larger than Sonazoid™ as well as most other conventional US contrast agents once activated. Stationary ACT bubbles that do not aggregate are formed during the 2.5 MHz insonation, however with some degree of coalescence. As for the observed Sonazoid™ aggregation, coalescence of ACT bubbles is unlikely to happen in vivo due to lower concentrations, increasing the distance between bubbles. Collapse of ACT bubbles was not observed and is presumed very unlikely.

During insonation of ACT bubbles, not all ACT clusters will be activated into ACT bubbles, and activation yield depends on the solution in which the ACT compound is diluted, being 91 % for Isoton® II (PBS solution) and 45 % for human serum albumin [142], which may explain the observation of the bright spots in Figure 4.5. The bright spots are inconceivably due to image artifacts, PDMS debris or dust particles. If some of the bright spots are individual Sonazoid™ MBs, their unexpected persistence may be due to Sonazoid™ experiencing the acoustic field differently in the presence of ACT clusters/bubbles, from when Sonazoid™ is insonated separately. However, Sontum et al. reported that no unactivated clusters, free emulsion droplets or Sonazoid™ MBs could be observed after insonation [9].

5.2.2 ACT bubble size during 2.5 MHz insonation

The image analysis of ACT bubbles shows that the bubbles are larger than the sizes reported by Sontum et al. [9], Healey et al. [142] and Kotopoulis et al. [61] in vitro as well as ex vivo. Sontum et al. investigated ACT bubble size as a function of time after insonation, and reported a peak number mean diameter of $\sim$25 µm after $\sim$30 s. The authors utilized a sonometry set-up based on custom-made instrumentation and software, employing numerical inversion methods [9, 142]. The increasing diameter after insonation stopped is in consistency with the results reported herein. However, the authors reported that the diameter remained stable until close to 1 min before slowly diminishing, with the volume of ACT bubbles decaying close to exponentially from that time point. The mean diameter in this thesis reached $\sim$30 µm after just 10 s of insonation and continued to grow both during and after the remaining insonation period. It could not be confirmed whether insonation was critical for the bubble growth rate once clusters were already activated, but it likely plays a role due to rectified diffusion. The mean diameter of 42-45 µm between activation stopped and enhancement started gives an indication of the diameter 1 min after insonation in this thesis, i.e. close to twice the value reported by Sontum et al. Nevertheless, insonation conditions were different as activation lasted for only 10 s, and nominal MI was 0.5.

Healey et al. reported a mean diameter of 22 µm after 30 s of insonation using the mentioned sonometry set-up, which gave a "simulated" Gaussian volume-weighted distribution with a full width at half maximum of 10-25 µm. ACT bubble size should reach maximum 12 s after insonation stops, according to their simulations. In addition, ACT bubble size was evaluated using an ex vivo extracorporeal measurement chamber after activation in the cardiac chamber of a dog model, yielding the same volume weighted mean diameter of 22 µm with no ACT bubbles above 44 µm. It was not given for how long the ACT bubbles were present in the acoustic field during activation in vivo, and neither of the authors discussed ACT bubble growth as a function of duration of insonation.

Kotopoulis et al. noted that the conversion from an ACT cluster to an ACT bubble happens

within 5 µs of insonation, resulting in a 6 µm bubble after 36 µs of insonation. After terminating the insonation, the bubble continued to grow, reaching 25 µm after 30 s. The rapid activation of ACT clusters was also observed in this project, with visible bubbles in the microscope <1 s after insonation started, which supports that the insonation period of 45 s is sufficient. Again, the growth after insonation stopped is consistent with the observations reported herein.

Important considerations that may explain the prominent growth of ACT bubbles in this thesis work are related to the conditions under which the experiments were performed. Striving for more physiologically relevant conditions may reduce excess bubble growth to gain more realistic insights about ACT bubble size and lifetime in vivo. Firstly, in contrast to the reported sonometry set-ups by Sontum et al. and Healey et al., control of gas saturation was not attempted in this master project. If the PBS used to dilute the ACT compound contained a higher gas fraction, it is reasonable to assume that more gas would diffuse into ACT bubbles, resulting in excess bubble growth. In the sonometry set-ups, gas saturation of Isoton® II diluter was controlled at 85 %. On the other hand, in a different set-up by Sontum et al., microscopy image analysis of ACT compound diluted in PBS or water for injection with unspecified gas saturation gave more similar results to this thesis. The authors observed ACT bubbles in the 50-100 µm range. To test the role of the PBS used in this thesis, analysis of ACT bubbles activated from an undiluted cluster solution was attempted, but was unfortunately not feasible due to substantial Sonazoid™ aggregation which disturbed the image quality, as well as prominent bubble coalescence which yielded artificially large bubbles. Secondly, the temperature of the materials in this project was not controlled, which may have affected the size as the temperature influences gas solubility and saturation threshold, and hence also gas fraction. In a mirofluidic device, the small liquid volume and high surface to volume ratio will likely have effects on especially the heat exchange of the liquid. This is relevant to consider as experiments herein were conducted at room temperature while the liquids were pre-heated to 37 °C, without a consistent routine for subsequent re-heating between experiments. Sontum et al. and Healey et al. both kept the temperature constant at 37 °C in their sonometry set-ups. In future experiments, it is recommended to control both the temperature and the gas fraction of the solution in which the ACT compound is diluted. Conducting the experiments in an environment with a constant temperature of 37 °C should also be considered.

There are additional factors that may explain the large ACT bubble diameters. The concentration of ACT clusters is of importance as it may affect the concentration of dissolved Sonazoid^{TM} and hence the gas fraction. Moreover, a shorter distance between resulting ACT bubbles promotes Ostwald ripening and coalescence. Naturally, it may be desirable to use clinically relevant concentrations as ACT bubbles are unlikely to interact with each other in vivo, however, too low concentration of ACT clusters may result in an undesirably low number of ACT bubbles. While Sontum et al. and Healey et al. did not specify their dilutions, Spiros et al. diluted their sample 10-fold. Last but not least, the different insonation parameters and conditions in this thesis work compared to the literature may have affected the results, and there are errors related to the image analysis. The video quality is also an important consideration as all ACT bubbles within the field of view were not simultaneously in focus, and images had to be edited manually for adequate quality, with a lack of acceptable standardized processing.

Comparing the ACT bubble size distribution to the results from the pre-master specialization project, a similar behaviour $\sim$1 s after insonation onset can be observed, with about half of the MBs in the 10-20 µm range compared to two thirds in this thesis. The ACT bubbles were, however, more different 1 min after activation had stopped, with 32 % in the 10-20 µm range and a mean diameter of 29.9 µm. For comparison, the ACT bubbles presented herein had a mean diameter of 42-45 µm around this time point, with less than 14 % below 20 µm. The analysis in the pre-master project was based on a single experiment using an undiluted ACT cluster solution. Moreover, a substantial amount of air was present in the channel before activation, and the device studied had a glass bottom. Hence, there could potentially be significant US reflection compared to the present set-up with M-devices, resulting in a different ACT bubble size.

5.2.3 ACT bubble behaviour and displacement of cells during low frequency enhancement

In the channels of empty devices during low frequency enhancement of ACT bubbles, nothing could be observed that was undoubtedly caused by the insonation, but the situation was different for channels containing PC3 cells. The observed changes in ACT bubble size can not be solely explained by rectified diffusion during insonation, as changes were also observed in the absence of US. ACT bubbles of all size groups visible with the 10x objective remained stationary throughout insonation in empty channels, and the lack of bubble movement may be explained by the zero flow conditions. Bubble movement was however observed in channels with PC3 cells during sonoporation studies as soon as the enhancement transducer was switched on (Figure 4.12 and Figure 4.13), likely due to ACT bubbles getting propelled by acoustic radiation forces [43]. This was however not observed during activation, presumably due to the different acoustic fields. The different bubble behaviour depending on presence of cells can be related to whether or not ACT bubbles are in physical contact with the channel surface, which is also possible for bubbles of diameter below the channel height (59-72 µm) as they are expected to float. Presumably, the ACT bubbles might have a higher affinity to an un-coated PDMS surface which immobilizes them, rather than a surface where cells, proteins and other macromolecules are present. Acoustic radiation forces may also be responsible for some of the movement of cells observed in Figure 4.12h and Figure 4.13 [151], but based on the videos, cell displacement was mainly due to cells being pushed or dragged by the translating ACT bubbles. In other words, physical contact between cells and ACT bubbles was very likely. Cell displacement may additionally be due to the streams generated by moving or cavitating ACT bubbles. It was inconclusive whether ACT bubbles are able to detach cells.

In future experiments, it may be interesting to repeat the experiments using a transducer with different MI. The MI = 0.5 in this project is considerably higher than those reported in pre-clinical studies of 0.1 [61] and 0.2 [62].

5.3 Application of PC3-seeded microfluidic channels to study sonoporation

The devices and insonation set-up developed in this project allowed sonoporation studies to be carried out, where new and/or enhanced fluorescence signals could be detected qualitatively for both MBs. Importantly, the video quality and substantial fluorescence background have restricted the opportunities for quantitative analysis. Semi-quantitative evaluation of change of fluorescence intensity indicates increasing PI uptake during enhancement of ACT bubbles. The lack of control experiments is of course a limitation, hence it is strongly recommended that control experiments are carried out in the future with the devices and protocols developed in this project. Moreover, using a single channel multiple times should be avoided. Although the goal of this master project was to create a vascular model, the observation of cancer cells becoming sonoporated by cavitating MBs is yet a contribution to research areas concerning tumour sonoporation for increased drug uptake.

5.3.1 Sonoporation caused by 2.5 MHz insonation of Sonazoid™ and ACT bubbles

Sonoporation of PC3 cells in microfluidic devices could be observed based on the qualitative evaluation of appearance of signals from PI before and after 2.5 MHz insonation of MBs, as the dye is impermeable to intact cell membranes. Enhanced PI uptake following insonation of Sonazoid™ is consistent with the work done by S. Hanstad, who studied co-incubation of this MB and fluorescently labeled nanoparticles in PC3 cells seeded in a CLINIcell®, insonated at similar MI (0.32 and 0.45) [68]. A modest increased uptake of nanoparticles was observed, when compared to an un-treated control, indicating sonoporation or enhanced endocytosis. The concentration of Sonazoid™ bubbles was however much lower; 1.25 million per mL in comparison to 0.3 billion per mL in this project. A more similar Sonazoid™ MB concentration (0.6 billion MBs per mL in 10 mL cell suspension) was used by Nejad et al., who characterized interactions between the MBs and human lymphoma cells (U937 cell line) at MI = 0.13, i.e. well below the threshold of inertial cavitation [152]. The authors found that Sonazoid™

MBs caused mild biomechanical effects on the cells, including local membrane protrusions and reparable submicron poration without causing any cell disruption. Sonoporation by 30 % Sonazoid™ in growth medium at MI = 0.4 (as in this project) was reported by Tomizawa et al., manifested as a suppressed cell proliferation in two different hepatocellular carcinoma cell lines due to the enhanced uptake of short-hairpin RNA of frizzled-2 [48]. The authors noted that sonoporation would be enhanced by collapse of MBs, but actual MI was not verified. Enhanced sonoporation by MB collapse is consistent with the previously mentioned sonoporation study by Juang et al. [22]. MB destruction by insonation during steady state flow in 100 µm × 100 µm channels caused significant PI uptake in HUVECs proximal to the collapsed MBs [22]. It was not specified what kind of MBs were used. The very limited sonoporation reported herein suggests that Sonazoid™ collapse did not happen, or was scarce. Nevertheless, considering the reported Sonazoid™ concentrations in sonoporation experiments, the used MB concentration is regarded as adequate for sonoporation to occur.

Sonoporation of PC3 cells following activation of ACT clusters into ACT bubbles was observed as overlap of new fluorescence spots and ACT bubbles. As the amount of such spots is limited due to the substantial amount of background fluorescence and a limited number of ACT bubbles, it cannot be concluded quantitatively that ACT bubbles will cause more sonoporation than Sonazoid™ during 2.5 MHz insonation. However, a single ACT bubble, being much larger than a Sonazoid™ bubble, has undoubtedly the potential of causing more sonoporation. This conclusion can be drawn from the appearance of two distinct fluorescence spots overlapping with a single ACT bubble in Figure 4.12b and the extremely low number of ACT bubbles present in a channel with respect to Sonazoid™. Importantly, the results indicate that sonoporation is possible *without* inertial cavitation resulting in ACT bubble collapse. As already mentioned, physical contact between ACT bubbles and cells was likely, followed by sonoporation resulting in increased PI uptake. This makes the model highly relevant as ACT bubbles are expected to deposit in microvasculature in vivo, being in physical contact with endothelial cells locally. To explain the enhanced uptake as a consequence of the contact, the ACT bubble may have mechanically deformed the cell membrane as it cavitates, pushing and pulling the cell membrane with resulting pore formation due to the mechanical stresses [52]. Furthermore, sonoporation may have been caused by microstreams that also affect cells not in physical contact with the

bubble. This could be the case for the fluorescence spots appearing in areas that did not overlap with an ACT bubble. On the other hand, sonoporation in these areas as well as further away from ACT bubbles could also be caused by Sonazoid^{TM} MBs that did not form ACT clusters, although their presence could not be verified.

5.3.2 Sonoporation during enhancement of ACT bubbles

The results presented in this thesis indicate additional PI uptake due to 500 kHz insonation of ACT bubbles during enhancement step, however, the uptake can be due to other factors than cavitation of ACT bubbles. Due to the lack of control experiments, additional uptake as a consequence of time can not be ruled out. Moreover, it is emphasized that the change in fluorescence intensity could not be verified accurately. Additional PI uptake is nevertheless expected to be due to cavitating ACT bubbles in proximity to cells, causing already sonoporated cells from the activation step to absorb additional PI. Considering the observed fluorescence signals close to ACT bubbles, the results are in favour of this assumption, although not verified for all spots. Changes in the appearance of spots including their intensity are evident in Figure 4.12c and h. Although quite a few fluorescence signals were out of focus before onset of activation, several fluorescence spots appeared unresolved only after insonation, especially after the enhancement step. Such unresolved spot(s) can be seen in Figure 4.12c, and may be due to a leakage of PI out from the cells seen in Figure 4.12b, as the spot(s) appeared unresolved even when adjusting the microscope focus. On the other hand, one of the annotated fluorescence spots seen in Figure 4.12h is visibly larger than in Figure 4.12g. The size and intensity of this spot suggests that it originates from more cells than in Figure 4.12g, although this could not be confirmed from phase contrast microscopy. Measures to improve video quality and reduce background fluorescence are necessary for quantitative analysis to be performed where cells in the immediate proximity of ACT bubbles can be evaluated. In addition, control experiments and a different MI as mentioned earlier, are recommended for the future.

5.4 Future work

Many insights and opportunities have been uncovered from the experiences in this master project, which will be helpful in improving the experimental set-up to gain quantitative results in the future. Undoubtedly, the established protocol for microfluidic device fabrication (and cell culture) can be used in the future. Melina Mühlenpfordt and Annemieke van Wamel have already applied the present microfluidic devices in their own experiments with MBs, including imaging ACT bubble cavitation at 25 million fps using a ultra high speed recording set-up at the University of Pittsburgh. By using the devices in practise, this thesis work has demonstrated that sonoporation can be detected for two very different MBs. Without doubt, the microfluidic vascular model provides a platform to study many aspects related to the interactions between endothelial cells and cavitating MBs. The amount of additional cues that can be added seems unlimited; additional types of MBs studied at varying concentration, nanoparticles, chemotherapies and additional fluorescence dyes and/or macromolecules may be included. Furthermore, the effects of varying insonation and liquid flow parameters can be studied. Even additional cell types may be added to include heterotypic cell signaling occurring between tumour and/or stromal and endothelial cells in co-culture [83, 87, 90, 91], or how drugs or nanoparticles are transported across the capillary wall to the tumour [113] under the influence of cavitating mirobubbles. The microfluidic devices can be tailored towards more specific applications, e.g. down-scaling channel dimensions to mimic capillaries as already mentioned, but this will require further optimization. This section will summarize the previous discussion regarding recommendations for the future, in addition to providing some additional suggestions and considerations.

The microfluidic devices developed in this project have already proved to allow cell culture with the possibility of maintaining culture for up to several days in the case of HUVEC, and M-devices are regarded as suitable for both culture with endothelial cells as well as insonation experiments. However, the process of seeding cells should be improved to achieve higher reproducibility and confluence, and to reduce the number of unattached and non-viable cells present in the microchannels. A modified channel design could also be considered for this purpose, where for example the inlet and outlet regions may be further optimized to facilitate even

distribution of cells in the channel. This will enable a more robust model to study MB - cell interactions such as sonoporation with significantly decreased fluorescence background, which will allow accurate quantitative assays. Moreover, reproducible endothelialized microchannels will enable repeat and control experiments to be performed. As already pointed out, there are indications that the issues experienced with PC3 will not necessarily apply for HUVEC, and that successful HUVEC culture appears to be more easily achievable. Efforts could be made for the establishment of 3D vessels for a more physiologically relevant model, allowing the study of MB - cell interactions in 3D such as during occlusion by ACT bubbles.

The main obstacle in this project hampering quantitative analysis was the quality of the obtained videos. For improvements, a different experimental set-up is highly recommended, especially with regards to the microscope and camera used for recording. In this project, the microscope light had to pass various layers of materials during imaging, and it was difficult to secure microfluidic devices to the sample stage. The water bath placed on top of the device, being already small in size with respect to the transducers, would barely fit in the microscope set-up. Moreover, the water bath disturbed the image quality due to imperfections in the plastic foil resulting in excess light scattering, hence submerging the whole device in water would perhaps be more ideal (ensuring no entry of water into the device) [117]. For these reasons, a different microscope that is more compatible with insonation set-ups is recommended for the future, with the addition of a different camera that allows significant improvements in quality and frame rate. With a high speed camera, new findings on MB behaviour in the present in vitro system may be uncovered, although ultra high speed imaging is required to visualize cavitation.

Based on the results and discussion of ACT bubble size, there are several experimental aspects that can be improved. Controlling temperature, gas saturation and decreasing the ACT cluster concentration will strengthen the reproducibility and in vivo relevance of the experiments. 85 % gas saturation of PBS may be achieved according to the protocol by Healey et al. for Isoton® II [142]. Moreover, an additional parameter that could be studied is the lifetime of ACT bubbles once activated, which is expected to be 5-10 min in vivo [9].

It may seem that the main attribute of microfluidic technology has not been exploited in this thesis, as the insonation experiments were all conducted under zero flow conditions. Nevertheless, the opportunity of adding flow exists [22], but will require a different experimental set-up including more advanced imaging tools such as a high speed camera. The importance of adding flow in a vascular model was already mentioned in Chapter 2.4.2 in terms of shear stress experienced by endothelial cells which may result in a different response to cavitating MBs [117]. Moreover, the flow MBs experience in vivo will both affect the time during which they are subject to the acoustic field, and possibly also their potential of interacting with each other as well as cells. Especially the mechanisms responsible for the therapeutic potential of ACT should be further studied and elucidated under dynamic flow conditions in vitro.

Chapter 6

Conclusion

Throughout this master project, a protocol has been established to produce microfluidic devices that have proven to fulfill the following: 1) suitability for cell culture, 2) suitability for studying different MBs real-time during insonation and 3) compatibility with sonoporation experiments. From the experiences gained during the pre-master specialization project leading up to this master project, new microfluidic devices were established in order to facilitate endothelial cell seeding and culture before subsequent experiments with MBs and insonation. A design comprising a single microfluidic channel was employed, and the rectangular cross section was increased in both height and width to decrease hydraulic resistance and alleviate cell clustering. However, fabrication of significantly taller channels was difficult with the available photolithography equipment, unleashing a host of optimization challenges that required considerable time to be dealt with. In addition to the new dimensions and channel layout, inlet and outlet areas were also re-designed to facilitate cell loading into the microchannels. Consequently, relatively confluent monolayers of both an endothelial cell line (HUVEC) as well as a cancer cell line (PC3) were observed within microfluidic devices of 400 and 600 µm width, while further optimization is necessary to achieve acceptable endothelial layers in 200 µm or smaller channels. Furthermore, as the microfluidic devices were both optically and acoustically transparent, MB behaviour could be studied, including concentration-dependent behaviour of Sonazoid^{TM} and the size of ACT bubbles. It was concluded that the ACT bubbles observed in this project were significantly larger than reported diameters from literature, most likely due to excess gas present in the solution and a high concentration of ACT clusters,

although insonation conditions were also different.

For practical reasons, PC3 cells were used to simulate endothelial linings during insonation experiments. It is believed that the mechanical interactions between MBs and PC3 are translatable to an endothelial cell line, so that sonoporation of endothelial cells may also be observed with the present devices and experimental set-up. Sonoporation, manifested as uptake of PI during insonation with MBs, was observed qualitatively to some degree for both Sonazoid™ and ACT. The interaction between ACT bubbles and cells was for the first time studied in microchannels, and there are strong indications that sonoporation by ACT happens as soon as during the activation step. Moreover, sonoporation by ACT is likely related to physical contact between cells and a single ACT bubble without inertial cavitation taking place. Sonoporation during the low frequency enhancement step of ACT could not be quantified accurately due to excess background fluorescence from non-viable cells and poor video quality, although the results indicated enhanced fluorescence for PC3 cells proximal to ACT-bubbles. A different experimental set-up including a different microscope and camera is recommended for future experiments using the developed in vitro system.

The goal of this master project was achieved with respect to establishing an in vitro system that can fulfill its purposes at the proof-of-concept stage and already uncover some of the interactions happening between MBs and cells. The experiences from this work will be very helpful in future experimental set-ups with endothelialized microfluidic channels subject to MBs in acoustic fields, to gain insights on how endothelial cells respond to MBs and cavitation in vivo.

References

1. Li, R. G., van Wamel, A., Mühlenpfordt, M. & de Lange Davies, C. Pre-master specialization project. A Microfluidic In Vitro Model for Studying Acoustic Cluster Therapy (2017).

2. Wilhelm, S., Tavares, A. J., Dai, Q., Ohta, S., Audet, J., Dvorak, H. F. & Chan, W. C. W. Analysis of nanoparticle delivery to tumours. *Nature Reviews Materials* **1** (2016).

3. Mullick Chowdhury, S., Lee, T. & Willmann, J. K. Ultrasound-guided drug delivery in cancer. *Ultrasonography* **36,** 171–184 (2017).

4. Nance, E., Timbie, K., Miller, G. W., Song, J., Louttit, C., Klibanov, A. L., Shih, T. Y., Swaminathan, G., Tamargo, R. J., Woodworth, G. F., Hanes, J. & Price, R. J. Non-invasive delivery of stealth, brain-penetrating nanoparticles across the blood-brain barrier using MRI-guided focused ultrasound. *J Control Release* **189,** 123–132 (2014).

5. Bekeredjian, R., Grayburn, P. A. & Shohet, R. V. Use of ultrasound contrast agents for gene or drug delivery in cardiovascular medicine. *J. Am. Coll. Cardiol.* **45,** 329–335 (2005).

6. Kooiman, K., Vos, H. J., Versluis, M. & de Jong, N. Acoustic behavior of microbubbles and implications for drug delivery. *Adv. Drug Deliv. Rev.* **72,** 28–48 (2014).

7. Guo, X., Li, Q., Zhang, Z., Zhang, D. & Tu, J. Investigation on the inertial cavitation threshold and shell properties of commercialized ultrasound contrast agent microbubbles. *J. Acoust. Soc. Am.* **134,** 1622–1631 (2013).

8. Wood, A. K. & Sehgal, C. M. A review of low-intensity ultrasound for cancer therapy. *Ultrasound Med Biol* **41,** 905–928 (2015).

9. Sontum, P., Kvale, S., Healey, A. J., Skurtveit, R., Watanabe, R., Matsumura, M. & Ostensen, J. Acoustic Cluster Therapy (ACT)–A novel concept for ultrasound mediated, targeted drug delivery. *Int J Pharm* **495,** 1019–1027 (2015).

10. Picollet-D'hahan, N., Dolega, M. E., Liguori, L., Marquette, C., Le Gac, S., Gidrol, X. & Martin, D. K. A 3D Toolbox to Enhance Physiological Relevance of Human Tissue Models. *Trends Biotechnol.* **34,** 757–769 (2016).

11. Young, E. W. & Beebe, D. J. Fundamentals of microfluidic cell culture in controlled microenvironments. *Chem Soc Rev* **39,** 1036–1048 (2010).

12. Tehranirokh, M., Kouzani, A. Z., Francis, P. S. & Kanwar, J. R. Microfluidic devices for cell cultivation and proliferation. *Biomicrofluidics* **7,** 1–32 (2013).

13. Bhatia, S. N. & Ingber, D. E. Microfluidic organs-on-chips. *Nat. Biotechnol.* **32,** 760–772 (2014).

14. Young, E. W. Cells, tissues, and organs on chips: challenges and opportunities for the cancer tumor microenvironment. *Integr Biol (Camb)* **5,** 1096–1109 (2013).

15. Lovitt, C. J., Shelper, T. B. & Avery, V. M. Cancer drug discovery: recent innovative approaches to tumor modeling. *Expert Opin Drug Discov* **11,** 885–894 (2016).

16. Kashaninejad, N., Nikmaneshi, M. R., Moghadas, H., Kiyoumarsi Oskouei, A., Rismanian, M., Barisam, M., Saidi, M. S. & Firoozabadi, B. Organ-Tumor-on-a-Chip for Chemosensitivity Assay: A Critical Review. *Micromachines* **7,** 130–154 (2016).

17. Rothbauer, M., Zirath, H. & Ertl, P. Recent advances in microfluidic technologies for cell-to-cell interaction studies. *Lab Chip* (2017).

18. Kim, S., Kim, W., Lim, S. & Jeon, J. S. Vasculature-On-A-Chip for In Vitro Disease Models. *Bioengineering (Basel)* **4** (2017).

19. Wong, K. H., Chan, J. M., Kamm, R. D. & Tien, J. Microfluidic models of vascular functions. *Annu Rev Biomed Eng* **14,** 205–230 (2012).

20. Gray, K. M. & Stroka, K. M. Vascular endothelial cell mechanosensing: New insights gained from biomimetic microfluidic models. *Semin. Cell Dev. Biol.* **71,** 106–117 (2017).

21. Meng, L., Cai, F., Jiang, P., Deng, Z., Li, F., Niu, L., Chen, Y., Wu, J. & Zheng, H. On-chip targeted single cell sonoporation with microbubble destruction excited by surface acoustic waves. *Applied Physics Letters* **104,** 073701 (2014).

22. Juang, E., Cock, I. D., Keravnou, C., Keller, S., Gallagher, M., Zheng, Y. & Averkiou, M. Engineered 3D microvessels for the study of angiogenesis and sonoporation. *Abstract from The 22nd European symposium on Ultrasound Contrast Imaging* (2017).

23. Gac, S. L., Zwaan, E., van den Berg, A. & Ohl, C. D. Sonoporation of suspension cells with a single cavitation bubble in a microfluidic confinement. *Lab Chip* **7,** 1666–1672 (2007).

24. Dreaden, E. C., Austin, L. A., Mackey, M. A. & El-Sayed, M. A. Size matters: gold nanoparticles in targeted cancer drug delivery. *Ther Deliv* **3,** 457–478 (2012).

25. Zhang, W., Zhang, Z. & Zhang, Y. The application of carbon nanotubes in target drug delivery systems for cancer therapies. *Nanoscale Res Lett* **6,** 1–22 (2011).

26. Probst, C. E., Zrazhevskiy, P., Bagalkot, V. & Gao, X. Quantum dots as a platform for nanoparticle drug delivery vehicle design. *Adv. Drug Deliv. Rev.* **65,** 703–718 (2013).

27. Chan, J. M., Valencia, P. M., Zhang, L., Langer, R. & Farokhzad, O. C. Polymeric nanoparticles for drug delivery. *Methods Mol. Biol.* **624,** 163–175 (2010).

28. Sercombe, L., Veerati, T., Moheimani, F., Wu, S. Y., Sood, A. K. & Hua, S. Advances and Challenges of Liposome Assisted Drug Delivery. *Front Pharmacol* **6,** 286–292 (2015).

29. Mahmoudi, M., Sant, S., Wang, B., Laurent, S. & Sen, T. Superparamagnetic iron oxide nanoparticles (SPIONs): development, surface modification and applications in chemotherapy. *Adv. Drug Deliv. Rev.* **63,** 24–46 (2011).

30. Fang, J., Nakamura, H. & Maeda, H. The EPR effect: Unique features of tumor blood vessels for drug delivery, factors involved, and limitations and augmentation of the effect. *Advanced Drug Delivery Reviews* **63.** EPR Effect Based Drug Design and Clinical Outlook for Enhanced Cancer Chemotherapy, 136–151 (2011).

31. Gao, H., Yang, Z., Zhang, S., Cao, S., Shen, S., Pang, Z. & Jiang, X. Ligand modified nanoparticles increases cell uptake, alters endocytosis and elevates glioma distribution and internalization. *Sci Rep* **3,** 2534 (2013).

32. Suk, J. S., Xu, Q., Kim, N., Hanes, J. & Ensign, L. M. PEGylation as a strategy for improving nanoparticle-based drug and gene delivery. *Adv. Drug Deliv. Rev.* **99,** 28–51 (2016).

33. Heldin, C. H., Rubin, K., Pietras, K. & Ostman, A. High interstitial fluid pressure - an obstacle in cancer therapy. *Nat. Rev. Cancer* **4,** 806–813 (2004).

34. Torosean, S., Flynn, B., Axelsson, J., Gunn, J., Samkoe, K. S., Hasan, T., Doyley, M. M. & Pogue, B. W. Nanoparticle uptake in tumors is mediated by the interplay of vascular and collagen density with interstitial pressure. *Nanomedicine* **9,** 151–158 (2013).

35. Blanco, E., Shen, H. & Ferrari, M. Principles of nanoparticle design for overcoming biological barriers to drug delivery. *Nat. Biotechnol.* **33,** 941–951 (2015).

36. Laugier, P. & Haïat, G. *Bone Quantitative Ultrasound* 1st ed., 29–45. ISBN: 978-94-007-0017-8 (Springer Netherlands, 2011).

37. Pitt, W. G., Husseini, G. A. & Staples, B. J. Ultrasonic drug delivery–a general review. *Expert Opin Drug Deliv* **1,** 37–56 (2004).

38. Shung, K. K. *Diagnostic ultrasound; imaging and blood flow measurements* 1st ed., 5–78. ISBN: 0-8247-4096-3 (CRC Press, 2006).

39. Doinikov, A. A. *Recent Research Developments in Acoustics* 1st ed., 39–67. ISBN: 81-7895-083-9 (Transworld Research Network, 2003).

40. Hynynen, K. & Jones, R. M. Image-guided ultrasound phased arrays are a disruptive technology for non-invasive therapy. *Phys Med Biol* **61,** 206–248 (2016).

41. Tsutsui, J. M., Xie, F. & Porter, R. T. The use of microbubbles to target drug delivery. *Cardiovasc Ultrasound* **2,** 23–29 (2004).

42. Paefgen, V., Doleschel, D. & Kiessling, F. Evolution of contrast agents for ultrasound imaging and ultrasound-mediated drug delivery. *Front Pharmacol* **6,** 197 (2015).

43. Fan, Z., Kumon, R. E. & Deng, C. X. Mechanisms of microbubble-facilitated sonoporation for drug and gene delivery. *Ther Deliv* **5,** 467–486 (2014).

44. Wang, J. F., Wang, J. B., Chen, H., Zhang, C. M., Liu, L., Pan, S. H. & Wu, C. J. Ultrasound-mediated microbubble destruction enhances gene transfection in pancreatic cancer cells. *Adv Ther* **25,** 412–421 (2008).

45. Escoffre, J. M., Piron, J., Novell, A. & Bouakaz, A. Doxorubicin delivery into tumor cells with ultrasound and microbubbles. *Mol. Pharm.* **8,** 799–806 (2011).

46. Heath, C. H., Sorace, A., Knowles, J., Rosenthal, E. & Hoyt, K. Microbubble therapy enhances anti-tumor properties of cisplatin and cetuximab in vitro and in vivo. *Otolaryngol Head Neck Surg* **146,** 938–945 (2012).

47. Sorace, A. G., Warram, J. M., Umphrey, H. & Hoyt, K. Microbubble-mediated ultrasonic techniques for improved chemotherapeutic delivery in cancer. *J Drug Target* **20,** 43–54 (2012).

48. Tomizawa, M., Shinozaki, F., Motoyoshi, Y., Sugiyama, T., Yamamoto, S. & Ishige, N. Suppression of hepatocellular carcinoma cell proliferation by short hairpin RNA of frizzled 2 with Sonazoid-enhanced irradiation. *Int. J. Oncol.* **48,** 123–129 (2016).

49. Dimcevski, G., Kotopoulis, S., Bjanes, T., Hoem, D., Schøtt, J., Gjertsen, B. T., Biermann, M., Molven, A., Sorbye, H., McCormack, E., Postema, M. & Gilja, O. H. A human clinical trial using ultrasound and microbubbles to enhance gemcitabine treatment of inoperable pancreatic cancer. *J Control Release* **243,** 172–181 (2016).

50. Qin, S., Caskey, C. F. & Ferrara, K. W. Ultrasound contrast microbubbles in imaging and therapy: physical principles and engineering. *Phys Med Biol* **54,** 27–57 (2009).

51. Huang, P., Zhang, Y., Chen, J., Shentu, W., Sun, Y., Yang, Z., Liang, T., Chen, S. & Pu, Z. Enhanced antitumor efficacy of ultrasonic cavitation with up-sized microbubbles in pancreatic cancer. *Oncotarget* **6,** 20241–20251 (2015).

52. Lentacker, I., De Cock, I., Deckers, R., De Smedt, S. C. & Moonen, C. T. Understanding ultrasound induced sonoporation: definitions and underlying mechanisms. *Adv. Drug Deliv. Rev.* **72,** 49–64 (2014).

53. Leong, T., Ashokkumar, M. & Kentish, S. *Handbook of Ultrasonics and Sonochemistry* 1st ed., 69–98. ISBN: 978-981-287-277-7 (2016).

54. Bader, K. B. & Holland, C. K. Gauging the likelihood of stable cavitation from ultrasound contrast agents. *Phys Med Biol* **58,** 127–144 (2013).

55. Flynn, H. G. & Church, C. C. Transient pulsations of small gas bubbles in water. *The Journal of the Acoustical Society of America* **84,** 985–998 (1988).

56. Postema, M., Marmottant, P., Lancee, C. T., Hilgenfeldt, S. & de Jong, N. Ultrasound-induced microbubble coalescence. *Ultrasound Med Biol* **30,** 1337–1344 (2004).

57. Koda, R., Watarai, N., Nakamoto, R., Ohta, T., Masuda, K., Miyamoto, Y. & Chiba, T. Dependence of aggregate formation of microbubbles upon ultrasound condition and exposure time. *Conf Proc IEEE Eng Med Biol Soc* **2011,** 5589–5592 (2011).

58. Talu, E., Lozano, M. M., Powell, R. L., Dayton, P. A. & Longo, M. L. Long-term stability by lipid coating monodisperse microbubbles formed by a flow-focusing device. *Langmuir* **22,** 9487–9490 (2006).

59. De Cock, I., Lajoinie, G., Versluis, M., De Smedt, S. C. & Lentacker, I. Sonoprinting and the importance of microbubble loading for the ultrasound mediated cellular delivery of nanoparticles. *Biomaterials* **83,** 294–307 (2016).

60. Delalande, A., Kotopoulis, S., Rovers, T., Pichon, C. & Postema, M. Sonoporation at a low mechanical index. *Bubble Science, Engineering & Technology* **3,** 3–12 (2011).

61. Kotopoulis, S., Stigen, E., Popa, M., Safont, M. M., Healey, A., Kvale, S., Sontum, P., Gjertsen, B. T., Gilja, O. H. & McCormack, E. Sonoporation with Acoustic Cluster Therapy (ACT®) induces transient tumour volume reduction in a subcutaneous xenograft model of pancreatic ductal adenocarcinoma. *J Control Release* **245,** 70–80 (2017).

62. Van Wamel, A., Sontum, P. C., Healey, A., Kvale, S., Bush, N., Bamber, J. & de Lange Davies, C. Acoustic Cluster Therapy (ACT) enhances the therapeutic efficacy of paclitaxel and Abraxane® for treatment of human prostate adenocarcinoma in mice. *J Control Release* **236,** 15–21 (2016).

63. Unger, E. C., McCreery, T. P., Sweitzer, R. H., Caldwell, V. E. & Wu, Y. Acoustically active lipospheres containing paclitaxel: a new therapeutic ultrasound contrast agent. *Invest Radiol* **33,** 886–892 (1998).

64. Mørch, Y., Hansen, R., Berg, S., Aslund, A. K., Glomm, W. R., Eggen, S., Schmid, R., Johnsen, H., Kubowicz, S., Snipstad, S., Sulheim, E., Hak, S., Singh, G., McDonagh, B. H., Blom, H., de Lange Davies, C. & Stenstad, P. M. Nanoparticle-stabilized microbubbles for multimodal imaging and drug delivery. *Contrast Media Mol Imaging* **10,** 356–366 (2015).

65. Meijering, B. D., Juffermans, L. J., van Wamel, A., Henning, R. H., Zuhorn, I. S., Emmer, M., Versteilen, A. M., Paulus, W. J., van Gilst, W. H., Kooiman, K., de Jong, N., Musters, R. J., Deelman, L. E. & Kamp, O. Ultrasound and microbubble-targeted delivery of macromolecules is regulated by induction of endocytosis and pore formation. *Circ. Res.* **104,** 679–687 (2009).

66. Bohmer, M. R., Chlon, C. H., Raju, B. I., Chin, C. T., Shevchenko, T. & Klibanov, A. L. Focused ultrasound and microbubbles for enhanced extravasation. *J Control Release* **148,** 18–24 (2010).

67. Wang, Y., Bai, W. K., Shen, E. & Hu, B. Sonoporation by low-frequency and low-power ultrasound enhances chemotherapeutic efficacy in prostate cancer cells in vitro. *Oncol Lett* **6,** 495–498 (2013).

68. Hanstad, S. & de Lange Davies, C. Master thesis. Cellular Uptake of Nanoparticles by Sonoporation (2017).

69. Qin, J., Wang, T. Y. & Willmann, J. K. Sonoporation: Applications for Cancer Therapy. *Adv. Exp. Med. Biol.* **880,** 263–291 (2016).

70. Apfel, R. E. & Holland, C. K. Gauging the likelihood of cavitation from short-pulse, low-duty cycle diagnostic ultrasound. *Ultrasound Med Biol* **17,** 179–185 (1991).

71. De Jong, N. Mechanical Index. *European Journal of Echocardiography* **3,** 73–74 (2002).

72. Iniewski, K. *CMOS Biomicrosystems: Where Electronics Meet Biology* 1st ed., 407–457. ISBN: 978-0-470-64190-3 (John Wiley & Sons, Inc., 2011).

73. Sheeran, P. S. & Dayton, P. A. Improving the performance of phase-change perfluorocarbon droplets for medical ultrasonography: current progress, challenges, and prospects. *Scientifica (Cairo)* **2014,** 579684 (2014).

74. Myhre, O., Bjorgan, M., Grant, D., Hustvedt, S. O., Sontum, P. C. & Dirven, H. Safety assessment in rats and dogs of Acoustic Cluster Therapy, a novel concept for ultrasound mediated, targeted drug delivery. *Pharmacol Res Perspect* **4** (2016).

75. Wei-Cheng, T. & Erin, F. *Microfluidics for Biological Applications* 1st ed., 10 (Springer US, 2009).

76. Hundertmark-Zaušková, A. & Lukáčová-Medvid'ová, M. Numerical study of shear-dependent non-Newtonian fluids in compliant vessels. *Computers Mathematics with Applications* **60,** 572–590 (2010).

77. Bruus, H. in. 1st ed., 1–28 (The Royal Society of Chemistry, 2015). ISBN: 978-1-84973-671-8.

78. Ismagilov, R. F., Rosmarin, T. D., Kenis, J. A., Chiu, D. T., Zhang, W., Stone, H. A. & Whitesides, G. M. Pressure-driven laminar flow in tangential microchannels: an elastomeric microfluidic switch. *Anal. Chem.* **73,** 4682–4687 (2001).

79. Evju, Ø. & Mardal, K.-A. *Modeling the Heart and the Circulatory System* 1st ed., 177–195. ISBN: 978-3-319-05230-4 (Springer International Publishing, 2015).

80. Le Gac, S. & van den Berg, A. Single cells as experimentation units in lab-on-a-chip devices. *Trends in biotechnology* **28,** 55–62 (2010).

81. Van der Meer, A. D., Poot, A. A., Duits, M. H., Feijen, J. & Vermes, I. Microfluidic technology in vascular research. *J. Biomed. Biotechnol.* **2009,** 823148 (2009).

82. Esch, E. W., Bahinski, A. & Huh, D. Organs-on-chips at the frontiers of drug discovery. *Nat Rev Drug Discov* **14,** 248–260 (2015).

83. Chung, S., Sudo, R., Mack, P. J., Wan, C. R., Vickerman, V. & Kamm, R. D. Cell migration into scaffolds under co-culture conditions in a microfluidic platform. *Lab Chip* **9,** 269–275 (2009).

84. Zhang, Q., Liu, T. & Qin, J. A microfluidic-based device for study of transendothelial invasion of tumor aggregates in realtime. *Lab Chip* **12,** 2837–2842 (2012).

85. Zervantonakis, I. K., Hughes-Alford, S. K., Charest, J. L., Condeelis, J. S., Gertler, F. B. & Kamm, R. D. Three-dimensional microfluidic model for tumor cell intravasation and endothelial barrier function. *Proc. Natl. Acad. Sci. U.S.A.* **109,** 13515–13520 (2012).

86. Sudo, R., Chung, S., Zervantonakis, I. K., Vickerman, V., Toshimitsu, Y., Griffith, L. G. & Kamm, R. D. Transport-mediated angiogenesis in 3D epithelial coculture. *FASEB J.* **23,** 2155–2164 (2009).

87. Zheng, Y., Chen, J., Craven, M., Choi, N. W., Totorica, S., Diaz-Santana, A., Kermani, P., Hempstead, B., Fischbach-Teschl, C., Lopez, J. A. & Stroock, A. D. In vitro microvessels for the study of angiogenesis and thrombosis. *Proc. Natl. Acad. Sci. U.S.A.* **109,** 9342–9347 (2012).

88. Liu, P. F., Cao, Y. W., Zhang, S. D., Zhao, Y., Liu, X. G., Shi, H. Q., Hu, K. Y., Zhu, G. Q., Ma, B. & Niu, H. T. A bladder cancer microenvironment simulation system based on a microfluidic co-culture model. *Oncotarget* **6,** 37695–37705 (2015).

89. Mi, S., Du, Z., Xu, Y., Wu, Z., Qian, X., Zhang, M. & Sun, W. Microfluidic co-culture system for cancer migratory analysis and anti-metastatic drugs screening. *Sci Rep* **6,** 35544 (2016).

90. Kim, S., Lee, H., Chung, M. & Jeon, N. L. Engineering of functional, perfusable 3D microvascular networks on a chip. *Lab Chip* **13,** 1489–1500 (2013).

91. Lee, H., Park, W., Ryu, H. & Jeon, N. L. A microfluidic platform for quantitative analysis of cancer angiogenesis and intravasation. *Biomicrofluidics* **8,** 054102 (2014).

92. Patra, B., Peng, C. C., Liao, W. H., Lee, C. H. & Tung, Y. C. Drug testing and flow cytometry analysis on a large number of uniform sized tumor spheroids using a microfluidic device. *Sci Rep* **6,** 21061 (2016).

93. Kamei, K., Guo, S., Yu, Z. T., Takahashi, H., Gschweng, E., Suh, C., Wang, X., Tang, J., McLaughlin, J., Witte, O. N., Lee, K. B. & Tseng, H. R. An integrated microfluidic culture device for quantitative analysis of human embryonic stem cells. *Lab Chip* **9,** 555–563 (2009).

94. Shemesh, J., Jalilian, I., Shi, A., Heng Yeoh, G., Knothe Tate, M. L. & Ebrahimi Warkiani, M. Flow-induced stress on adherent cells in microfluidic devices. *Lab Chip* **15,** 4114–4127 (2015).

95. Bartling, B., Tostlebe, H., Darmer, D., Holtz, J., Silber, R. E. & Morawietz, H. Shear stress-dependent expression of apoptosis-regulating genes in endothelial cells. *Biochem. Biophys. Res. Commun.* **278,** 740–746 (2000).

96. Koutsiaris, A. G., Tachmitzi, S. V., Batis, N., Kotoula, M. G., Karabatsas, C. H., Tsironi, E. & Chatzoulis, D. Z. Volume flow and wall shear stress quantification in the human conjunctival capillaries and post-capillary venules in vivo. *Biorheology* **44,** 375–386 (2007).

97. Myers, D. R., Sakurai, Y., Tran, R., Ahn, B., Hardy, E. T., Mannino, R., Kita, A., Tsai, M. & Lam, W. A. Endothelialized microfluidics for studying microvascular interactions in hematologic diseases. *J Vis Exp,* 1170–1179 (2012).

98. Esch, M. B., Post, D. J., Shuler, M. L. & Stokol, T. Characterization of in vitro endothelial linings grown within microfluidic channels. *Tissue Eng Part A* **17,** 2965–2971 (2011).

99. Tsai, M., Kita, A., Leach, J., Rounsevell, R., Huang, J. N., Moake, J., Ware, R. E., Fletcher, D. A. & Lam, W. A. In vitro modeling of the microvascular occlusion and thrombosis that occur in hematologic diseases using microfluidic technology. *J. Clin. Invest.* **122,** 408–418 (2012).

100. Rosano, J. M., Tousi, N., Scott, R. C., Krynska, B., Rizzo, V., Prabhakarpandian, B., Pant, K., Sundaram, S. & Kiani, M. F. A physiologically realistic in vitro model of microvascular networks. *Biomed Microdevices* **11,** 1051–1057 (2009).

101. Hattori, K., Munehira, Y., Kobayashi, H., Satoh, T., Sugiura, S. & Kanamori, T. Microfluidic perfusion culture chip providing different strengths of shear stress for analysis of vascular endothelial function. *J. Biosci. Bioeng.* **118,** 327–332 (2014).

102. Huang, S. B., Wu, M. H., Wang, S. S. & Lee, G. B. Microfluidic cell culture chip with multiplexed medium delivery and efficient cell/scaffold loading mechanisms for high-throughput perfusion 3-dimensional cell culture-based assays. *Biomed Microdevices* **13,** 415–430 (2011).

103. Kim, S.-J., Zhu, X. & Takayama, S. in *Microtechnology for Cell Manipulation and Sorting* (eds Lee, W., Tseng, P. & Di Carlo, D.) 175–192 (Springer International Publishing, 2017).

104. Bogorad, M. I., DeStefano, J., Karlsson, J., Wong, A. D., Gerecht, S. & Searson, P. C. Review: in vitro microvessel models. *Lab Chip* **15,** 4242–4255 (2015).

105. Khan, O. F. & Sefton, M. V. Endothelial cell behaviour within a microfluidic mimic of the flow channels of a modular tissue engineered construct. *Biomed Microdevices* **13,** 69–87 (2011).

106. Van der Meer, A. D., Poot, A. A., Feijen, J. & Vermes, I. Analyzing shear stress-induced alignment of actin filaments in endothelial cells with a microfluidic assay. *Biomicrofluidics* **4,** 011103 (2010).

107. Kusunose, J., Zhang, H., Gagnon, M. K., Pan, T., Simon, S. I. & Ferrara, K. W. Microfluidic system for facilitated quantification of nanoparticle accumulation to cells under laminar flow. *Ann Biomed Eng* **41,** 89–99 (2013).

108. Shamloo, A., Ma, N., Poo, M. M., Sohn, L. L. & Heilshorn, S. C. Endothelial cell polarization and chemotaxis in a microfluidic device. *Lab Chip* **8,** 1292–1299 (2008).

109. Meng, L., Deng, Z., Niu, L., Li, F., Yan, F., Wu, J., Cai, F. & Zheng, H. A Disposable Microfluidic Device for Controlled Drug Release from Thermal-Sensitive Liposomes by High Intensity Focused Ultrasound. *Theranostics* **5,** 1203–1213 (2015).

110. Friend, J. & Yeo, L. Fabrication of microfluidic devices using polydimethylsiloxane. *Biomicrofluidics* **4** (2010).

111. Urbaczek, A. C., Leao, P. A. G. C., Souza, F. Z. R., Afonso, A., Vieira Alberice, J., Cappelini, L. T. D., Carlos, I. Z. & Carrilho, E. Endothelial Cell Culture Under Perfusion On A Polyester-Toner Microfluidic Device. *Sci Rep* **7,** 10466 (2017).

112. *Creative Commons CC BY 4.0 license* Available at `https://creativecommons.org/licenses/by/4.0/`, 10-06-2018. ().

113. Kwak, B., Ozcelikkale, A., Shin, C. S., Park, K. & Han, B. Simulation of complex transport of nanoparticles around a tumor using tumor-microenvironment-on-chip. *J Control Release* **194,** 157–167 (2014).

114. Wang, Y., Meng, R., Zhou, W., Wang, K., Niu, L., Meng, L. & Zheng, H. *Controlled permeation of cell membrane by a single-bubble stable cavitation in a microfluidic device* in *2017 IEEE International Ultrasonics Symposium (IUS)* (2017), 1–1.

115. Lajoinie, G., De Cock, I., Coussios, C. C., Lentacker, I., Le Gac, S., Stride, E. & Versluis, M. In vitro methods to study bubble-cell interactions: Fundamentals and therapeutic applications. *Biomicrofluidics* **10,** 011501 (2016).

116. Quinto-Su, P. A., Lai, H. H., Yoon, H. H., Sims, C. E., Allbritton, N. L. & Venugopalan, V. Examination of laser microbeam cell lysis in a PDMS microfluidic channel using time-resolved imaging. *Lab Chip* **8,** 408–414 (2008).

117. Park, J., Fan, Z. & Deng, C. X. Effects of shear stress cultivation on cell membrane disruption and intracellular calcium concentration in sonoporation of endothelial cells. *J Biomech* **44,** 164–169 (2011).

118. Regehr, K. J., Domenech, M., Koepsel, J. T., Carver, K. C., Ellison-Zelski, S. J., Murphy, W. L., Schuler, L. A., Alarid, E. T. & Beebe, D. J. Biological implications of polydimethylsiloxane-based microfluidic cell culture. *Lab Chip* **9,** 2132–2139 (2009).

119. Toworfe, G. K., Composto, R. J., Adams, C. S., Shapiro, I. M. & Ducheyne, P. Fibronectin adsorption on surface-activated poly(dimethylsiloxane) and its effect on cellular function. *J Biomed Mater Res A* **71,** 449–461 (2004).

120. Berthier, E., Young, E. W. & Beebe, D. Engineers are from PDMS-land, Biologists are from Polystyrenia. *Lab Chip* **12,** 1224–1237 (2012).

121. Mohajerani, E., Farajollahi, F., Mahzoon, R. & Baghery, S. Morphological and thickness analysis for PMMA spin coated films. *J. Optoelectron. Adv. M.* **9 (12),** 3901–3906.

122. Quirk, M. & Serda, J. *Semiconductor Manufacturing Technology* 1st ed. ISBN: 9789861541174 (Pearson Education Taiwan, 2001).

123. Aissaoui, N., Bergaoui, L., Landoulsi, J., Lambert, J. F. & Boujday, S. Silane layers on silicon surfaces: mechanism of interaction, stability, and influence on protein adsorption. *Langmuir* **28,** 656–665 (2012).

124. McDonald, J. C. & Whitesides, G. M. Poly(dimethylsiloxane) as a material for fabricating microfluidic device. *Acc. Chem. Res.* **35,** 491–499 (2002).

125. Wang, Z., Volinsky, A. A. & Gallant, N. D. Crosslinking effect on polydimethylsiloxane elastic modulus measured by custom-built compression instrument. *Journal of Applied Polymer Science* **131,** 41050 (2014).

126. Bodas, D. & Khan-Malek, C. Hydrophilization and hydrophobic recovery of PDMS by oxygen plasma and chemical treatment—An SEM investigation. *Sensors and Actuators B: Chemical* **123,** 368–373 (2007).

127. Cornelissen, C. G., Dietrich, M., Gromann, K., Frese, J., Krueger, S., Sachweh, J. S. & Jockenhoevel, S. Fibronectin coating of oxygenator membranes enhances endothelial cell attachment. *Biomed Eng Online* **12,** 7 (2013).

128. Feinberg, A. W., Schumacher, J. F. & Brennan, A. B. Engineering high-density endothelial cell monolayers on soft substrates. *Acta Biomater* **5,** 2013–2024 (2009).

129. Harris, J., Lee, H., Vahidi, B., Tu, C., Cribbs, D., Jeon, N. L. & Cotman, C. Fabrication of a microfluidic device for the compartmentalization of neuron soma and axons. *J Vis Exp,* 261 (2007).

130. Chuah, Y. J., Koh, Y. T., Lim, K., Menon, N. V., Wu, Y. & Kang, Y. Simple surface engineering of polydimethylsiloxane with polydopamine for stabilized mesenchymal stem cell adhesion and multipotency. *Sci Rep* **5,** 18162 (2015).

131. Koenig, A. L., Gambillara, V. & Grainger, D. W. Correlating fibronectin adsorption with endothelial cell adhesion and signaling on polymer substrates. *J Biomed Mater Res A* **64,** 20–37 (2003).

132. Short, S. M., Talbott, G. A. & Juliano, R. L. Integrin-mediated signaling events in human endothelial cells. *Mol. Biol. Cell* **9,** 1969–1980 (1998).

133. Young, E. W., Wheeler, A. R. & Simmons, C. A. Matrix-dependent adhesion of vascular and valvular endothelial cells in microfluidic channels. *Lab Chip* **7,** 1759–1766 (2007).

134. Neri, S., Mariani, E., Meneghetti, A., Cattini, L. & Facchini, A. Calcein-acetyoxymethyl cytotoxicity assay: standardization of a method allowing additional analyses on recovered effector cells and supernatants. *Clin. Diagn. Lab. Immunol.* **8,** 1131–1135 (2001).

135. Chen, T. *A Practical Guide to Assay Development and High-Throughput Screening in Drug Discovery* 1st ed., 107. ISBN: 9781420070514 (CRC Press, 2009).

136. Kooiman, K., Foppen-Harteveld, M., van der Steen, A. F. & de Jong, N. Sonoporation of endothelial cells by vibrating targeted microbubbles. *J Control Release* **154,** 35–41 (2011).

137. Wang, M., Zhang, Y., Cai, C., Tu, J., Guo, X. & Zhang, D. Sonoporation-induced cell membrane permeabilization and cytoskeleton disassembly at varied acoustic and microbubble-cell parameters. *Sci Rep* **8,** 3885 (2018).

138. Riccardi, C. & Nicoletti, I. Analysis of apoptosis by propidium iodide staining and flow cytometry. *Nat Protoc* **1,** 1458–1461 (2006).

139. *Cardiovascular Physiology* 10th ed. (eds Pappano, A. J. & Wier, W. G.) 153–170. ISBN: 978-0-323-08697-4 (Philadelphia, 2013).

140. Miller, D. L. & Quddus, J. Sonoporation of monolayer cells by diagnostic ultrasound activation of contrast-agent gas bodies. *Ultrasound Med Biol* **26,** 661–667 (2000).

141. Fornaro, M., Plescia, J., Chheang, S., Tallini, G., Zhu, Y. M., King, M., Altieri, D. C. & Languino, L. R. Fibronectin protects prostate cancer cells from tumor necrosis factor-alpha-induced apoptosis via the AKT/survivin pathway. *J. Biol. Chem.* **278,** 50402–50411 (2003).

142. Healey, A. J., Sontum, P. C., Kvale, S., Eriksen, M., Bendiksen, R., Tornes, A. & Ostensen, J. Acoustic Cluster Therapy: In Vitro and Ex Vivo Measurement of Activated Bubble Size Distribution and Temporal Dynamics. *Ultrasound Med Biol* **42,** 1145–1166 (2016).

143. Wamel, A. V., Healey, A., Sontum, P. C., Kvale, S., Bush, N., Bamber, J. & de Lange Davies, C. Acoustic Cluster Therapy (ACT) - pre-clinical proof of principle for local drug delivery and enhanced uptake. *J Control Release* **224,** 158–164 (2016).

144. Schindelin, J., Rueden, C. T., Hiner, M. C. & Eliceiri, K. W. The ImageJ ecosystem: An open platform for biomedical image analysis. *Molecular Reproduction and Development* **82,** 518–529 (2015).

145. Geerts, W. J., Vocking, K., Schoonen, N., Haarbosch, L., van Donselaar, E. G., Regan-Klapisz, E. & Post, J. A. Cobblestone HUVECs: a human model system for studying primary ciliogenesis. *J. Struct. Biol.* **176,** 350–359 (2011).

146. Docheva, D., Padula, D., Schieker, M. & Clausen-Schaumann, H. Effect of collagen I and fibronectin on the adhesion, elasticity and cytoskeletal organization of prostate cancer cells. *Biochem. Biophys. Res. Commun.* **402,** 361–366 (2010).

147. Choi, J. S., Piao, Y. & Seo, T. S. Fabrication of a circular PDMS microchannel for constructing a three-dimensional endothelial cell layer. *Bioprocess Biosyst Eng* **36,** 1871–1878 (2013).

148. Tsuge, H. *Micro- and nanobubbles - fundamentals and applications* 1st ed., 1–355. ISBN: 9789814463102 (CRC press, 2014).

149. Shi, W. T., Forsberg, F., Tornes, A., Ostensen, J. & Goldberg, B. B. Destruction of contrast microbubbles and the association with inertial cavitation. *Ultrasound Med Biol* **26,** 1009–1019 (2000).

150. Sontum, P. C. Physicochemical characteristics of Sonazoid, a new contrast agent for ultrasound imaging. *Ultrasound Med Biol* **34,** 824–833 (2008).

151. Kim, D.-H., Haake, A., Sun, Y., Neild, A. P., Ihm, J. E., Dual, J., Hubbell, J. A., Ju, B.-K. & Nelson, B. J. *High-throughput cell manipulation using ultrasound fields* in *The 26th Annual International Conference of the IEEE Engineering in Medicine and Biology Society* **1** (2004), 2571–2574.

152. Nejad, S. M., Hosseini, H., Akiyama, H. & Tachibana, K. Reparable Cell Sonoporation in Suspension: Theranostic Potential of Microbubble. *Theranostics* **6,** 446–455 (2016).